Analysis of Plasma Wave Irregularities Generated during Active Experiments in Near-Earth Space Environment

Maitrayee Ranade Bordikar

Dissertation submitted to the Faculty of the
Virginia Polytechnic Institute and State University
in partial fulfillment of the requirements for the degree of

Doctor of Philosophy
in
Electrical Engineering

Wayne A. Scales, Chair
C. Robert Clauer
William A. Davis
Danesh K. Tafti
Timothy Pratt

March 27, 2013
Blacksburg, Virginia

Keywords: Dusty Plasma, Particle-in-Cell Code, Hybrid Code, Numerical Simulation, SEE, Ion-Ion Hybrid Structuring, Three-wave Parametric Decay Process

Analysis of Plasma Wave Irregularities Generated during Active Experiments in Near-Earth Space Environment

Maitrayee Ranade Bordikar

(ABSTRACT)

This work focuses on the analysis of plasma irregularities generated during two active space experiments: the injection of an artificial dust layer, and high-power radio waves. The objective of the first experiment is to examine the effects of artificially created dust layers on the scatter of radars from plasma irregularities embedded in dusty plasma in space. This is an alternate approach for understanding the mechanisms of enhanced radar scatter from plasma irregularities embedded in Noctilucent Clouds and Polar Mesospheric Summer Echoes. The second experiment involves a transmission of high power electromagnetic waves into the ionospheric plasma from the ground, which can excite stimulated electromagnetic emissions offset from the transmitter frequency. These stimulated electromagnetic emissions provide diagnostic information of the ionosphere and thus can be used to investigate fundamental physical principles which govern the earth's ionosphere, so that present and future transmission technologies may take into account the complexities of the ionosphere. The interaction altitude of the artificial dust layer and high power radio waves is approximately 250 km and 160 km respectively, thus dealing with uniquely different regions of the ionosphere. Each experiment is discussed separately using theoretical, observational and advanced computational methodologies.

The study first investigates plasma turbulence associated with the creation of an artificial dust layer in the earth's ionosphere. Two scenarios are considered for plasma irregularity generation as dust is injected at an oblique angle across the geomagnetic field. The first is a shear-driven plasma instability due to inhomogeneities in the boundary layer between the injected charged dust layer and the background plasma. This begins to appear at very early times once the dust is released into the space plasma, which is of the order or less than the dust charging time period. The second mechanism is free streaming of the charged dust relative to the background plasma. This produces irregularities at times much longer than the dust charging period and also longer than the dust plasma period. Although both mechanisms are shown to produce turbulence in the lower hybrid frequency range, the resulting irregularities have important differences in their physical characteristics. A comparison between the processes is made to determine the consequences for upcoming observations. Both processes are shown to have the possibility of generating turbulence after the release of dust for the regimes of upcoming space experiments over a range of timescales.

This work also presents the first observations of unique narrowband emissions ordered near the Hydrogen ion (H^+) gyro-frequency (f_{cH}) in the Stimulated Electromagnetic Emission (SEE) spectrum when the transmitter is tuned near the second electron gyro-harmonic frequency ($2f_{ce}$), during ionospheric modification experiments. The frequency structuring of

these newly discovered emission lines is quite unexpected since H^+ is known to be a minor constituent in the interaction region which is near 160 km altitude. The spectral lines are typically shifted from the pump wave frequency by harmonics of a frequency about 10% less than f_{cH} ($\approx$ 800 Hz) and have a bandwidth of less than 50 Hz which is near the O^+ gyro-frequency f_{cO}. A theory is proposed to explain these emissions in terms of a Parametric Decay Instability (PDI) in a multi-ion species plasma due to possible proton precipitation associated with the disturbed conditions during the heating experiment. The observations can be explained by including several percent H^+ ions into the background plasma. The implications are new possibilities for characterizing proton precipitation events during ionospheric heating experiments.

To my lighthouse, Meera.

Acknowledgments

I wish to thank the following people for helping me on my path of pursuing PhD.

Amey, my patient, unwavering, devoted and loving husband, for sharing my goal of undertaking this difficult task while staying apart, for believing in me when I doubted myself, and for the countless days of daddy daycare to our beautiful son during the final months. Arjun Mayon, for motivating me with love and compassion even as he bore the brunt of my moods and absences.

My advisor, Prof. Wayne Scales for his valuable advice and comprehensive guidance during my course of study at Virginia Tech. Thank you for the adventurous journey, Prof Scales. Prof. Robert Clauer, Prof. William Davis, Prof. Timothy Pratt, Prof. Danesh Tafti for serving on my advisory committee.

Dr. Paul Bernhardt for his kind support and help, Dr. Marlene Rosenberg for providing valuable comments on my research work and Edward Kennedy, Mike McCarrick, Stan Briczinski for helping me setup my experiments at HAARP. Many thanks to my colleagues at the Center of Space Science and Engineering Research at Virginia Tech.

Good friends are precious and rare, I consider myself extremely lucky to have found a few of them during my stay here at Virginia Tech. Their company made my life in Blacksburg enjoyable.

Finally my family, my mother, Meera who started my education process and gave me strength, direction and motivation over each hurdle. No words can express my gratitude to my father, Mahadeo, sister, Meghana, brother-in-law, Gyan, and nephew, Vedas, for the kind of support they have given me throughout my life. The encouragement and inspiration that my father-in-law, Umesh, and mother-in-law, Vrushali, have given is priceless.

Contents

List of Figures

List of Tables

Chapter 1

Introduction

As we grow more dependent on an ever-growing network of satellite communication technologies, we find that our way of life is becoming more and more vulnerable to space weather. The study of the environment in near-earth space has become exceedingly important as we continue to venture more frequently into it growing technology and as world becomes more and more dependent on the high-performance electrical devices. The near-earth space environment produces effects that impact our society greatly, including the degradation of our satellite communication systems, navigation systems (e.g. GPS), electric-power systems on earth, satellite integrity, spacecraft and astronauts, and radiation effects on airline passengers, just to name a few. The ultimate goal of such a study is to explore possible strategies for accurate space weather prediction and to provide solutions toward managing this environment. Space weather is characterized by phenomena that occur due to the interaction between the sun's atmosphere and the earth's upper atmosphere (magnetosphere/ionosphere). Examples of such phenomena include: the natural dust layer, proton precipitation, wave-wave interaction, and wave-particle interaction. These occurrences produce degrading effects on our communication systems; therefore, a predictive capability of these disturbances is essential for the study of space weather. Laboratory experiments have been helpful in expanding the knowledge of plasma physics but they are prone to restrictions due to physical boundary conditions. The ionosphere provides a natural plasma environment with different species, such as electrons, ions, and neutrals with their parameters of density, temperature, and collision frequency varying with altitude. Rather than depending on highly variable and sporadic natural events, active space experiments can be used to study and/or simulate natural phenomena occurring in the space environment using controlled stimulus. The primary distinction of passive versus active experimentation is in measuring of the space environment and performing controlled experiments in that environment respectively. Active space experiments allow us to study the basic physics of the space environment, to take control of some physical processes in the space environment, and to study natural phenomena in the space environment. In this work, plasma instabilities generated during two different active experiments conducted in near-earth space environment are investigated: 1. Lower

hybrid irregularities generated during injection of artificial dust layer in the ionosphere, and 2. ion-ion hybrid instabilities generated during radio wave stimulation of the ionosphere.

Lower hybrid irregularities generated during injection of artificial dust layer in the ionosphere: One of the natural phenomenon that occurs in the ionosphere is the dust layer formed by tons of meteoric dust. This layer spans along an altitude range between 80 and 100 kilometers of the earth's upper mesosphere and lower thermosphere. Due to cold temperatures in this region, ice nucleates on this dust layer forming noctilucent clouds (NLC). These are the highest clouds in the earth's atmosphere and are also a spectacular visual display. These dust layers are charged due to a collection of electrons and ions from the earth's ionosphere. This results in irregularities in the electron density above the NLC altitude. Radar signals scatter off of these irregularities, generating the so-called Polar Mesospheric Summer Echoes [Cho and Kelly, 1993; Cho and Rottger, 1997]. An alternate approach to understanding these natural dust layers and the associated turbulence is to perform active space experiments in which a dust cloud is artificially created, in a controlled manner, in the upper atmosphere. The Charged Aerosol Release Experiment (CARE) injected artificial dust at about 250 km altitude into the earth's ionosphere to investigate similarities in plasma irregularities associated with natural and artificial dust layers [Bernhardt, 2011]. CARE utilized radar backscatter to investigate artificial dust clouds. A comparison between the artificial and natural dust layers aids in understanding the physical processes in the natural dust layer, which is currently a forefront issue in space science.

There have been several studies conducted on the various plasma irregularities generated in these injected artificial dust clouds. Bernhardt et al., 1995 considered possible mechanisms of enhanced radar backscatter from space shuttle exhaust as observed with the Arecibo 430 MHz radar. Bharuthram and Rosenberg, 1998 and Rosenberg et al., 1999 considered that the excitation of lower hybrid (LH) type waves were formed by a charged dust beam streaming across the magnetic field. A detailed study of such LH instabilities generated in the streaming dust from rocket exhaust plumes was presented in Rosenberg and Sorasio, 2006. Scales et al., 1995 studied different types of instabilities generated in expanding dust clouds due to velocity-shear flows in the dust cloud boundary. The investigation of early time evolution after expansion of an artificial dust cloud across the magnetic field in the ionosphere was conducted by Scales et al., 2010. In this work, plasma turbulence that was developed at two different time scales was analyzed: 1. The earlier turbulence was due to neutral dust injection at oblique angles to the magnetic field and its charging in background plasma; and 2. The turbulence experienced at a later time was due to the streaming of charged dust relative to the background plasma.

Ion-ion hybrid instabilities generated during radio wave stimulation of the ionosphere: Studying the interaction of nonlinear waves in the ionosphere has been a topic of interest during the past few decades. The excitation of plasma waves in the ionosphere causes turbulence and hence disturbance in communication systems in near-earth space environment. An alternative to studying this interaction is to use ground-based radio beams to perturb the ionosphere and analyze the plasma wave interaction. Ionospheric research

facilities have been in continuous use since the 1950's to investigate fundamental physical principles which govern the earth's ionosphere, so that present and future transmission technologies may take into account the complexities of the ionosphere. A number of such ionospheric research facilities have been built in Europe, Russia and the United States to conduct experimental radio science research, including plasma-wave interactions. These facilities include HIPAS and HAARP in Alaska, EISCAT in Tromso, Norway, SURA in Nizhniy Novgorod, Russia, Arecibo observatory in Puerto Rico, and Jicamarca radio observatory, Peru. Research conducted at these facilities include: polar electrojet and ELF/VLF generation, energetic electrons and artificial airglow emissions, large scale density and temperature modifications, and generation of electrostatic waves, parametric instabilities and production of small-scale density irregularities.

Stimulated Electromagnetic Emission (SEE) has been observed during ionospheric modification experiments when a powerful high-frequency pump wave is transmitted from a heating facility. This results in a complicated series of interactions between the HF radiowave pump (the heater wave) and the internal plasma waves, in the ionized upper atmosphere. The SEE exhibits frequency sidebands upshifted and downshifted from the pump wave frequency within roughly 100 kHz bandwidth. Interest in SEE has been steadily growing since it was first experimentally observed [Thide et al., 1982] because it may be used as a diagnostic tool for the ionosphere, and it is also a fundamental nonlinear plasma phenomenon [Stenlo, 1990] that is not well understood. A classification of SEE spectral features and the description of their possible generation through parametric decay instability processes were provided by Stubbe et al., 1984. Some of the important and classical SEE features are frequency-downshifted sidebands such as: downshifted maximum (DM), broad downshifted maximum (BDM), and downshifted peak (DP): and frequency-upshifted sidebands such as: broad upshifted maximum (BUM) and upshifted maximum (UM). There are other less prominent components, and new ones are likely to be discovered with continued experimentation.

Recently there has been considerable interest in SEE with structures near the ion-gyro frequency observed in the spectrum. O^+ gyro-harmonic structuring observed for second electron gyro-harmonic heating was first reported by Bernhardt et al., 2011. Subsequent observations were made at second and third electron gyro-harmonic heating by Samimi et al., 2012, 2013; Mahmoudian et al., 2013. These works provided a detailed theory to explain the generation of these ion-gyro structures in the SEE spectra in terms of parametric instabilities in a single-component plasma. In this current study, new observations of emission lines at a frequency related to the H^+ gyro-harmonic frequency are reported for the first time and all the observations are analyzed in detail to determine the cause of emission and to explain the generation mechanism.

The organization of this dissertation is as follows:

Chapter 2 provides a background for the research. An introduction to the ionosphere and its different layers is provided, while basic plasma and dusty plasma concepts are explained. Active experiments are defined and their applications and some examples are discussed. The

two active experiments which are investigated in this dissertation are also introduced.

Chapter 3 covers the first experiment: Exploring plasma turbulence in the lower hybrid frequency range associated with the creation of an artificial dust layer in the earth's ionosphere. Two scenarios are considered for plasma irregularity generation, as dust is injected at oblique angles across the magnetic field. Following the introduction to the model, a linear theory of the plasma turbulence is presented, as well as the simulation model used in the research. Finally, the chapter ends with a discussion of the results of the plasma turbulence as generated by the two mechanisms presented. A comparison between the processes is made and conclusions are drawn.

Chapter 4 covers the second experiment: To engage in new observations of structuring near minority ion H^+ gyro-frequency in the SEE spectrum during second electron gyro-harmonic heating. The experimental setup is described, followed by a detailed outline of all the observations. Active conditions during the experiment period are described and a possible cause of the appearance of these emission lines is postulated. A three-wave parametric decay instability of a pump wave into high-frequency upper hybrid/electron Bernstein mode and a low-frequency mode related to H^+ gyro frequency in multi-ion species plasma is developed and proposed as a theory behind these new observations. The comparison of theoretical calculations and observations are made for agreement and conclusions are drawn. These new observations provide possibilities for further diagnostics for determining the density of minority plasma species in ionospheric plasma that have not been considered before with such SEE measurements.

Chapter 5 provides a summary of current work and its conclusions, a list of related publications by the author, and possibilities for future expansion of research.

Chapter 2

Background

This chapter provides fundamental background information on the earth's upper atmosphere, as well as some pertinent information concerning the basic plasma theory and the research's active experiments. The objective is to define and develop the important concepts that will appear in the discussion of the dusty plasmas, stimulated electromagnetic emissions (SEE) and ion-gyro structures in the following chapters. These concepts include information of the earth's ionosphere and physical plasma parameters, such as: plasma frequency, cyclotron frequency, and Debye length. A discussion on important waves in plasma is then presented, which include: electrostatic ion waves, upper hybrid waves, and Bernstein waves. Concepts of parametric instability and dusty plasmas are explained briefly, which is followed by a classification of study of space plasma into active and passive experiments. Active experiments are defined and explained in terms of their applications, followed by examples of active experiments and their current development. This research made contributions to two active experiments: the injection of artificial dusty plasma, and stimulated electromagnetic emission by high power radio wave radiation. Each of these experiments is introduced with its own, separate background. Finally, the scientific contributions made in this research work are listed.

2.1 Neutral Atmosphere and Ionosphere

Earth's atmosphere is a layer of several gases that surrounds the planet and is maintained by gravity. It extends up to approximately 500 km above the earth's surface, after which there is a transitional layer into interplanetary space. The majority of the earth's atmospheric mass is concentrated in its first 30 km from the ground up. There have been several studies conducted to learn more about the atmosphere. Now, with recent advancements in technology and more sophisticated instrumentation we are better able to understand the atmosphere and its functions.

The earth's atmosphere can be described and classified in several ways. Its stratification is characterized by a series of layers with specific distinctions, which can be applied as necessary to the physical process under consideration. Four commonly used classifications include:

- Classification via temperature (e.g. troposphere, mesosphere, etc.)
- Classification via chemical composition (e.g. homosphere, heterosphere, etc.)
- Classification via ionization (e.g. ionosphere, magnetosphere, etc.)
- Classification via dynamics/mixing (e.g. barosphere, exosphere, etc.)

The troposphere is the atmospheric layer closest to the earth; its boundary starts at the surface of the earth and extends to an altitude of about 9 km to 17 km. It consists of a major percentage (about 80%) of the atmospheric mass. The temperature in the troposphere decreases rapidly with higher altitudes, from about 20 to -52 °C. All weather phenomena occur within the troposphere, and its height varies with the seasons highest in the summer and lowest in the winter. The troposphere, along with its upper boundary, the tropopause, is known as the lower atmosphere.

The stratosphere is above the troposphere, and extends from the tropopause to about 50 km high. This is the second densest layer of air in the atmosphere, where the temperature increases with altitude (up to -3°C). The troposphere and stratosphere together consist of 99% of total atmospheric mass. The ozone layer plays an important role in regulating the thermal regime in this region the temperature rises with ozone concentration. The boundary between the stratosphere and the next layer up, the mesosphere is known as the stratopause.

The mesosphere extends from 50 to 85 km above the earth's surface. It is characterized by decreasing temperatures with altitude. In this layer most meteorites burn up upon entering the earth's atmosphere. This space debris forms a dust layer extending from 80 to 100 km above the earth's surface. The mesopause is the boundary between the mesosphere and thermosphere and is the coldest place on earth, where the temperature can drop down to -100°C. Due to these frigid temperatures water vapor freezes, thus forming ice clouds; the ice particle nucleates on the dust particles in this region form noctilucent clouds (NLCs). The stratosphere, stratopause, mesosphere, and mesopause are known as the middle atmospheric regions.

The thermosphere is the region above the mesosphere. This layer is characterized by an increase in temperature with altitude due to intense solar radiation. The temperature of this layer can rise to 1500°C. Unlike the stratosphere, thermal variation in this region is due to the low density of molecules. At these high altitudes molecules are widely separated, traveling kilometers before colliding with each other. This layer is known as the upper atmosphere.

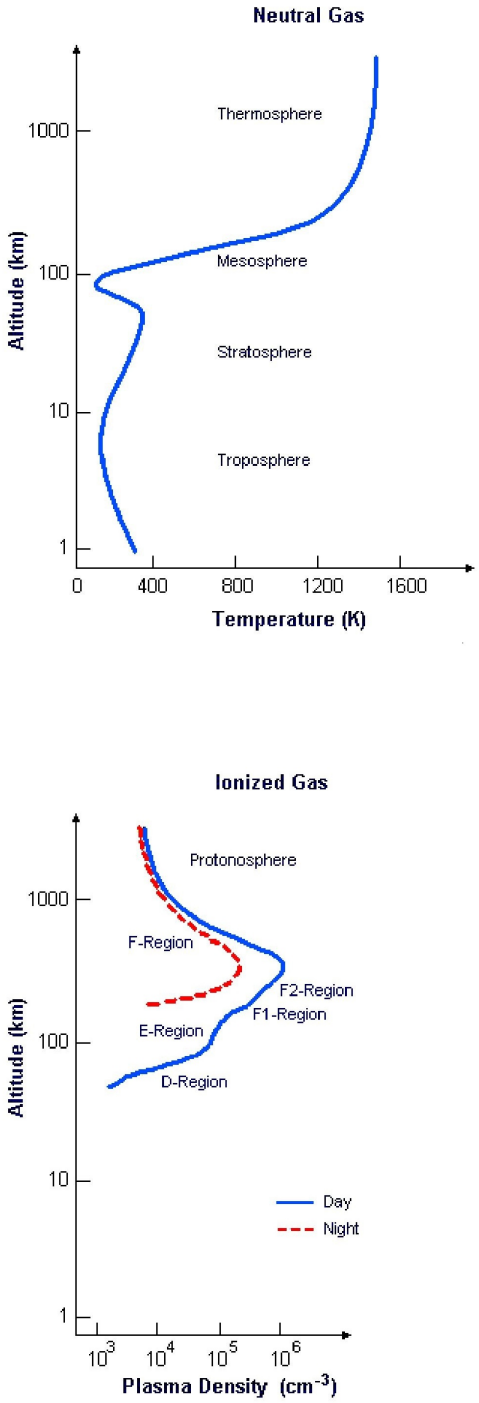

Figure 2.1: Classification of upper atmosphere altitude regions by temperature and ionization layer. Figure reproduced from Kelley, 1989.Used under fair use, 2013.

Another way of sectioning the earth's atmosphere is by observing the number of free electrons and other charged particles. Based on this, earth's atmosphere is divided into three layers: the ionosphere, plasmasphere and magnetosphere. Figure 2.1 shows the classification of the upper atmosphere altitude regions by temperature and ionization layer. In this work, we will focus on the ionization layer known as the ionosphere, which is essentially a plasma.

At high altitudes, radiation from the sun causes substantial photoionization of the upper atmosphere, which results in a significant number of free electrons and ions. These usually tend to recombine, but since the ionosphere has low gas densities, the recombination is slow. Due to this, the ionosphere is a region characterized by a relatively high-density concentration of both free electrons and ions. In general, any region that has this characterization is classified as a plasma. A plasma state is the fourth state of matter: heating a solid makes a liquid, heating a liquid makes a gas, heating a gas makes a plasma. At low temperatures collisions between atoms are rare, and these collisions do not have enough energy to ionize one or both atoms. However, as a gas heats up, the number of collisions between atoms increases, providing the gas with sufficient energy to ionize the atoms. At a certain point the number of ionized atoms will increase such that there is an abrupt change in the ratio between ionized and neutral atoms. At this point we are no longer talking about a gas, but a plasma. It is possible for a plasma to heat up enough that the number of ionized atoms will exceed the number of neutral atoms, thus fully ionizing the plasma. A plasma can also be considered a quasineutral gas of charged and neutral particles that exhibits a collective behavior.

The ionosphere- being a plasma and a conducting medium- supports propagation and reflection of radio waves, depending on their frequencies. This allows for long distance radio communication. The ionosphere is classified into vertical regions, which is continuously changing, varying from day to night, with the seasons of the year, and with the latitude. The different ionospheric layers are summarized in Table 2.1 with respect to their altitude and electron density range. D layer exists during daytime, when photoionization is higher due to sunlight. The E and F layers are the most important for radio communications in the frequency range of 3 to 30 MHz. Electromagnetic waves with a frequency above 40 MHz are able to penetrate through the ionosphere. In the D region, only waves of 2 MHz and below are reflected. This is because the D region has a much lower electron density than the other layers. The D region also has a much larger collision frequency, due to a high neutral density.

Table 2.1: Layers in Ionosphere

Layer	Approximate altitude	Electron density range
D	50-90 km	$10^2 - 10^4$ cm^{-3}
E	90-140 km	$10^4 - 10^5$ cm^{-3}
F	140-400 km	$10^5 - 10^6$ cm^{-3}

1. D-region (50 - 90 km) comprises the lowest part of the ionosphere and is characterized by high collision frequency due to high neutral density. Its electron density is in the order of $10^2 - 10^4$ cm^{-3}. Majority ion components of this layer are NO^+ and O_2^+, produced by ionization due to radiation of Lyman$_\alpha$ = 121.5 nm and high solar activity hard x-rays of < 1 nm respectively.

2. E-region (90 - 140 km). Electron density is in the range of $10^4 - 10^5$ cm^{-3}. It is the middle layer of ionosphere above the D layer. Ionization is due to soft x-ray of 1-10 nm and extreme ultraviolet (EUV) solar radiation, producing mainly O_2^+ and NO^+. The vertical structure of this layer is primarily due to ionization and recombination. At night this layer disappears rapidly since its primary source of ionization is absent. Sporadic E layer (Es) is generated within the E-region and is a thin layer of intense ionization.

3. F-Region (140 - 400 km), the highest layer, has the densest point of the ionosphere. Electron density is largest in this region of the order of $10^5 - 10^6$ cm^{-3}. The lower region of F is also known as F1 layer extending up to 200 km. The primary ion components of this region are NO^+, O_2^+ and O^+ ionized due to EUV radiation. Dominating molecular ion density is controlled by dissociative recombination. F2 is the layer extending above 200 km. O^+ is the dominating ion species of this region. Ionization of O is probably accompanied by N_2 ionization, which disappears rapidly after sunset. It has the maximum electron density of up to 10^6 cm^{-3} produced by charge transfer between major atomic ions and neutral species. F1 and F2 layers merge as a single F layer at night.

The F layer is the most complex layer with the largest plasma density. It is most widely used for HF propagation over long distances due to sky wave propagation, and is most strongly affected by solar radiation, meteors, artificial sources such as rocket/space exhausts and high power HF radio waves. Radio communication systems, navigation systems, etc., are vulnerable to these ionospheric disturbances. Thus understanding the development of irregularities in the plasma of this region is one of the most active areas of ionospheric research. This study concerns itself chiefly with plasma instabilities, which can be classified in several ways, although each classification is caused by waves produced by free particles in the ionosphere. The chemical composition of the ionosphere varies with altitude, and this plays an important role in the development of these irregularities. Electrostatic ion wave instability generated due to artificial ionospheric disturbances in the F region is the main focus in this research work.

2.2 Basic Plasma Concepts and Dusty Plasma

2.2.1 Basic Plasma Concepts

Plasma Oscillations and Plasma frequency

If the electrons in a plasma are displaced from a uniform background of ions, the electric field is set up, causing the electrons to be pulled back toward the much less mobile ions. Because of their inertia, the electrons overshoot and oscillate around their equilibrium positions with a frequency known as the plasma frequency ω_p . Their oscillations are so fast that the massive ions are assumed to be fixed. The plasma frequency is given by the expression:

$$\omega_p^2 = \frac{q^2 n_0}{m\epsilon_0} \tag{2.1}$$

where, ω_p is the plasma frequency; q, n_0, m are the charge, charge density, and the mass of the species respectively; and ϵ_0 is the permittivity of free space.

Cyclotron Frequency

If a magnetic field is applied on a charged particle, the particle will experience a cyclotron gyration with a frequency known as the cyclotron frequency ω_c. The cyclotron frequency is given by the expression

$$\omega_c = \frac{qB}{m} \tag{2.2}$$

where, ω_c is the cyclotron frequency; q, m are the charge and mass of the species respectively; and B is the applied magnetic field strength.

Debye Shielding

A fundamental characteristic of the plasma is its ability to shield out electric potentials that are applied to it. Suppose an electric field is applied into a plasma by connecting two charged metal surfaces to a battery. The charged surfaces would attract potentials of opposite charges and almost immediately a cloud of ions would surround the negatively charged surface while a cloud of electrons surrounds the positively charged surface. If the plasma were cold and there were no thermal motions, there would be just as many charges in the cloud as on the surface, and the shielding would be perfect. No electric field in this case would be present in the body of the plasma outside the cloud. On the other hand, if the temperature is finite, the particles that are at the edge of the cloud, where a weak electric field is present, would have enough thermal energy to escape from the electrostatic potential well. The edge of the

cloud occurs at the radius where the potential energy is approximately equal to the thermal energy kT, where k is Boltzman's constant and T is the temperature of the species, of the particles, and the shielding is not complete. Potentials of the order $kT = q$ can leak into the plasma and cause a finite electric field to exist [Chen, 1984]. A measure of the plasma shielding is called the Debye length λ_D, which is given by the following equation,

$$\lambda_D = \sqrt{\frac{\epsilon_0 k T_e}{n q_e^2}} \tag{2.3}$$

which is a measure of the shielding distance. Note that describing the plasma as a quasineutral gas means that it is neutral enough to assume $n_i = n_e = n$ where n is the plasma density.

Criteria of Plasmas

An ionized gas is called plasma if it satisfies the following three criteria:

- the Debye length is much smaller than other physical dimensions of interest, for example, the plasma system length
- there are a lot of charged particles inside a "Debye sphere" whose radius equals a Debye length, in order to enable the Debye shielding to be statistically valid
- the collision frequency between charged and neutral particles is small compared with the frequency of typical plasma oscillations. In other words, $\omega_p \tau > 1$, where τ is the mean time between collisions with neutral atoms.

The upper ionosphere meets all three of these criteria, and is therefore considered a plasma.

Electrostatic Ion Waves Perpendicular to B_0

Assume k, the wave vector, is almost perpendicular to the background magnetic field B_0. Assume also that an infinite plasma in equilibrium with uniform density, n_0 and magnetic field B_0. Also the assumption of cold ions is considered, i.e $T_i = 0$. The geometry is shown in Figure 2.2. The angle $\pi/2 - \theta$ is taken to be so small that we may take $E = E_1 \hat{x}$ as far as ions are concerned. For the electrons, however, it makes a great difference whether $\pi/2 - \theta$ is zero or small and finite. The electrons have such small Larmor radii that they cannot move in the x-direction to preserve charge neutrality; all that the E field does is make them drift back and forth in the y direction. If θ is not exactly $\pi/2$, the electrons can move along the dashed line (along B_0) to carry the charge from negative to positive regions in the wave and carry out Debye shielding. The ions cannot do this effectively because their inertia prevents them from moving a long distance in a wave period. This critical angle $\pi/2 - \theta$

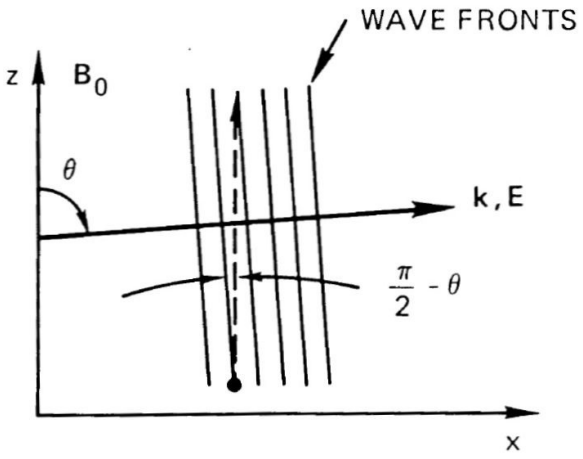

Figure 2.2: Geometry of electrostatic ion waves. Figure reproduced from Chen, 1984. Used under fair use, 2013.

is proportional to the ratio of ions to electrons' thermal velocity which is proportional to $\sqrt{m_e/m_i}$. Considering the plasma approximation $n_e = n_i$, the dispersion equation of the ion cyclotron waves is obtained [Chen, 1984], which is given by:

$$\omega^2 = \Omega_i^2 + k^2 v_s^2 \tag{2.4}$$

where, Ω_i is the ion cyclotron frequency, k is the wave number, and v_s is the electron oscillating velocity.

Now, consider the case with θ is exactly equal to $\pi/2$, and the electrons are not allowed to preserve their charge neutrality by flowing along the lines of force. Assuming also that the electron mass is finite and considering the plasma approximation, we obtain the frequency called the lower hybrid frequency [Chen, 1984], which is given by:

$$\omega_{lh} = \sqrt{\frac{\omega_{pi}^2}{1 + \omega_{pe}^2/\Omega_e^2}} \tag{2.5}$$

where Ω_e and Ω_i are the electron cyclotron and ion cyclotron frequencies respectively. Note that the lower hybrid oscillations are only observed when θ is very close to $\pi/2$.

Upper Hybrid Waves

Assume that high-frequency electrostatic electron oscillations propagate at right angles to the background geomagnetic field. These electrostatic electron waves across B will oscillate with the frequency, called the upper hybrid frequency, ω_{uh}. The upper hybrid frequency is given by:

$$\omega_{uh}^2 = \omega_{pe}^2 + \Omega_e^2 \tag{2.6}$$

where, ω_{uh} is the upper hybrid frequency; ω_{pe} is the electron plasma frequency; and Ω_e is the electron cyclotron frequency. Note that these are different oscillations than those along B which are the usual plasma oscillations, with $\omega = \omega_p$.

Bernstein Waves

Bernstein waves are electrostatic waves propagating at right angles to B at harmonics of the cyclotron frequency, $n\Omega$.

Parametric Instability

Ion density fluctuations may couple an electromagnetic wave into an electron plasma wave to give us an electric field $\vec{E}$. In turn, the electron plasma wave beats with the electromagnetic wave to generate a spatial variation in the electric field intensity that can enhance the ion density fluctuations via the ponderomotive force. Hence, a feedback loop is formed and depending on the pump amplitude, instability can result. Such instability is called parametric instability, with the parameter being the wave's amplitude.

In order for the parametric instability to occur, a minimal set of common characteristics is required:

- Matching conditions - The spatially varying electric field E_0 which results from the beating of two waves, requires a two-wave number matching condition to produce sustaining instability. Mathematically,

  $$k_0 = k_i + k_s \tag{2.7}$$

  where the scripts $0, i$ and s stand for the pump, idler and the signal respectively. In the SEE problem, the electromagnetic wave is the pump, the electron plasma wave is the idler, and E_0 is the signal. The wave number matching condition is equivalent to conservation of momentum. The parametric instability also has to satisfy the conservation of energy to take place. This translates into the frequency matching condition

  $$\omega_0 = \omega_i + \omega_s \tag{2.8}$$

- Threshold - The instability can occur only when the pump amplitude is above a critical value in order to maintain the feedback growth. If the pump amplitude is below the instability threshold, even a small amount of either collision or Landau damping will prevent the instability from occurring.

Figure 2.3 shows the parallelogram construction for the parametric decay instability process. Here, (ω_0, k_0) is an incident electromagnetic wave of large phase velocity $\omega_0/k_0 \approx C$. It excites an electron wave and an ion wave moving in opposite directions. Since k_0 is small we have $|k_1| \approx -|k_2|$ and $\omega_0 = \omega_1 + \omega_2$ for this instability.

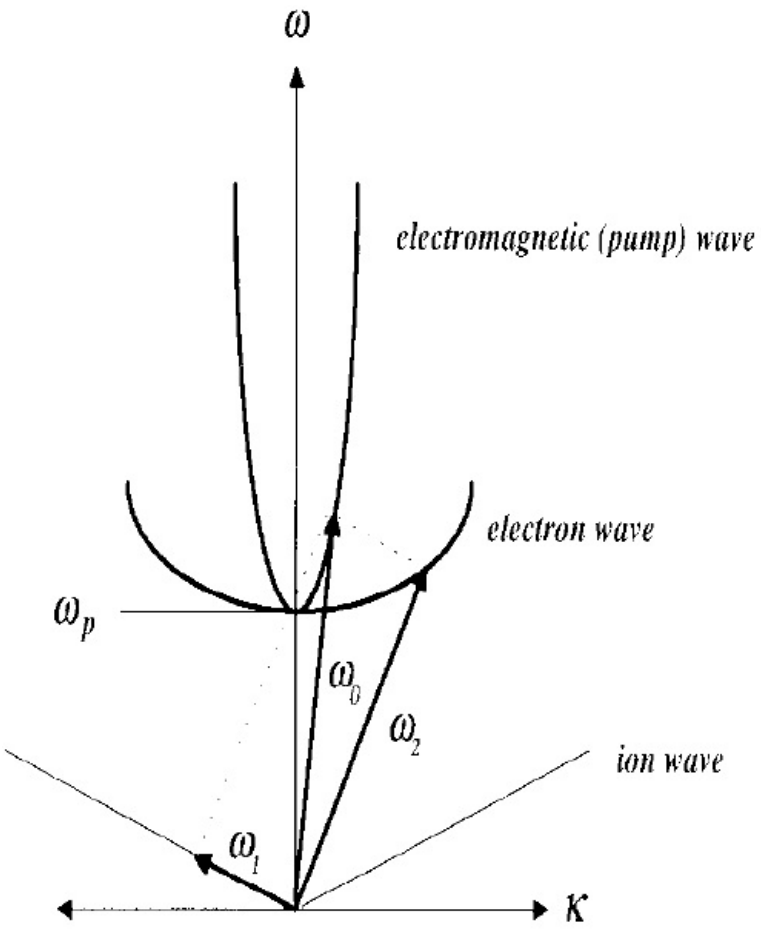

Figure 2.3: Parametric Decay Instability Process. Figure reproduced from Chen, 1984. Used under fair use, 2013.

2.2.2 Dusty Plasma

Dusty plasma is a plasma containing nanometer or micrometer-sized particles suspended within it. The interaction of dust particles with background plasma results in the charging of dust particles. Background plasma and charged dust particles behave as plasma following electromagnetic laws. This makes dusty plasma interesting and technologically important. The dynamics of these massive charged particles occurs on considerably slower time scales than the ordinary plasma ions, since their charge to mass ratio is orders of magnitude smaller than that of the corresponding (e/m) electrons or ions. Dust is found everywhere, for example, in cosmic plasmas, planetary plasmas, plasmas near the earth, and plasmas in the laboratory. Dust occurs in both natural and artificial (man made) forms. Interplanetary medium, planetary ring systems, volcanoes, meteoric dust, and noctilucent clouds in the mesosphere are some examples of naturally occurring dusty plasma. Some examples of man-made dust plasma include rocket exhaust, atmospheric aerosols, dust on surfaces in space,

dust in fusion devices, and dusty plasma devices used to produce and study dust plasmas in laboratories. Dust particles come in a variety of shapes (e.g., sphere, rods etc.), and materials such as dielectric or conducting.

Debye Shield and Intergrain Spacing

We consider a multi-component dusty plasma composed of electrons, singly charged positive ions, and massively charged dust grains, in a neutral background. The dust grain radius r_d is usually much smaller than the dusty plasma Debye length λ_D. When the intergrain spacing, a, is much smaller than the Debye length, $a << \lambda_D$, the charged dust particulates can be treated as massive point particles similar to multi-charged negative (or positive) ions in a multi-species plasma. When the dust particles' spacing is smaller than the Debye length, $a < \lambda_D$, the charged dust particles participate in a collective behavior corresponding to dusty plasma. The dust particles then can be considered as massive point particles where the effect of neighboring particles can be significant. For dust-in-plasma, $a > \lambda_D$, the dust particles are completely isolated from their neighbors.

Charge on Dust Particles

The charge Q on a dust particle is given by

$$\frac{dQ}{dt} = \sum I_j \tag{2.9}$$

where I_j are the currents on dust particles due to different plasma species. The currents depend both on the properties of the dust particles such as velocity distribution and size and on the ambient plasma conditions.

Coulomb Coupling

Charged dust grains can be either weakly or strongly correlated depending on the strength of the Coulomb coupling parameter

$$\Gamma_d = \frac{Q_d^2}{aT_d} exp(-a/\lambda_D) \tag{2.10}$$

where $a = (3/4\pi n_{d0})^{1/3}$ is the intergrain spacing, n_{d0} is the initial dust density, Q_d is the dust charge, T_d is the thermal energy. When $\Gamma_d >> 1$ the dust is strongly coupled, while dust plasma is considered weakly coupled when $\Gamma_d << 1$. When the dust is weakly coupled, the dispersion relation of waves is not affected by the spatial correlation of the dust grains. The dust grains used in the model in this work are assumed to be weakly coupled, where the charged dust microspheres cannot strongly interact with each other.

Forces on Dust Particles

To understand the dynamics and transport of dust particles it is important to know the various forces acting on these dust particles. Some examples of different types of forces on dust particles are gravitational, electric, and drag force.

Formation and Growth of Dusty Particles

Dust particles can be formed (and grow in size) in plasmas that contain chemically active species, such as plasma devices in the semiconductor processing industry. Particle growth in plasma is thought to be produced due to nucleation, coagulation and surface growth. Nucleation is essentially a chemical reaction in the gas phase, forming small clusters of particles. Coagulation is when two particles collide to form a larger particle and surface growth is when plasma radicals stick to existing particles.

2.3 Active Experiments

Space weather is a continuously changing phenomenon produced by the interaction of the sun's atmosphere with the earth's upper atmosphere (ionosphere and magnetosphere). This near-earth space environment causes several effects that degrade our satellite communication systems, navigation systems, electric power systems, etc. These orbital communication networks are growing by leaps and bounds, and we are increasingly becoming more and more dependent on them. But this technology is vulnerable to the space environment around earth. Numerous investigations and studies have been conducted to better understand space weather, and the ultimate goal of such works is to accurately predict its phenomena. This can be explored by studying properties of plasma in space. There are numerous kinds of experiments conducted for the same purpose, and most of these experiments can be broadly classified as active and passive experiments.

- Active Experiments: In this kind of experiment, the natural environment of the plasma is perturbed with artificial elements and the effects on the plasma are investigated.
- Passive Experiments: In this kind of experiment, the space plasma is observed with either ground-based or satellite instruments, and its naturally changing properties and irregularities are investigated.

Rather than observing purely natural phenomena, space physicists have been conducting controlled experiments in the ionospheric and magnetospheric plasmas; for example, the modification of the space plasma with injection of chemical compounds; injection of artificial dust into the space plasma; ELF and VLF wave generation by HF heating using ground-based

heating facilities, such as the High-Frequency Active Auroral Program (HAARP); generation of stimulated electromagnetic emission (SEE) by stimulation radiation using HAARP; etc. In such experiments, the near-earth space environment is deliberately perturbed by the injection of a signal that has known characteristics; this signal may be in the form of energetic charged particles or radio wave. The effect of this perturbation is then studied to better understand the environment or similarly occurring natural phenomena. These experiments are known as active experiments.

During the 1960s, space plasma in the ionosphere and the magnetosphere was primarily investigated with passive techniques, where ground-based and satellite-based instruments monitored the naturally changing phenomena. By next decade the methods of observations were broadened to include active experiments, in which local space plasmas were modified with a well-defined perturbation and its response was investigated [Kivelson and Russell, 1973]. These active experiments were performed with the primary applications of measurements of preexisting fields and perturbation of system. The artificial perturbation of space plasma has the following applications:

- in the study of basic physics of the near-earth space environment. Plasma processes existing inside the ionospheric plasma can be destabilized and their generation and evolution can be studied with ground- or space-based instruments.
- in controlling of some physical process in the near-earth space environment. Ionospheric disturbances degrade communication systems, and artificial stimulant can be used to identify and characterize the ionospheric processes so that techniques can be developed to mitigate or control them.
- in studying naturally occurring phenomena. The ionosphere is rich in natural processes, such as PMSE's; particle acceleration can be investigated in a controlled experiment with an artificial stimulant with known properties.

2.3.1 Examples of Active Experiments

Ionospheric modification experiments are conducted by employing a known stimulant in a controlled manner. Depending on the kind of stimulant, there is a broad range of active experiments being investigated today. The following are some examples of ionospheric modification in which the stimulant signal is artificial dust/aerosol or radio beam.

Ionospheric modification with artificial dust release

Charged Aerosol Release Experiment (CARE) injects layers of artificial dust into the ionosphere. Artificial or man-made dust has been injected into the ionosphere since man started

venturing into outer space. Aerosol particles released from rocket and shuttle exhaust interacts with the ionosphere to produce a wide range of disturbances. An early detected effect of exhaust on the ionosphere was the so-called "ionospheric holes" or "bite-out" in the electron density created during the Skylab workshop of the Saturn 5 rocket launch reported by Mendillo et al., 1975a. This rapid reduction in the electron density was almost undetected due to the limited number of ionosonde stations along the Atlantic coast and their degradation by geomagnetic activity. Fortunately, the Faraday rotation technique of determining total electron content, which was used here, has the capability of withstanding even the most severe types of ionospheric disturbances capable of being induced by solar, geomagnetic, or even man-made activity. A similar ionospheric hole was observed using the Faraday rotation to detect total electron content (TEC) during an earlier launch of the NASA rocket in 1962 [Jackson et al., 1962]. The mechanism in the generation of these holes was the rapid ion-atom interchange reactions between the ionospheric O+ and the hydrogen and water vapor molecules in the plume, followed by dissociative recombination of the molecular ion [Mendillo et al., 1975a and 1975b]. A detailed study of theory and experiments on ionospheric holes has been provided by Mendillo, 1988, where different mechanisms for the generation of ionospheric holes are explained: e.g., snow plow effects, plasma depletions, electron attachments. Since the discovery of the ionospheric hole during rocket launches, several of such experiments were conducted to investigate the types of disturbances created by rocket exhaust plumes. Recently, Bernhardt et al., 2012 provided a detailed report on the long range measurements done by ground- and space-based instruments during emission of rocket exhaust plumes conducted in experiments such as: CARE (Charged Aerosol Release Experiment), SIMPLEX (Shuttle Ionospheric Modification with Pulse Localized Exhaust Experiment), and SETIE (Shuttle Exhaust Ionospheric Turbulence Experiment).

There have been several applications in studying rocket release exhaust including: the behavior of dust particulates in background plasma in initial dust layer creation phase, and the study of radar backscatter associated with regions near NLCs by rocket dust release, which validates radar theory in dusty plasmas. Additional applications include the generation of ionospheric holes or bite-outs in electron density, and creation of artificial air glow. The generation of plasma instabilities in the expanding dust/aerosol cloud has been a topic of interest recently due to possible enhanced radar backscatter from the expanding dust plume in the ionosphere. Bernhardt et al., 1995 considered the dust acoustic instability, arising from a relative drift between the charged dust (ice) particles and the background plasma ions and electrons, since the exhaust vapors have a velocity relative to the background atmosphere. The excitation of ion waves in the exhaust plume by a charged dust beam drifting through the background electron and ion plasma, using the parameters of Bernhardt et al., 1995 were considered by Bharuthram and Rosenberg, 1998. It was suggested that these instabilities might occur on the dust time scale. Numerical analysis of dust acoustic instability, driven by the ion beam using a one-dimensional hybrid model, was provided by Winske and Rosenberg, 1998. A two-dimensional theoretical model of ion-dust streaming instability was investigated for conditions representative of plasma sheath by Rosenberg, 1996. The investigation of lower hybrid waves generated by a charged dust beam through background

plasma with magnetic field was provided by Rosenberg et al., 1999. Scales et al., 1998 investigated wave generation in expanding dust clouds into a plasma with a magnetic field due to velocity-shear driven instabilities in the dust cloud boundary. Detailed numerical analysis of low-frequency ion waves and instabilities in a magnetized two dimensional plasma were provided by Chae et al., 2000. The code used for analysis was the hybrid code with fluid electrons and ions and dust treated as particles. In particular, the effects of dust charging on the low-frequency instability were studied. This work was further developed to investigate shear driven lower hybrid instability developed in expanding dust across the magnetic field in the ionosphere by Scales et al., 2010. An analysis of plasma turbulence generated in injected artificial dust clouds using numerical techniques has varied applications including its predicting capability for experimental observations during active experiments. The simulation models can be used under different scenarios and this broadens its applications to artificial as well as natural dusty plasma in interplanetary space, laboratory dusty plasma etc. This research work provides one such model applied to the investigation of lower hybrid turbulence.

Ionospheric modification with radio beam

There are many heating facilities around the world used for active experiments including: HAARP at Gakona, AK; EISCAT at Tromso, Norway; HIPAS near Fairbanks, AK (currently decommissioned); SURA near Nizhny Novgorod, Russia; Aercibo in Puerto Rico; and Jicamarca in Peru. The High-frequency Active Auroral Research program (HAARP) is the most powerful heating facility used in ionospheric modification experiments, located in Gakona, AK. Figure 2.4 shows a photo of the phased array transmitter consisting of 180 crossed dipole antennas arranged in a rectangular planar array capable of delivery up to 3.6MW power. The two pairs of crossed dipole antennas are mounted on each of the 180 towers. The two antennas are used for low band (2.8-8.3 MHz) and high band (7-10 Mhz). Each tower is 72' high mounted on thermopiles spaced 80' apart in a 12×15 grid. A ground screen is elevated at about 15' height. There are 30 shelters mounting 6 pairs of 10 kW transmitters. Each shelter provides power to antennas that are mounted on 30 towers. Thus a 6×2×30×10 kW = 3.6 MW of full power can be generated at this facility. The ground screen is a reflector of the antenna array and it allows access to the shelters housing the transmitters. The entire structure is fenced for protection. Various diagnostics instruments, such as, riometer, magnetometer, digisonde, VHF radar, MUIR radar, etc. are installed in the HAARP research facility and/or locations in Alaska.

HAARP is used for a number of ionospheric modification experiments such as: generation of ELF/VLF waves, generation of field aligned ionization, creating artificial ionospheric layers, etc. The ELF/VLF waves are produced in nature by lightning discharge and the wave packet generated propagates in the natural waveguide, the ionosphere, with a group velocity close to the speed of light. The investigation of the generation of these waves and the manner in which they propagate in and scatter from various regions of the upper atmosphere is

Figure 2.4: Photograph of the HAARP antenna array

used as a diagnostic tool to investigate physical processes in the earth's ionosphere. The generation of ELF and VLF waves through a process called modulated heating has been carried out at HAARP since 1999 [Milikh et al., 1999, Rodriguez et al., 1999]. HAARP is used to modulate the conductivity of the ionosphere which then modulates ionospheric currents such as the auroral electrojet. Recently, a new technique has been developed to use HAARP efficiently to generate ELF waves using geometric modulation of the heater beam [Cohen et al., 2008, 2010]. The increased efficiency creates new possibilities for many applications including communications, radiation belt remediation, etc. HF heating of the ionosphere produces patches of ionization that are aligned with the geomagnetic field, thus producing scattering centers for RF waves. Natural processes also produce such scatterers, as evidenced by the scintillations observed on satellite-to-ground links in the equatorial and high latitude regions. The generation of artificial field-aligned irregularities using a heater provides a controlled way to study the natural physical processes. E-region artificial field-aligned irregularities were first observed by coherent scatter radar by Fialer 1974. Since then there have been several observations made at the radar facility at Tromso. The upgrade in HAARP which allows heating at low frequency (2.75 MHz) has allowed for the generation of FAI in the E-region [Nossa et al., 2009]. Several experiments conducted using heating above the E-region's critical frequency have appeared to produce artificial field aligned irregularities (AFAI) in both the E- and F1- regions. These provide applications in many fields such as communications-HF propagation around the world, and means of diagnosing neutral winds and background electric fields. Recent work by Hysell et al., 2011 have shown that X-mode heating can suppress AFAI generated by O-mode heating. By staggering the O-mode and X-mode pump frequencies, broad spans of the lower thermospheric profile could be interrogated [Hysell et al., 2011]. The use of very high power RF heaters to accelerate electrons to 14-

20 eV opens the way for the creation of substantial layers of ionization at altitudes where normally there are very few electrons. Recently, Pederson et al., 2010 reported for the first time evidence of an artificial ionosphere generated using HAARP. The initial heating was at 220 km with radio wave frequency near the second electron gyro-harmonic frequency. Once the artificial plasma reaches sufficient density to support interaction with the transmitter beam it rapidly descends as an ionization wave to 150 km altitude. This new ability to produce substantial artificial plasma in the upper atmosphere (developed by Mishin, 2011) opens the door to a new regime in ionospheric radio wave propagation where transmitter-produced plasmas dominate over the natural ionospheric plasma and may eventually be employed as active components of communications, radar, and other systems. A numerical model of generation of artificial ionosphere by HF transmitters was presented by Eliasson et al., 2012. This code simulated the strong Langmuir turbulence generated by the transmitter, which is an input to the simulated creation and descent of an artificial ionospheric layer.

These new discoveries during active experiments suggest that the study of the ionosphere is still in its early stages and there is a great deal to learn about its physics, chemical composition, and the physical processes that are generated in it due to its interaction with solar radiation. This research is one such step in understanding plasma turbulence generated in the lower hybrid and ion-ion hybrid frequency range. The two active experiments discussed in this research work- aerosol release and stimulated radiation- study naturally occurring phenomena of the dust layer, and investigate the ionosphere in the F-region during active magnetic conditions, respectively.

2.3.2 Artificial Dusty Plasmas/CARE

From Section 2.1 we know that a natural dust layer formed by tons of meteoric dust spans an altitude of 80 to 100 kilometers within the earth's upper mesosphere and lower thermosphere. Noctilucent Clouds (NLC) are visual manifestation of these dust layers. NLCs are the highest clouds in the earth's atmosphere, and are visible in deep twilight. They are most commonly observed in the summer months at latitudes between 50 and 70 north and south of the equator. They can only be observed when the sun is below the horizon, after which they are lit from underneath and the light reflected at a low angle picks out the many waves which cross the cloud layer. NLCs appear as a thin but distinct cloud layer well above the visible part of the atmosphere. They appear to be about twice the distance from the horizon than the visible thickness of the atmosphere. To the eye, they look like a thin shell of glowing wisps suspended above our atmosphere in the blackness of space. An image of NLC can easily be obtained from internet- one such picture is shown in Figure 2.5. This photo was taken on July 30, 2009 at 22:15UT by Pekka Parviainen, just after sunset in southern Finland. The orange hues are of the sunset and the blue-white luminous streaks are from the NLCs. The nature of noctilucent clouds is not fully understood; in fact NLCs are a recently-discovered meteorological phenomenon. There is no evidence of the existence of this phenomenon over 120 years ago. These clouds are composed of tiny crystals

Figure 2.5: Noctilucent Clouds over Finland on a summer evening. [Photograph taken by Pekka Parviainen]

of water ice up to 100 nm in diameter and exist higher than any other clouds in earth's atmosphere. Clouds in the earth's lower atmosphere form when water collects on particles, but mesospheric clouds may form directly from water vapor in addition to collecting on dust particles. The conditions of the mesopause are suitable for ice particle formation and growth only during summer months, both for the temperature and the humidity, since summer is the only time when the stratosphere allows the right kind of vertical waves to propagate to the mesosphere and provide the necessary influx of eastward momentum. Noctilucent clouds are known to exhibit high radar reflectivity. The charging of the dust density in NLCs generates irregularities in electron density above the NLC altitude which scatter radar echoes, called Polar Mesospheric Summer Echoes. Because of the intimate relationship between these phenomenological signatures and the global environment, the study of such dust layers is a forefront issue in upper atmospheric space science.

Most studies of NLCs have been limited to ground-based observations, and scientists had very little knowledge of the mesosphere until the 1960s, when direct rocket measurements began. Space observations led to closer observations of the mesosphere's coldest region all the way to the geographic poles. These experiments showed for the first time that the occurrence of the clouds coincided with very low temperatures in the mesosphere. Noctilucent clouds were first traced across the polar cap from space by an instrument on the OGO-6 satellite in 1972. The OGO-6 observations identified a bright scattering layer over the polar caps as poleward extensions of these clouds. Since then, numerous space-based studies have been conducted in the investigation of NLCs. For instance, on April 25, 2007, the AIM satellite (Aeronomy of Ice in the Mesosphere) was launched, the first satellite dedicated to studying noctilucent clouds, and made its first observations on May 25, 2007. Images taken by the satellite show shapes in the clouds that are similar to shapes in tropospheric clouds, hinting

at similarities in their dynamics.

The Charged Aerosol Release Experiment (CARE) was the alternative method in studying the natural dusty plasmas associated with polar mesospheric clouds, which have been shown to scatter radar echoes. It was an active ionospheric modification experiment which examined the creation of an artificial dust layer and the subsequent ionospheric turbulence. Its objective was to study the effect of the artificial layer of charged dust particulate on the UHF, L-Band and S-Band radars [Bernhardt, 2011]. The experiment was set to launch a series of rockets to test the theory of radar scatter from charged dust. On September 19, 2009 CARE became the first rocket experiment to use a chemical release for this purpose. A Nihka motor on the rocket released Al_2O_3 and about 200 kg of neutral molecule vapor at 280 km. Figure 2.6 shows a schematic diagram of the launch of the rocket, its trajectory, and release of charged dust cloud.

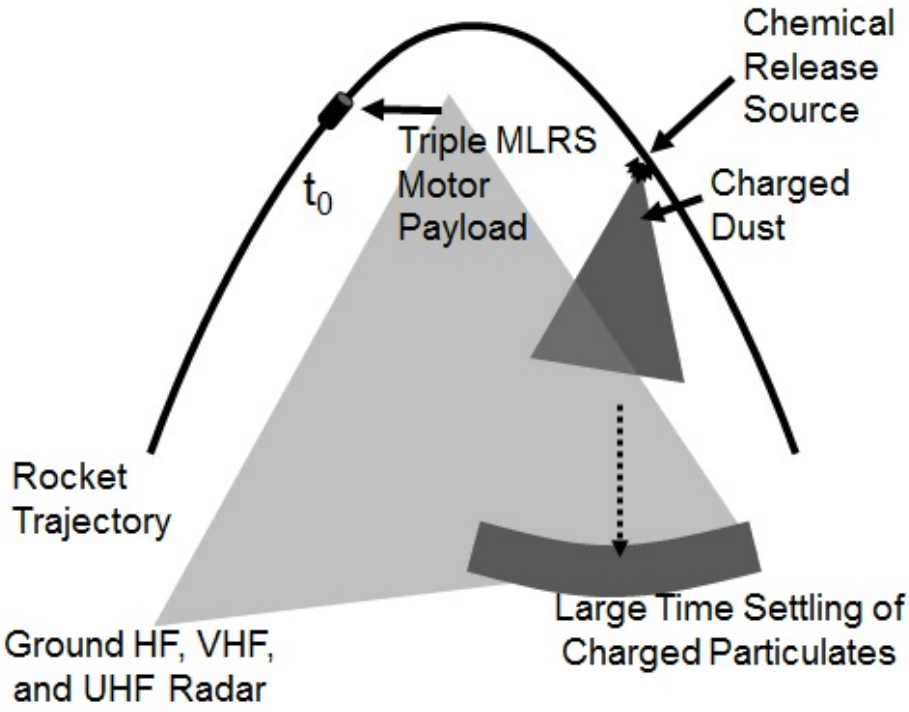

Figure 2.6: Charged Aerosol Release Experiment (CARE) schematic of rocket launch trajectory and dust injection source. Figure reproduced from Bernhardt, 2009. Used under fair use, 2013.

The sounding rocket was launched from NASA's Wallops flight facility. This rocket for the CARE I project was configured as a Black Brant XII with the Nihka motor used as the payload to release dust and (neutral) molecules into the upper atmosphere. One third of the released mass was Al_2O_3 and two-thirds was neutral molecules, consisting of H_2, H_2O, CO_2, N_2, HCl, and CO. This large amount of neutrals displaced the background ionospheric

plasma. The dust and neutrals released into the ionosphere could drive ionospheric instabilities. Artificial airglow was observed as the dust cloud was released. The exhaust molecules exchanged charge with the atomic oxygen in the ionosphere to ionize molecular ion. By dissociative recombination this ion then rapidly recombined with electrons. The excited electronic states relaxed to produce photons which were observed as the airglow. Figure 2.7 shows the images of the initial dust release as seen from the ground and the dust ring along with the red glow of red lines emissions from atomic oxygen.

Figure 2.7: (left) Dust and neutral exhaust release and (right) dust ring and red lines emission. Figure reproduced from Bernhardt et al., 2011. Used under fair use, 2013.

The fourth stage was fired in such a way that the Nihka motor opposed the downward motion and chemical released at a constant altitude. The dust cloud was released at 3 km/s speed in 17.79 seconds [Bernhardt et al., 2011]. My contribution to this experiment was to model the creation and evolution of the dust layer. This model simulated the generation of lower hybrid turbulence (few kHz frequency range) with two different mechanisms at two different time scales. The first one developed at the beginning of the dust cloud release (few 10's of milliseconds) and the second one, a few seconds after the dust was released. The analysis of the two turbulences using the models is presented in this research, and the results are checked for agreement with the linear theory. The two turbulences are compared and contrasted.

2.3.3 Stimulated Electromagnetic Emission

A high-frequency radio wave transmitted from the ground into the ionosphere can interact with local ionospheric plasma and excite a wide range of plasma processes. In order to understand these plasma processes generated due to active modification of the ionosphere, appropriate instruments were required for diagnosis. These include, to name a few: HF receivers for the detection of stimulated electromagnetic emissions from heater induced turbulence in the ionosphere; HF/VHF radars, to determine the amplitudes of short-scale geomagnetic field-aligned irregularities; optical imagers, to view artificially produced airglow; scintillation measurements using satellites; in situ measurements by rocket borne instruments; a chain of ELF receivers to record signal strengths at various distances from the heater; a digital HF ionosonde, to determine background electron density profiles in the E- and F-regions; a magnetometer chain, to observe changes in the earth's magnetic field in order to determine large volume ionospheric currents and electric fields; and, a riometer, to provide additional data, especially for disturbed ionospheric conditions. HF receivers that monitor the ionospheric plasma response to electromagnetic pumping have provided rich data. Electromagnetic emissions stimulated by the radio wave (pump wave) in the interaction region at an altitude of few hundred kilometers that has escaped the ionospheric plasma is observed by the receivers. This pump induced radiation is called stimulated electromagnetic emissions.

For the past few decades, since the discovery of Stimulated Electromagnetic Emissions (SEE)in experiments conducted at the HF heating facility near Tromso, Norway, by Thide et al., 1982 there has been considerable amount of interest in the process of generation of spectral features in SEE and its diagnostic capabilities. SEE are high-frequency (HF) radio emissions that are generated as a result of a complicated series of interactions between a high-power, ordinary mode (O-mode), HF radiowave pump (the heater), and internal plasma waves in the ionized upper atmosphere. The internal waves include upper hybrid, lower hybrid, and ion cyclotron waves. The SEE spectrum exhibits sidebands that are upshifted and downshifted from the pump wave within roughly about several tens of kHz bandwidth.

We participated in two campaigns at the High-frequency Active Auroral Research Program (HAARP), Gakona, AK, during the summer of 2010 and 2011 to conduct stimulated electromagnetic emissions experiments. A physical model for the generation of SEE is shown in Figure 2.8. The SEE receiver was used to measure the stimulated radiation signal.

SEE provides a window on the ionosphere when perturbed by HF transmitters. It is a very important diagnostic tool for studying parametric instabilities and other nonlinear physical processes that may occur around the heated region. SEE is such an important diagnostic tool that it is also considered a fundamental plasma phenomenon. The spectral features in the SEE contain diagnostic information about the ionosphere; for instance, the SEE spectral features can be employed:

1. to determine the local magnetic field magnitude [Leyser et al, 1992]. When a HF radio wave is injected vertically at frequencies near high harmonics of f_{ce}, a prominent lower

sideband, DM, is suppressed in an extremely narrow range of pump frequency. This DM feature is known to disappear when the pump frequency passes through the local electron cyclotron frequency (f_{ce}). The local magnetic field magnitude can hence be calculated with an accuracy of 1 nT because of the narrow bandwidth of absorption resonance.

2. to measure electron temperatures [Bernhardt et al., 2009]. An HF electromagnetic wave can decay into an ion acoustic wave and a scattered electromagnetic wave by a process called Stimulated Brillouin Scatter (SBS). A dispersion relation equation for ion acoustic wave and electromagnetic waves that keep all of the effects of the ion and electron gyro frequencies was developed, providing an analytic expression that yields measurements of the electron temperatures in the heated ionosphere.

3. to measure ion composition [Bernhardt et al., 2010]. HF electromagnetic waves can excite low-frequency electrostatic waves by magnetized Stimulated Brillouin Scatter. Either an ion-acoustic wave with a frequency less than the ion cyclotron frequency (fCI) or an electrostatic ion cyclotron (EIC) wave just above fCI can be produced for propagation along the magnetic zenith and with oblique propagation angles respectively. The ion composition can be obtained from the measured EIC frequency.

The transmitted pump wave interacting with local plasma may generate different types of waves, instabilities, and turbulence, and as a result a variety of spectral features in the scattered wave are expected. Parametric decay of the high-frequency pump wave, transmitted from the ground into other plasma wave modes, is considered to be the underlying theory for a generation of the features in the SEE spectrum [Leyser et al., 2001]. The EM pump wave can be directly involved in the decay process, which scatters new EM and ES waves. For example, decay of the pump field into ion acoustic or electrostatic ion cyclotron waves and scattered EM waves is involved in the Stimulated Brillouin Scatter process [Norin et al., 2009; Bernhardt et al., 2009, 2010]. These decayed waves are seen as strong SEE spectral sidebands. On the other hand, for other SEE features, the EM pump undergoes conversion to another ES wave first, which then decays into new ES waves. These ES waves can be a high-frequency ES wave and irregularities converted due to oscillating two stream instability (OTSI) [Dysthe et al., 1983, Huang and Kuo, 1995]. The ES waves could be high-frequency and low-frequency waves and finally the high-frequency ES wave then converts back to EM waves, which propagates to the ground. For example, the downshifted maximum (DM) spectral feature is proposed to be generated by this process [Zhou et al., 1994; Bernhardt et al., 1994]. DM is a distinct peak at a frequency approximately 5-10kHz below the pump frequency. It involves an interaction of low-frequency lower hybrid waves and high-frequency upper hybrid waves [Bernhardt et al. 1994; Huang and Kuo, 1995]. The most important upshifted feature in the SEE spectrum is the broad upshifted maximum (BUM) usually seen when the pump frequency is above the electron gyro-harmonic frequency (nf_{ce}). It was noted by Leyser et al., 1989 that the BUM feature could be generated through a four-wave interaction process involving two pump photons or upper hybrid plasmons, a decay mode

at nf_{ce}, and the stimulated radiation at f_{BUM}. When the heater frequency f_0 is above an electron cyclotron harmonic nf_{ce}, frequency upshifted upper hybrid waves and frequency downshifted electron Bernstein waves can be excited above the upper hybrid resonance layer via the considered four-wave process. [Huang and Kuo, 1994] have proposed that the BUM is produced in the region where the pump frequency is about the mean of the upper hybrid wave frequency and the electron Bernstein wave frequency.

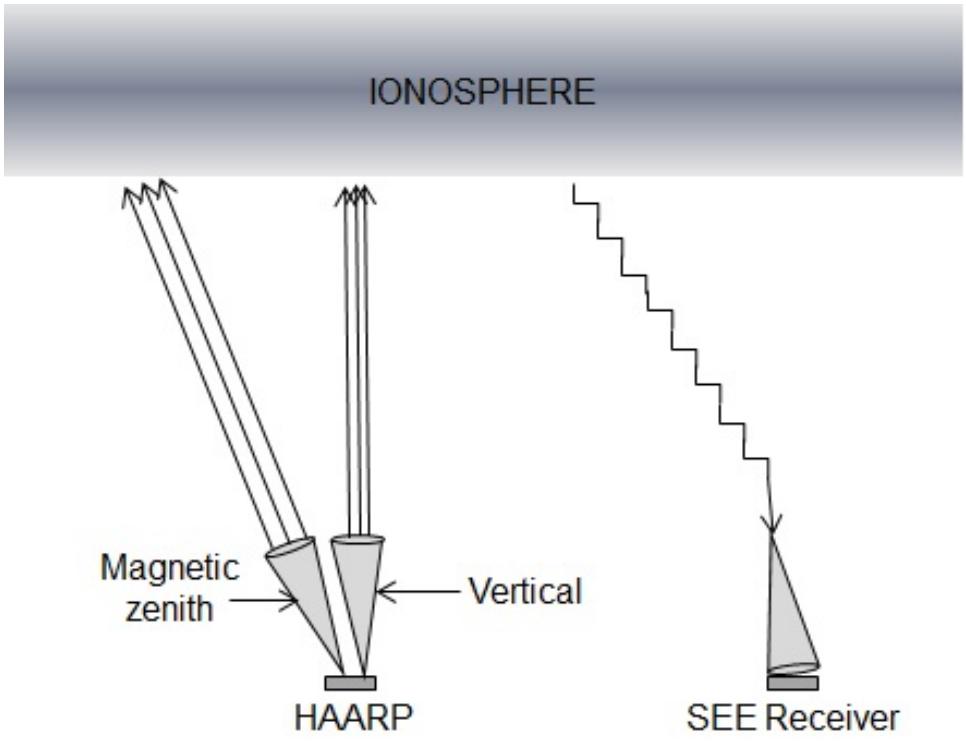

Figure 2.8: Model for generation of SEE

The classification of SEE spectral features and the description of their generation through parametric decay instability processes was provided by Stubbe et al., 1984. The SEE spectral sidebands were found to depend on a number of ionospheric parameters in addition to the pump wave. It was also postulated that the sidebands in the SEE spectrum should develop in the altitude region where ω_0 is near the plasma upper hybrid frequency $\omega_u h$. It was also found that this spectrum is dependent on the proximity of ω_0 to the harmonics of the electron cyclotron frequency Ω_e, and proximity to upper hybrid frequency. The sidebands also depend on the amount of proximity to these frequencies. The interaction of these different waves produces SEE of important spectral features, sidebands which extend above and below the pump frequency by multiples of the lower hybrid frequency or less than a lower hybrid frequency such as the downshifted maximum (DM), downshifted peak (DP), upshifted maximum, broad upshifted maximum (BUM), etc. Figure 2.9 shows an example of some of these spectral features observed in SEE during heating experiments conducted in the 2011 HAARP campaign.

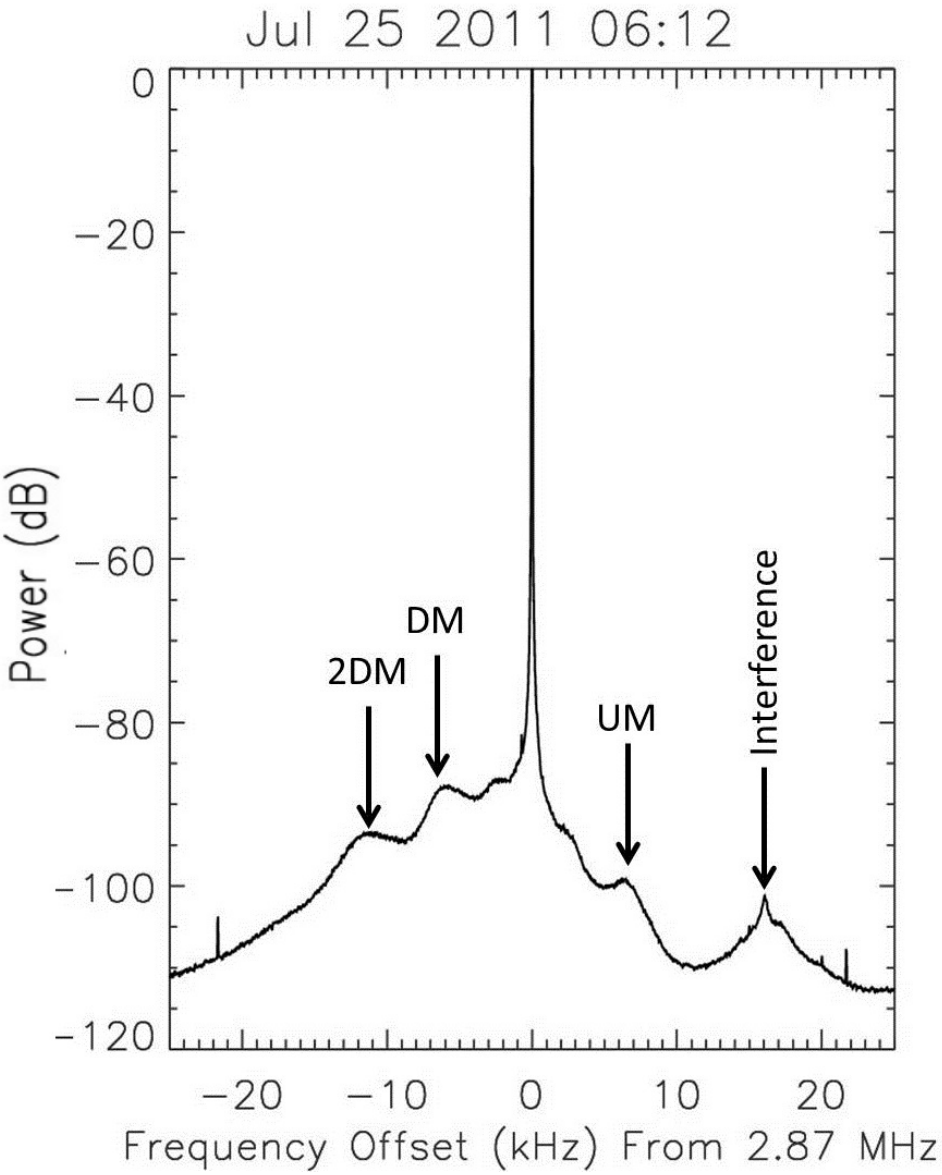

Figure 2.9: SEE spectrogram cross-section showing DM, 2DM and UM observed during second gyro-harmonic heating experiment

There has been a considerable interest recently in the generation of an artificial ionospheric layer when the transmitter is tuned to harmonics of the electron gyro-frequency f_{ce} [e.g., Mishin et al., 2011; Pederson et al., 2011]. Another phenomenon in SEE with structures near the ion-gyro frequency seen in its spectrum is generating substantial curiosity. O+ gyro-harmonic structuring has been observed for second electron gyro-harmonic heating within 1kHz of the pump frequency generated by the so-called Stimulated Ion Bernstein Scatter (SIBS) [Bernhardt et al., 2011]. A theory based on the interaction at the reflection altitude

was originally proposed by Bernhardt et al., 2011 that suggested the parametric decay of O-mode EM pump wave into electron Bernstein EB and ion Bernstein IB modes. In subsequent observations and work [Samimi et al., 2012 and 2013] broadband decay lines with embedded O^+ gyro-structures was observed. A new theory developed by Samimi et al. 2012 and 2013, based on the interaction at the upper hybrid (UH) altitude, where the pump frequency equals the local UH frequency, and double resonance condition is satisfied explained both the parametric decay of UH/EB wave into another UH/EB wave and ion waves such as ion gyro-structures and oblique IA decay believed to be responsible for the broadband spectral feature. This theory was developed in a single-component plasma.

During the HAARP campaign in 2011, stimulated radiation experiments were designed to frequency step near $2f_{ce}$ at two different beam angles. The stimulated electromagnetic emissions generated during this campaign shows harmonics of a newly discovered emissions line related to H^+ cyclotron frequency. These new emission lines are ion electrostatic waves in the ion-ion hybrid frequency range. Analysis of these emission lines in terms of their generation process and theoretical explanation is provided in this research work.

2.4 Scientific Contribution from This Work

In this research, two active experiments are under consideration: an aerosol release experiment conducted to understand a naturally occurring phenomena of natural dust layer; and stimulated electromagnetic emissions to investigate the plasma processes in the ionosphere.

This study's scientific contributions are as listed below:

Aerosol release experiment: Extended past work by developing a model to investigate the creation and evolution of the artificial dust layer and associated lower hybrid turbulence generated by two different mechanisms at different time scales.

- Investigate creation and evolution of irregularities generated by dust injection at oblique angles to background magnetic field for the first time.
- Simulation involved more realistic boundary conditions where neutral dust was injected in background plasma, drifted across the simulation domain and was taken out from the opposite boundary to allow only neutralized dust particles to be injected from the source throughout the simulation time.
- For the first time, a model compares lower hybrid turbulence generated by dust charging and dust streaming at two different time scales due to the boundary layer inhomogeneity and the free streaming.
- Incorporated new physics of ion-wave particle damping, dust-neutral collisions, and effects of ion-neutral collisions.

Chapter 3 covers material on my contribution to the aerosol release experiment. A brief motivation and introduction is also given to the model developed. A linear theory of the lower hybrid turbulence is analyzed and the results are presented, while the hybrid simulation model is explained in terms of all the governing equations. The simulation runs were completed within the parameter regime of the CARE project. The results of the model showing a non-linear evolution of the turbulence are discussed and a comparison is made with the linear theory. Two generation mechanisms are investigated for two different time scales. Each turbulence is compared in terms of its generation, controlling dynamics, saturation mechanism, wave electric field, and spatial structures. Finally, conclusions are drawn predicting the dust cloud evolution, and lower hybrid turbulence generation.

HF stimulated radiation experiment: Analyzed cause and generation process of newly observed emission lines in the stimulated electromagnetic emission spectra.

- Reported, for the first time, new observations related to protons in stimulated electromagnetic emission spectrogram.
- Summarized all observations with its time evolution and comparisons.
- Postulated reason for the emissions lines by investigating other instrumental data during the experiment period. Inferred proton precipitation to be the plausible cause.
- Further developed a new parametric decay instability in multi-ion component plasma with several dominating species and H^+ minority species to explain the generation process of the new emission lines.

Chapter 4 covers all my contributions to this experiment. The focus is on the first observations of structuring near the H+ (proton) gyro-frequency in the SEE spectrum, during second electron gyro-harmonic heating. A brief description of work completed in this field pertaining to these new emission lines is given and discussed in detail. Active ionospheric conditions are discussed based on data available from a magnetogram and riometer. A novel theory is developed to explain these emissions based on Parametric Decay Instability (PDI) in a multi-ion component plasma due to possible proton precipitation associated with the disturbed conditions during the heating experiment. The implications of this study include new possibilities for characterizing proton precipitation events during ionospheric heating experiments.

Chapter 3

Irregularities Generated during Active Aerosol Release Space Experiments

In this chapter, we investigate lower hybrid turbulence generated during a dust layer injection at an altitude of 250 km in the ionosphere by using a simulation model developed with many novelties. The model is validated with linear theory. To predict the generation of turbulence during the artificial aerosol release, CARE, this model is studied in the parameter regime of the experiment. The next section provides the introduction with motivation and also the organization of the rest of the chapter.

3.1 Introduction

A natural dust layer formed by tons of meteoric dust spans the altitude range between 80 and 100 km of the earth's upper mesosphere and lower thermosphere. Noctilucent Clouds (NLCs) are composed of ice particles that nucleate on these dust particles. NLCs are a spectacular visual display and the highest clouds in the earth's atmosphere. These dust layers are charged due to a collection of electrons and ions from the earth's ionosphere. Polar Mesospheric Summer Echoes are radar echoes which result from the scattering of radar signals off the irregularities in the electron density above the NLC altitude due to the charging of turbulent dust density [Cho et. al., 1993; Cho et. al., 1997]. An alternate approach to understanding natural dust layers and the associated turbulence is to perform active near-earth space experiments in which a dust cloud is artificially created in a controlled manner in the upper atmosphere. The Charged Aerosol Release Experiment (CARE) used a chemical release from Nihka motor to inject artificial dust at about an altitude of 250 km into the earth's ionosphere to investigate a similarity in plasma irregularities associated with natural and artificial dust layers. Solid rocket motors produce dust particles composed of Al_2O_3 [Bernhardt et. al., 2009; Bernhardt et. al., 2011]. CARE utilized radar backscatter

to investigate artificial dust clouds. The comparison between the artificial and natural dust layers will aid in understanding the physical processes in the natural dust layer which is currently a forefront issue in space science. The physical processes that are expected to be important in generating plasma turbulence for radar backscatter or in situ wave observations during the early time after creation of an artificial dust cloud in the earth's ionosphere will be considered here. The objective is to investigate two possible plasma instability mechanisms that may generate such turbulence as the dust is injected across a background magnetic field into a plasma, representative of the F-region ionosphere, which is a possible configuration of the CARE experiments. The first of these instabilities is driven by the inhomogeneity at the boundary between the dust cloud and the background plasma, and the second is driven by the streaming of charged dust relative to the background plasma. Both may generate turbulence in the lower hybrid frequency range. The organization of this chapter is as follows. First, the linear theory of the instabilities will be presented. This is followed by the description of a two-dimensional plasma simulation model that will be used for examining the nonlinear evolution of the instabilities during the expansion of an artificial dust cloud across the magnetic field in the ionosphere. Results of the two instability mechanisms will be discussed and compared over a range of parameters relevant to near-earth space experiments. Conclusions will then be drawn about the plausibility of these mechanisms for generating turbulence during the experiments.

3.2 Linear Theory of Plasma Irregularities

Two mechanisms are considered for generating irregularities in the lower hybrid frequency range due to dust injection across a background magnetic field. The first mechanism is related to the inhomogeneity in the boundary layer created due to the initial expansion of the dust into the background plasma [Scales et. al., 2010; Chae et. al., 2000]. Ambipolar electric fields generate sheared $\vec{E} \times \vec{B}$ flows that develop along the boundary layer resulting in vortex-like structures [Ganguli et. al., 1998]. The timescale for initial creation of flows that generate these irregularities is of the order or faster than the charging time τ_c given by $\tau_c \approx \omega_{pi}^{-}1(\lambda_D/a)$ [Rosenberg et. al., 2011], where a is the radius of dust grain; λ_D is the Debye length; and ω_{pi} is the plasma frequency of the ion. This process does not require the dust dynamics in the electrostatic field and of course may occur on timescales much less than the dust plasma period. The dust serves primarily to reduce the electron density and form the boundary layer with the sheared ambipolar field and cross-field flow velocity. The second mechanism is due to the streaming of dust relative to the background plasma after the dust has reached a near equilibrium charge after this initial period-which is much longer than the dust charging period. The charge on the dust particles may be taken to be at the equilibrium charge (typically negative) in this case. The dynamics of the dust in the electrostatic field are of course critical for this process and occurs after many dust plasma periods. The two mechanisms just described may be expected to be interrelated, but

for simplicity in this work they will be considered independently. Ongoing work indicates important consequences of this interdependence that will be reported in the future.

The physical model consists of electrons, ions and uniform-sized dust particles. The dust may be assumed to be negatively charged due to electron attachment and drifting relative to background plasma with velocity of the order of the ion's thermal speed. The charge neutrality condition is as follows:

$$n_e + Z_d n_d = n_i \tag{3.1}$$

where n_e, n_i and n_d are the densities of electrons, ions and dust particles respectively, and Z_d is the dust charge number. The dispersion relation for both instabilities is given as

$$1 + \chi_e + \chi_i + \chi_d = 0 \tag{3.2}$$

where χ_e,χ_i and χ_d is the susceptibility of electrons, ions and dust respectively.

For the shear-driven instability, the susceptibilities are approximated as [Scales et. al., 2010]

$$\chi_e \simeq \frac{-\omega_{pi}^2}{(\Omega_{ci}(\omega - k_y V_E)k_y L_N)}; \chi_i \simeq \frac{-\omega_{pi}^2}{\Omega_{ci}^2}; \chi_d \simeq 0 \tag{3.3}$$

where ω and k_y are the wave frequency and the wavenumber along the boundary, V_E is electron $\vec{E}$ x $\vec{B}$ drift flow velocity along the boundary and $L_N = (dn_{e0}/dx)/n_{e0}$ is the electron density gradient scale length. Also $\omega_{\rm pi}$ and $\Omega_{\rm ci}$ are the ion plasma and cyclotron frequency. The dust motion dynamics is neglected since the timescale for growth is much less than the dust plasma period and the dust susceptibility may be neglected. Using these susceptibilities the dispersion equation is given by

$$\begin{aligned} \tilde{\omega}^4 \quad &+ \quad (\frac{\delta_i}{\tilde{k_y}} S - \frac{\alpha_i}{\delta_i}\tilde{k}_y)\tilde{\omega}^3 \\ &- \quad \tilde{\omega}^2 + (\frac{\alpha_i}{\delta_i}\tilde{k_y})\tilde{\omega} = 0. \end{aligned} \tag{3.4}$$

where $\tilde{\omega} = \omega/\omega_{lh}$; $\tilde{k_y} = k_y L_E$; $\delta_i = \omega_{pi}/\Omega_{ci}$; $S = L_E/L_N$; $\alpha_i = V_E/\Omega_{ci}L_E$; where $L_E = (dV_e/dx)$ electron flow velocity shear scalelength and $\omega_{\rm lh}$ is the lower hybrid frequency.

For the dust streaming instability, the susceptibilities are approximated as [Chae et. al., 2000, Fu et. al., 2011]

$$\begin{aligned} \chi_e \simeq \frac{1}{k^2\lambda_{De}^2}\{1 + \zeta_{e0} \sum_{n=-\infty}^{\infty} \Gamma_n(b_e) Z(\zeta_{en})\} \\ \chi_i \simeq \frac{1}{k^2\lambda_{Di}^2}\{1 + \zeta_i Z(\zeta_i)\} \\ \chi_d \simeq \frac{1}{k^2\lambda_{Dd}^2}\{1 + \zeta_d Z(\zeta_d)\} \end{aligned} \tag{3.5}$$

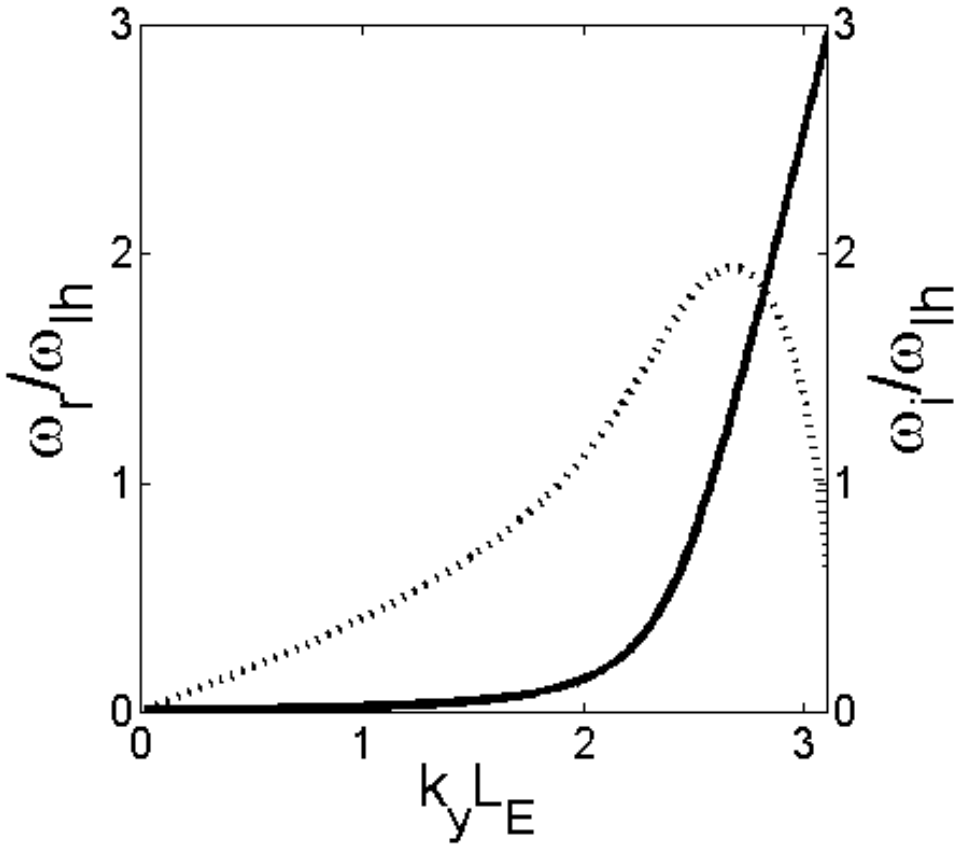

Figure 3.1: Real frequency (solid, axis on left) and growth rate (dotted, axis on right) of lower hybrid shear-driven instability

where $b_e = k_\perp^2 \rho_e^2/2$, $\Gamma_n(b_e) = I_n(b_e)\exp(-b_e)$, where I_n is the modified Bessel function of order n $\zeta_e = (\omega - n\Omega_{ce})/k_{||}v_{te}$, $\zeta_i = \omega/\sqrt{2}kv_{ti}$ and $\zeta_d = (\omega - kv_d)/\sqrt{2}kv_{td}$. Also v_{te}, v_{ti} and v_{td} is the electron, ion and dust thermal velocity respectively; v_d is drift speed of the dust particles, which is of the order of ion thermal speed in the x direction. Also $k_\perp$ and $k_{||}$ is the wavenumber perpendicular and along the magnetic field respectively and k is the magnitude of the wavenumber. The electron plasma and cyclotron frequency are given by $\omega_{\rm pe}$ and $\Omega_{\rm ce}$ and the dust plasma frequency is $\omega_{\rm pd}$ ($<< \omega_{\rm lh}$).

The real (dispersion relation) and imaginary (growth rate) frequency for both instabilities are shown in Figures 3.1 and 3.2 using parameters roughly in line with the CARE experiments while also allowing computational efficiency and comparisons with the simulation model and results to be described in the following sections. The solid lines show the real part of the frequency while the dashed lines show the imaginary part for both cases. The background plasma and dust concentrations are taken as identical for both instabilities. The background plasma is described here as $\omega_{pi}/\Omega_{ci} \approx 60$, which is roughly equal to the parameters used in the CARE experiment. The dust concentration is described with $\omega_{pd}^2/\omega_{pi}^2 = 0.005$. Note that

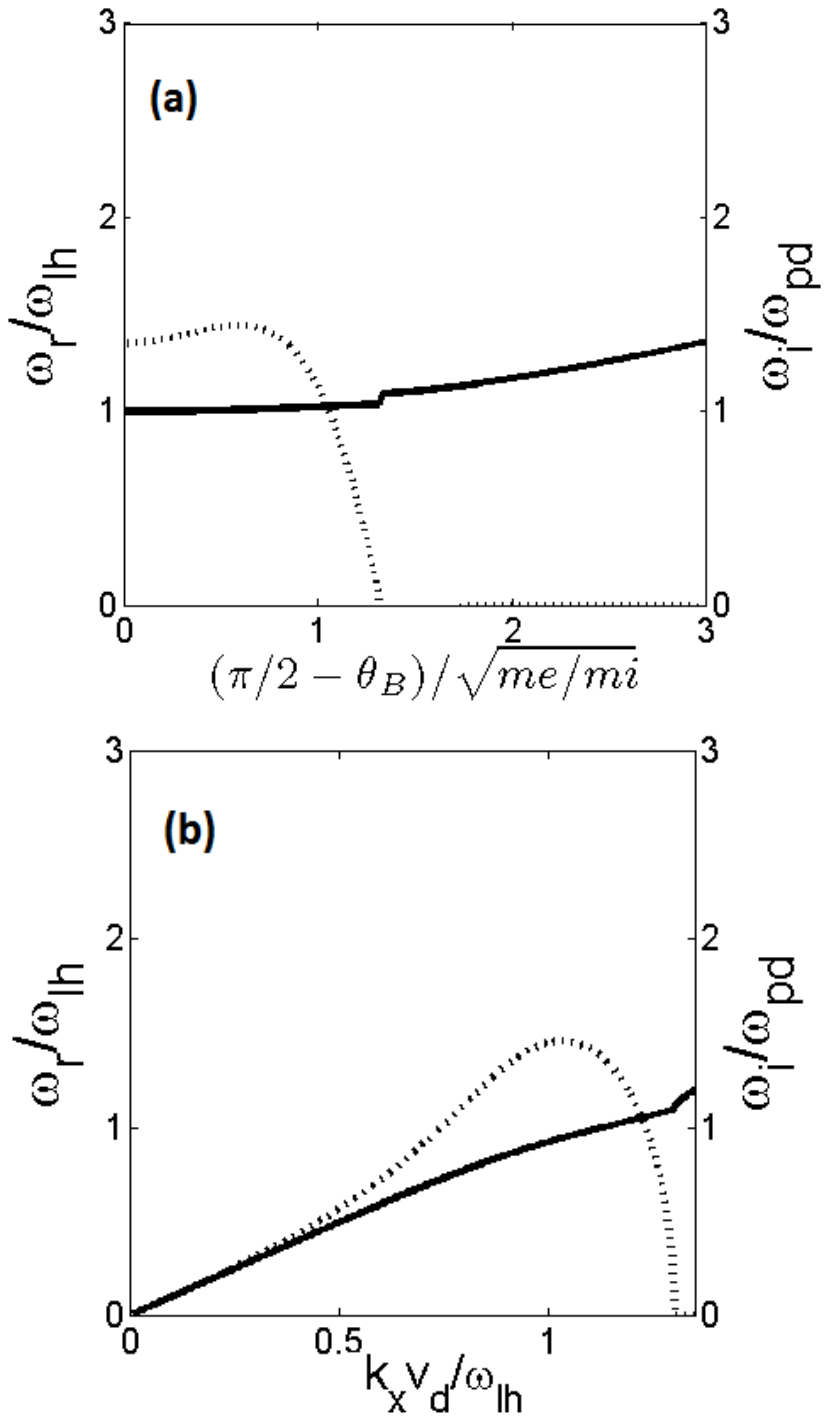

Figure 3.2: Real frequency (solid, axis on left) and growth rate (dotted, axis on right) of lower hybrid streaming instability for (a) varying angles and (b) varying wavenumber at angle of maximum growth

this corresponds to a reduced mass ratio ($m_d/m_i = 10^3$) for comparison with the numerical model of the following section. This reduced ratio is used to conserve computational time; however, it does not alter the qualitative physics under investigation [Oppenheim et. al., 1996]. Also these are a small percent of dust particles relative to the background plasma with dust radius up to 1μm or so, as will be described shortly.

The shear-driven instability (in figure 3.1) has its free energy source described in two parameters $S = 0.19$ and $\alpha_i = 356$ which depend on the density scale length L_N in the boundary layer, the $\vec{E} \times \vec{B}$ flow velocity V_E and the shear lengths of this flow in the boundary layer L_E. Note that these parameters must be estimated a priori in a simulation since the boundary layer is created due to dust charging. The developing boundary layer is estimated to be of the order of meters initially [Scales et. al., 2010]. The wavelength of shear-driven instability is such that $\lambda \approx L_E$ and therefore is determined by the initial gradients in the boundary layer. The dispersion relation and growth rate for the streaming instability is calculated versus angle off perpendicular propagation to the magnetic field ($\pi/2 - \theta_B$). The growth rate maximizes near the angle $\pi/2 - \sqrt{m_e/m_i} = 89.6°$. The growth rate at this angle is plotted versus wavenumber along the streaming direction and is limited by Landau damping at larger angles. The drift speed is taken so $v_d = 3v_{ti}$. Notice that at maximum growth rate, the wave frequency is in the range of ω_{lh} for both instabilities. The shear-driven instability, however, has a much larger growth rate of the order of the lower hybrid frequency while the streaming instability has a growth rate of the order of the dust plasma frequency. The dust streaming instability therefore occurs on a much longer timescale.

3.3 Simulation Model

There are different kinds of numerical methods used to simulate irregularity generation in space plasma. These can be classified into particle in cell (PIC), fluid code (MHD) and hybrid code, where some plasma species are treated as fluids while others are treated as a particle. Figure 3.3 shows time and space scales resolved in these simulation models. When introducing a species that is modeled as fluid, longer time scales are resolved with less noise. To resolve the lower hybrid plasma irregularities generated during the injection of artificial dust particles during CARE, the project's hybrid code is used for modeling. The simulation model is a 2-D plane ($x - y$) with inclined background magnetic field $\vec{B}$ in ($x - z$) plane as shown in Figure 3.2. The angle of the magnetic field relative to the simulation plane is denoted by θ_B. The electrons and ions are described with fluid equations and the dust is modeled with simulation particles using the Particle-In-Cell (PIC) method. For simplicity the collisions of electrons and ionospheric neutrals are neglected which is reasonable at the altitudes under consideration and timescales of interest [Scales et. al., 2010; Fu et. al., 2011]. Ion collisions with neutrals in the plume are considered to investigate effects on the shear-driven instability. This is described in Section 3.4.

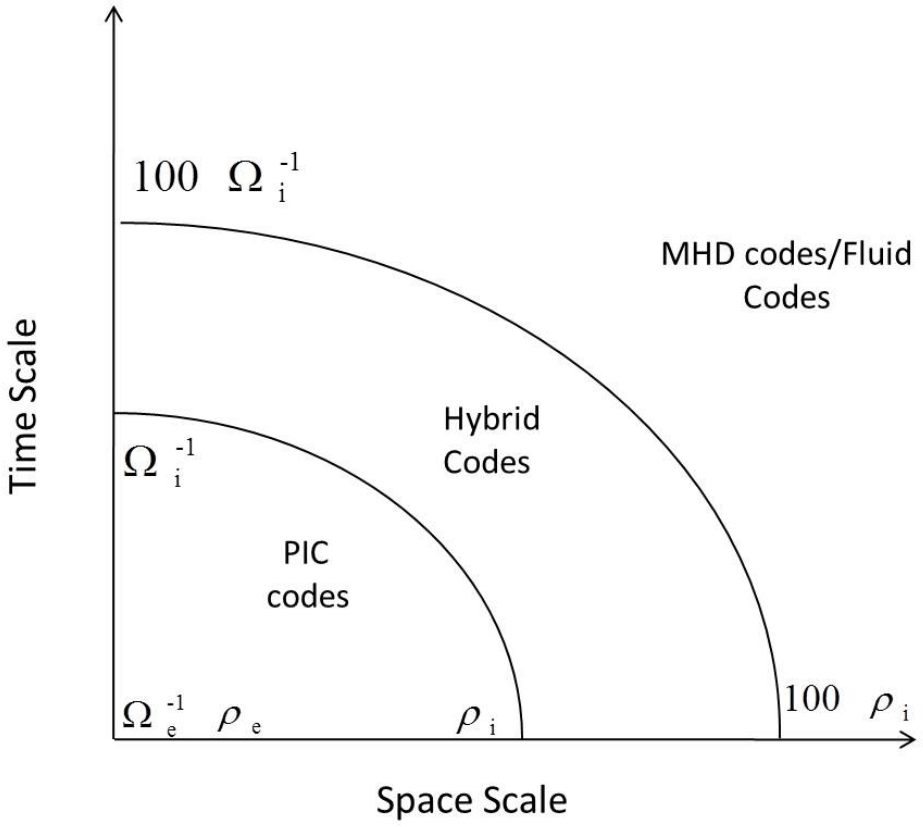

Figure 3.3: Time and space scales resolution of different simulation models

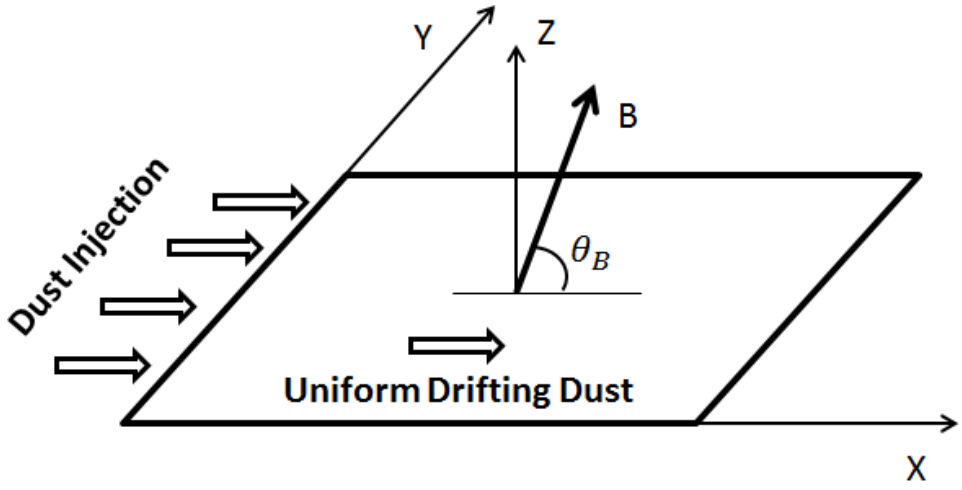

Figure 3.4: Configuration of the two-dimensional simulation model for injection of initially neutral dust or streaming of uniform charged dust into a background plasma in the x direction. The simulation plane is at angle θ_B to the background magnetic field B.

The electron density n_e evolution is modeled with the continuity equation

$$\frac{\partial n_e}{\partial t} + \nabla \cdot (n_e \vec{v_e}) = \frac{dn_e}{dt}|_{\text{charging}} + P_e + L_e \tag{3.6}$$

where $\vec{v_e}$ is the electron velocity; $dn_e/dt|_{\text{charging}}$ is the change in electron density due to collection of electrons on the dust due to its charging; P_e and L_e are the production and loss of electrons due to photoionization and recombination in the ionosphere. The component of velocity perpendicular to the magnetic field $\vec{v}_{e\perp}$ is approximated by the perpendicular momentum equation

$$\vec{v}_{e\perp} = \frac{\vec{E} \times \vec{B}}{B^2} \tag{3.7}$$

The component of electron velocity parallel to the magnetic field $v_{e\parallel}$ is approximated by the parallel momentum equation

$$\begin{aligned} \frac{\partial v_{e\parallel}}{\partial t} + (\vec{v_e}.\nabla) v_{e\parallel} = & -\frac{q_e \cos\theta_B}{m_e} \frac{\partial \phi}{\partial x} \\ & -\frac{K T_e \cos\theta_B}{m_e} \frac{1}{n_e} \frac{\partial n_e}{\partial x} \end{aligned} \tag{3.8}$$

where q_e is the electron charge, m_e is the electron mass, T_e is the electron temperature, K is Boltzmann's constant, and ϕ is the electrostatic potential which is related to the electrostatic electric field by $\vec{E} = -\nabla\phi$. The ions are also treated as a fluid whose density n_i is self-consistently reduced due to dust charging.

$$\frac{\partial n_i}{\partial t} + \nabla \cdot (n_i \vec{v_i}) = \frac{dn_i}{dt}|_{\text{charging}} + P_i + L_i. \tag{3.9}$$

The ions are approximated as unmagnetized and the momentum equation for ion velocity $\vec{v_i}$ is

$$\begin{aligned} \frac{\partial \vec{v_i}}{\partial t} + (\vec{v_i} \cdot \nabla)\vec{v_i} = & \frac{q_i}{m_i}\vec{E} - \gamma \frac{K T_i}{m_i} \frac{1}{n_i} \nabla n_i \\ & + {\nu_L}^* \vec{v_i} - \nu_{in}(\vec{v_i} - v_d) \end{aligned} \tag{3.10}$$

where q_i, m_i, and T_i are the ion charge, mass, and temperature, ν_{in} is the ion-neutral collision frequency and ${\nu_L}^*$ is a term for modeling ion landau damping which is written in wavenumber space as ${\nu_L}^* = -(\omega_{pi}^2/kV_{ti})(\sqrt{\pi}/k^2\lambda_{Di}^2)\exp(-\omega_{pi}^2/k^2V_{ti}^2)$ e.g. [Oppenheim et. al., 1996] and $\gamma = (2 + D/D)$ is the ratio of specific heats. D is the number of dimensions.

The standard Particle-In-Cell method is used to model the dynamics of the dust particles. The jth dust particle is assumed to have the mass m_j and a time variable charge $Q(t)$. The velocity and position of dust particles is determined by

$$\frac{d\overrightarrow{v}_j}{dt} = \frac{Q_j(t)}{m_j}\overrightarrow{E}; \frac{d\overrightarrow{x}_j}{dt} = \overrightarrow{v}_j \tag{3.11}$$

The dust-neutral collisions are implemented using a Monte Carlo collision model [Vahedi et. al., 1995]. The probability of their collision is determined by $P = 1 - exp(-\nu_c \bigtriangledown t)$, random angles that describe the new velocity vector are calculated. The magnitude of the velocity is conserved. The new velocity vectors in terms of the random angles is given by,

$$\hat{v}_{scat} = \hat{v}_{inc}\cos\psi + \hat{v}_{inc} \times i\frac{\sin\psi\sin\phi}{\sin\theta} + \hat{v}_{inc} \times (i \times \hat{v}_{inc})\frac{\sin\psi\cos\phi}{\sin\theta} \tag{3.12}$$

The time dependent charge on the dust is described with the Orbit Motion Limited (OML) approach [Shukla et. al., 2002]

$$\frac{dQ_j}{dt} = I_{ej} + I_{ij} \tag{3.13}$$

where I_{ej} and I_{ij} are the electron and ion currents collected by the dust grain. Assuming negatively charged dust, the electron and ion currents on the jth dust grain are given by

$$I_{ej} = \sqrt{8\pi}r_d^2 q_e n_e v_{te} \exp\left[\frac{e\phi_{fj}}{KT_e}\right] \tag{3.14}$$

$$I_{ij} = \sqrt{8\pi}r_d^2 q_i n_i v_{ti} \left[1 - \frac{e\phi_{fj}}{KT_i}\right] \tag{3.15}$$

where r_d is the grain radius and ϕ_{fj} the floating potential on the dust grain given by $\phi_{fj} = Q_j(t)/C = Q_j(t)/4\pi\epsilon_0 r_d$ where C is the grain capacitance and ϵ_0 is the vacuum permittivity. To calculate the electrostatic potential, the Poisson's equation is used and given by

$$\epsilon_0\nabla^2\phi = -(q_e n_e + q_i n_i + Q_d n_d) \tag{3.16}$$

here, $Q_d n_d$ denotes the dust charge density which is calculated with the PIC method. The algorithm for solving this model numerically has been previously discussed [Chae et. al., 2000].

Two types of particle boundary conditions are used to investigate the two instabilities. For the shear-driven instability, neutral particles are continuously injected from the left side of the simulation domain as shown in Figure 3.4. As they enter the domain, they charge due to the background plasma currents. As dust particles reach the right side of the simulation domain, they are removed from the system. For the streaming instability, the dust particles are taken to have a fixed charge and have a uniform density across the simulation domain. The dust particles then drift at a uniform rate through the background plasma with periodic particle boundary conditions.

3.4 Results

In the CARE project, the artificial dust layer is created in the earth's ionosphere at an altitude of approximately 250 km. The background plasma may therefore be characterized for purposes here with density of approximately 5×10^{11} m^{-3}. The primary ion component at this altitude is O^+. The electron and ion temperatures are taken to be equal and 0.1 eV, which implies an ion thermal velocity of order 1 km/s. The dust particles are injected by using rocket motor burns and the size of dust particles injected are estimated to be from 0.5μm - 1 μm. The dust injection speed is about two to three times the ion thermal speed $v_{\rm ti}$. The dust mass concentration is described with $\omega_{\rm pd}^2/\omega_{\rm pi}^2 = 0.0005$ which typically corresponds to a few percent of dust particles relative to the background plasma. The dust mass used here is artificial for simulation purposes. The impact of varying the dust particle size, density and velocity has been considered on the shear-driven instability for injection perpendicular to the background magnetic field in a prior investigation [Scales et. al., 2010]. The objective of this investigation is to ultimately consider the generation of turbulence in the lower hybrid frequency range over longer timescales by considering two kinds of plausible instability mechanisms that occur on different timescales. Also, the impact of injection at an oblique angle to the magnetic field, which is more realistic, will be considered as well.

During the initial injection of neutral dust, the dust charges and creates a reduction in background electron density on the dust charging timescale. Therefore, a boundary layer is created between the dusty plasma and the background plasma. The inhomogeneous flow along the boundary layer provides free energy for a shear-driven turbulence [Scales et. al., 2010]. On somewhat longer timescales the streaming of charged dust particles relative to the background plasma provides free energy for a streaming lower hybrid instability. The dispersion equation for both of these instabilities was described in Section 3.2. Since the shear-driven instability is expected to occur first after the initial injection, it will be considered first with the model of Section 3.3.

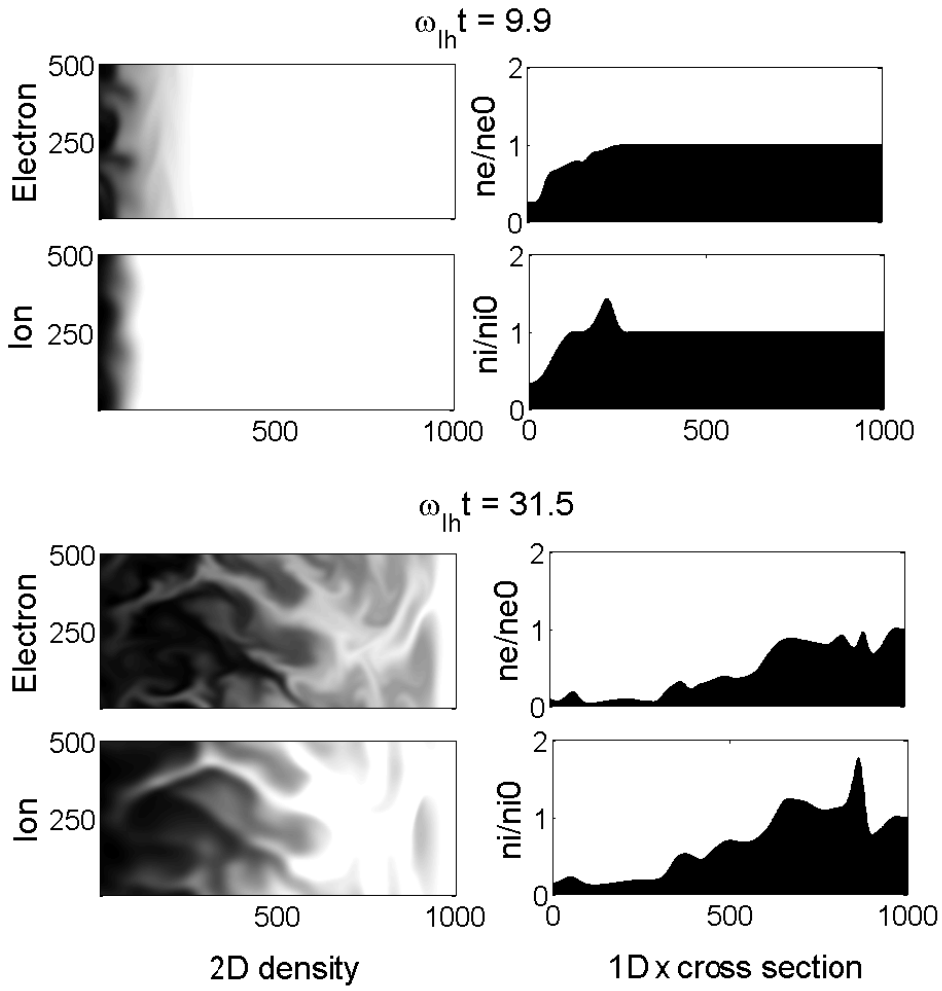

Figure 3.5: Temporal evolution of electron and ion density for magnetic field inclination of 90° to simulation plane. Initially uncharged dust is injected from left. Left column shows two-dimensional density and the right column shows the one dimensional cross-section along x direction. The shear-driven instability is seen growing with the development of the vortex-like structures.

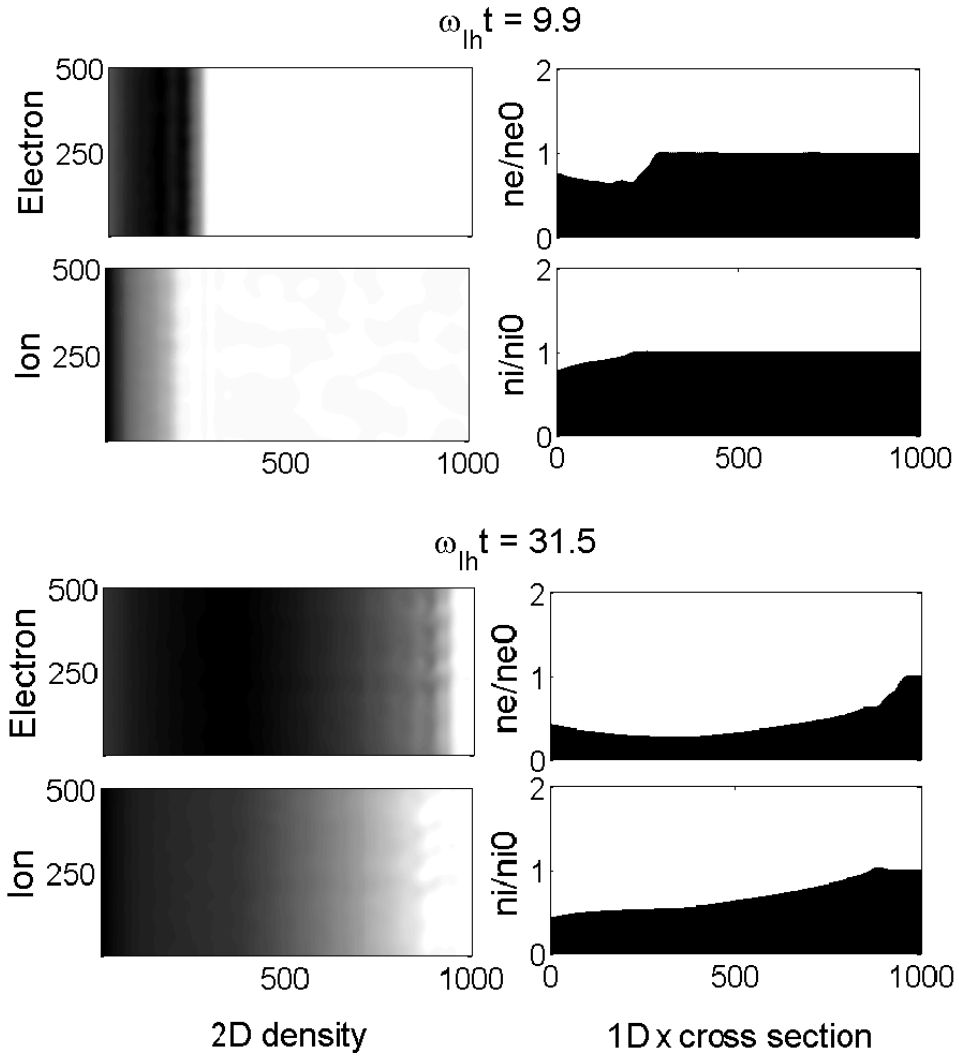

Figure 3.6: Temporal evolution of electron and ion density for magnetic field inclination of 75° to simulation plane. Initially uncharged dust is injected from left. Left column shows the two dimensional density and the right column shows the one dimensional cross-section along x direction. The shear-driven instability is much weaker compared to the perpendicular inclination case.

Figures 3.5 and 3.6 show the temporal evolution of the background plasma electron and ion density for $\theta_B = 90°$ and $\theta_B = 75°$ respectively for the shear-driven instability. For now the impact of collisions with injected neutral gas in the plume is neglected. This will be described shortly. The dust density is not shown since no fluctuations develop in the dust density on the timescales of these simulations, which are much less than the dust plasma period. The two times shown are $\omega_{lh}t = 9.9$ (top) which is very early after the initial reduction in electron density due to dust charging, and $\omega_{lh}t = 31.5$ (bottom) after the dust has moved to the edge

of the simulation domain. The left column shows the two dimensional density of electrons n_e and ions n_i and the right column shows a one dimensional cross-section along $\hat{x}$ direction of electrons n_e/n_{e0} and ions n_i/n_{i0} where $n_{e0} = n_{i0}$ are the initial electron and ion densities. The injected dust density is a small fraction about 0.5% of the background plasma density. The dust radius is 0.5 μm which corresponds to an equilibrium negative charge of $Z_d = 125$ electrons. Therefore, at equilibrium charge the ratio of the dust charge to background plasma density is $Z_d n_d/n_{e0} = 0.625$. The dust injection speed is three times the ion thermal speed v_{ti}. The dimension of the simulation domain is $1000\lambda_D$ in x and $500\lambda_D$ in y where λ_D is the Debye length. This corresponds to the physical dimensions for the parameters under investigation of approximately 4 meters by 2 meters in x and y respectively.

As the neutral dust is injected into the background plasma, it charges negatively causing an electron density reduction as can be clearly seen in the cross-section at $\omega_{\rm lh}t = 9.9$. An ambipolar electric field develops in the $\hat{x}$ direction. The enhancement in the ion density seen in the cross-section at $\omega_{\rm lh}t = 9.9$ is due to the electrostatic snowplow effect. An electron $\vec{E}$ x $\vec{B}$ drift develops in the $-\hat{y}$ direction due to the ambipolar field. This sheared electron flow ultimately gives rise to irregularities in the electron density which can be seen to appear as vortex-like structures in Figure 3.5 at $\omega_{\rm lh}t = 9.9$. Irregularities can also be seen in ion density in Figure 3.5 and also in the dust charge which is not shown (although not in the dust density). The vortex-like structures are much more pronounced at time $\omega_{\rm lh}t = 31.5$

The inclination of magnetic field with respect to the background plasma is 75° in Figure 3.6. The change in magnetic field inclination allows the electrons to move along the magnetic field and therefore have a component of velocity in $\hat{x}$ direction. This reduces the ambipolar field and the effect of $\vec{E}$ x $\vec{B}$ drift, and thus weakening the instability in turn. The temporal evolution of electron, ion and dust charge density shows the instability still appears by the end of the simulation; however, it is quite weak. Weak vortex-structures are observed in the boundary at $x/\lambda_D \sim 900$ at time $\omega_{\rm lh}t = 31.5$ in Figure 3.6.

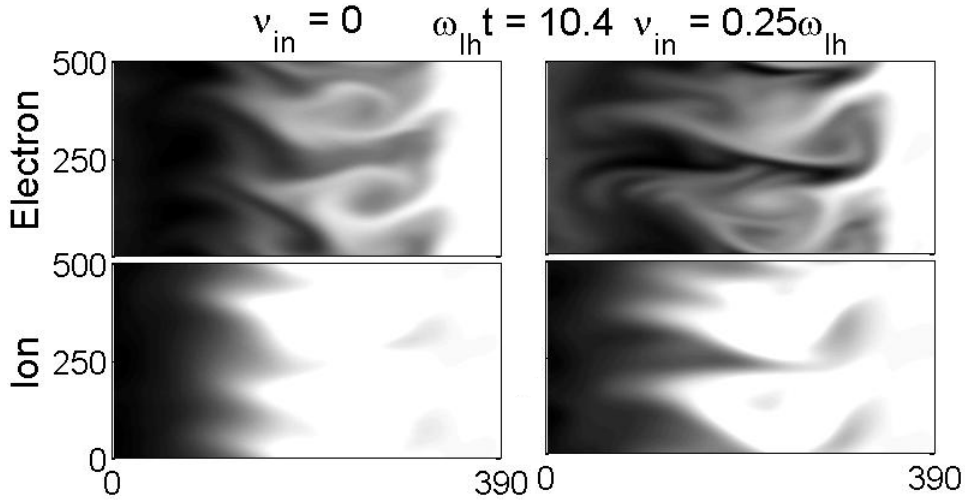

Figure 3.7: Two dimensional electron and ion density spatial structures at $\omega_{lh}t = 10.4$. Left column shows results for $\nu_{in} = 0$ and the right column shows results for $\nu_{in} = 0.25\omega_{lh}$. Note distinct vortex formation is inhibited due to plume neutral collisions.

Ion collisions with plume neutrals are considered to investigate its effects on the shear-driven instability, which may be important at early times. These neutrals are ejected with the exhaust and taken to move with a velocity of $3v_{ti}$ as do the dust particles. For the parameters of the CARE experiment, the collision frequency to lower hybrid frequency ratio is considered to be in the regime $\nu_{in}/\omega_{lh} < 1$ [Rosenberg et. al., 2011]. Several simulations were performed to investigate these effects. There is a slight reduction in the ambipolar electric field amplitude which results in a reduction of about 30% in the saturated wave field energy for $\nu_{in}/\omega_{lh} = 0.25$, which is the case seen in Figure 3.7. In general, the spatial structures show much less pronounced vortex formation when plume neutral collisions are incorporated; however, the growth and saturation amplitude are not substantially reduced for $\nu_{in}/\omega_{lh} < 0.5$.

The shear-driven process just described is expected to occur initially after injection of dust into the plasma across the magnetic field on timescales of the dust charging and creation of the electron density reductions. This timescale is much less than the dust plasma period. The streaming instability for parameter regimes considered here occurs on timescales longer than the dust plasma period as shown in Section 3.2. In this case the model of section 3.3 is initialized with charged dust particles of uniform density in the simulation domain. The background plasma, dust particle size, dust drift velocity, and dust charge density (at equilibrium) are identical to the case used to investigate the shear-driven instability just described to allow some comparisons to be discussed shortly. Note, however, that the simulation domain used in this case is twice as long in x ($2000\lambda_D$) compared to the case for the shear-driven instability. This corresponds to physical dimensions for the parameters under investigation of approximately 8 meters by 2 meters in $\hat{x}$ and y respectively. Figure

3.8 shows two-dimensional electron and ion densities on the left and one-dimensional cross-sections in the x direction in a similar format to Figures 3.5 and 3.6 for the dust streaming instability. The magnetic field inclination here is taken to be $\theta_B = \pi/2 - \sqrt{m_e/m_i} = 89.6°$. While the shear-driven waves initially begin to propagate in the $-\hat{y}$ direction in Figures 3.5 and 3.6, it is seen in Figure 3.8 as expected in the streaming instability, that the waves begin to propagate in the x direction as can be seen by the nearly plane wavefront structures at time $\omega_{pd}t = 1.8$ in the two-dimensional densities. The structures are quite turbulent by the end of the simulation at time $\omega_{pd}t = 3.8$. Careful observation of the wavefronts at $\omega_{pd}t = 1.8$ show initial development of vortex-like structures which may indicate some impact of the shear-driven waves as a secondary process in this case as the wave amplitudes grow.

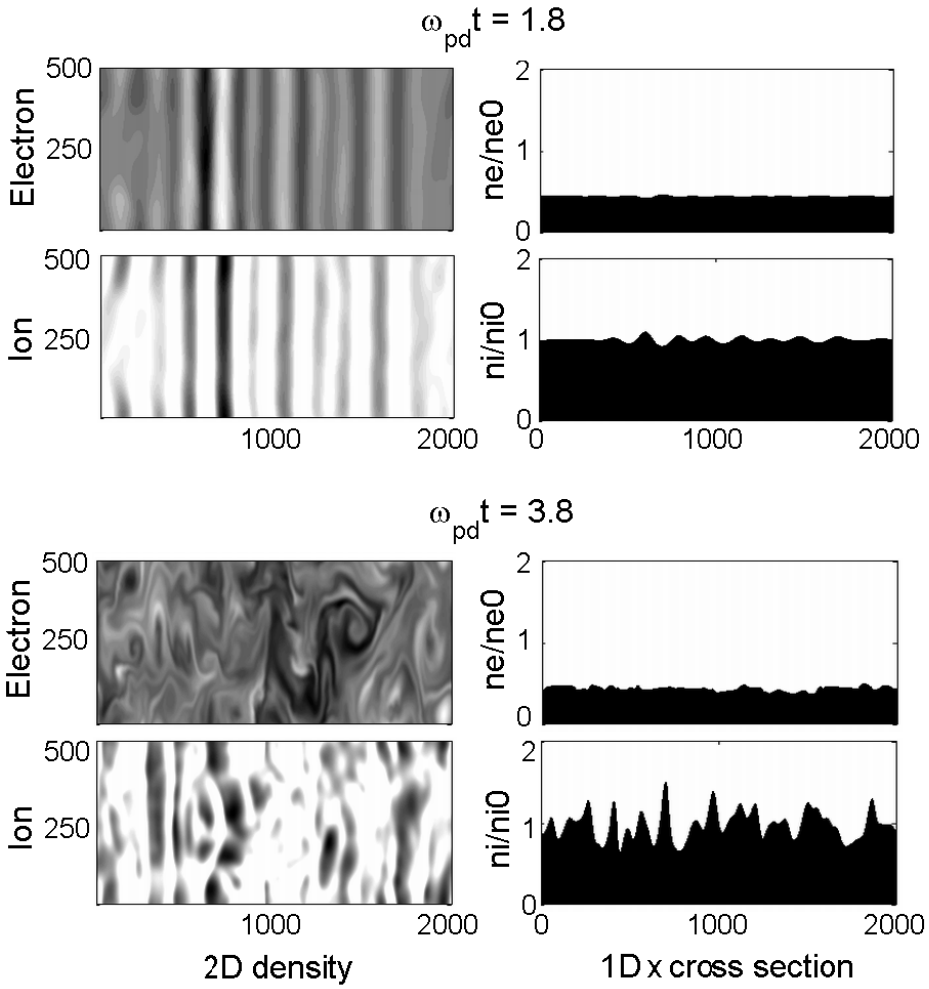

Figure 3.8: Temporal evolution of electron and ion density for $\pi/2 - \sqrt{m_e/m_i} = 89.6°$ magnetic field inclination for streaming instability. Charged dust streams uniformly from left to right. The left column is the two dimensional density and the right column is a cross-section in the x direction. The growth of the instability can be seen with the initial propagation of wavefronts to the right.

It is instructive to compare some of the important characteristics of the two instability processes which may have consequences for experimental observations. The previous simulations have utilized the same background plasma conditions and dust characteristics.

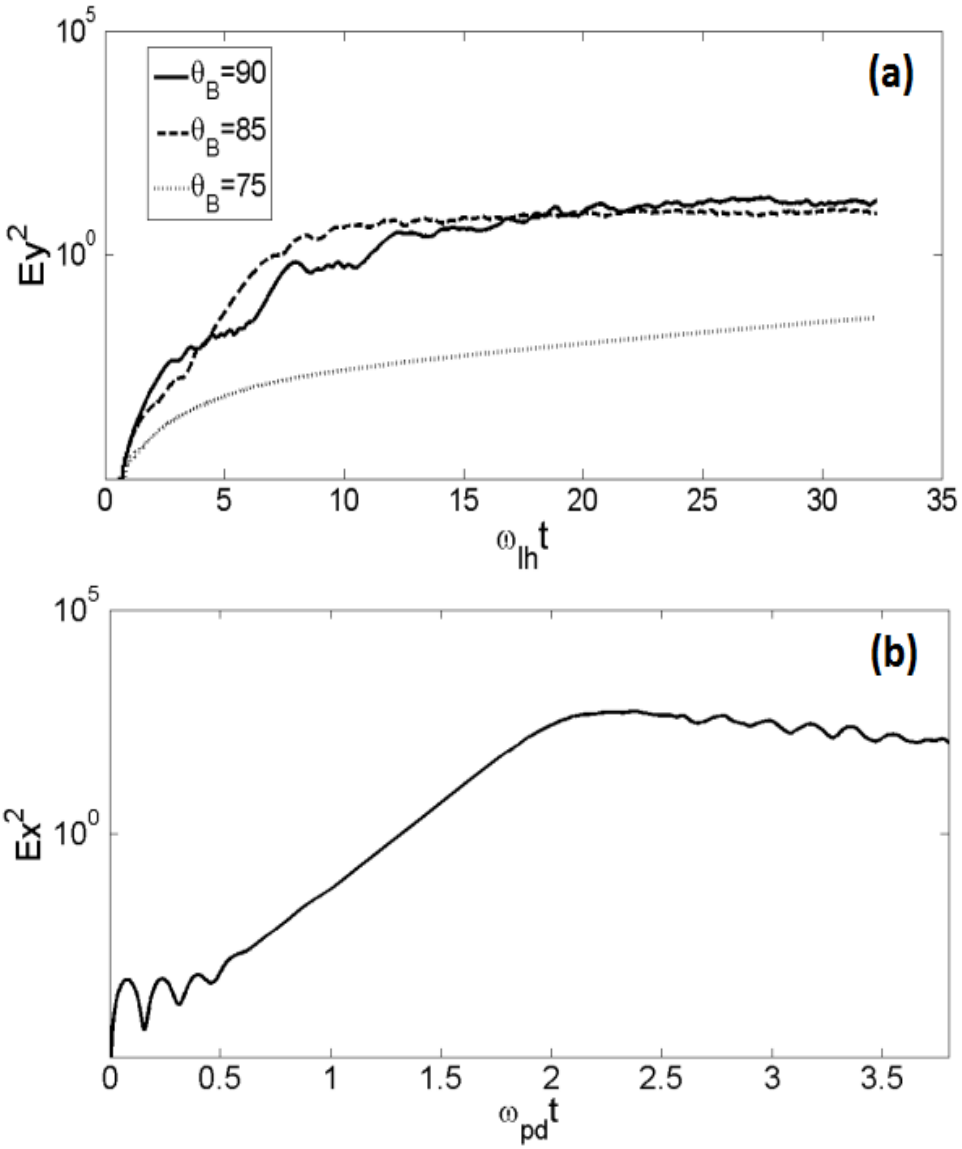

Figure 3.9: Electric field energy variation with time in terms of primary wave field (a) for shear (Ey field) and (b) streaming (Ex field) instability.

One important characteristic is the energy in the electrostatic field, which may provide some sense of the relative strength of the two processes. Figure 3.9 shows the electric field energy variation for both the instabilities in nondimensional simulation units. The field energy is shown only for the primary wave field which is $\sim \int E_y^2 dv$ for the shear-driven instability and $\sim \int E_x^2 dv$ for the streaming instability. For both the instabilities the growth rate is comparable to the linear theory. For the shear-driven instability $\gamma_{simulation}/\omega_{lh} \simeq 1$ and for the streaming instability $\gamma_{simulation}/\omega_{pd} \simeq 1.5$. The variation with the injection relative to the magnetic field is also considered. Figure 3.4 shows that the shear-driven instability

grows and saturates on lower hybrid timescales. Three cases of magnetic field inclination are shown with $\theta_B = 90°, 85°,$ and $75°$. It is observed that the strength of the shear-driven instability reduces with decreasing θ_B as described earlier, since the ambipolar field in the boundary layer and $E \times B$ flow are reduced. The streaming instability, shown in Figure 3.4, develops on a much longer timescale. The instability is strongest for angles slightly off perpendicular $\pi/2 - \sqrt{m_e/m_i} = 89.6°$. Important to note in Figure 3.9 is that the strength of wave electric field of the shear-driven case is much less than that of the streaming case. It should be noted that the shear-driven instability is concentrated only at the boundary layer between the dust and background plasmas where steep gradients drive the instability, while for streaming instability the total electric field energy exists over the entire simulation domain. In case of shear-driven instability the broadening of the boundary layer due to growth of the waves as can be seen in Figure 3.5 is the mechanism for saturating growth of this instability. However, the dust heating is expected to play a primary role in saturating the streaming instability growth.

Figure 3.10 shows the frequency power spectrum of the shear-driven and streaming instability at $85°$ and $\pi/2 - \sqrt{m_e/m_i} = 89.6°$ angles respectively. The power spectrum is estimated by calculating the Fast Fourier Transform FFT using the time series of the field $E(\omega)$ over the entire simulation. The frequency power spectrum is then estimated from $P(\omega) = |E(\omega)|^2$. Figure 3.10 shows both processes produce turbulence in the lower hybrid frequency range. However, it is observed that the power maximizes slightly below the lower hybrid frequency for the shear-driven case while just above the lower hybrid frequency for the streaming case. The shift in the peak of maximum power for the streaming case can be understood from the parallel wavenumber component in the dispersion relation for lower hybrid waves where the frequency is given by $\omega^2 \approx \omega_{\rm lh}^2 + \omega_{\rm pe}^2/(1 + \omega_{\rm pe}^2/\Omega_{\rm ce}^2)\cos^2\theta_B$. The frequency of the shear-driven waves are determined by the shear frequency $\omega \approx dV_E/dx \sim \omega_{\rm lh}$ as described in equation (3.4). Therefore this frequency is related to the gradient in the electron flow along the boundary which dynamically changes. As the waves grow, the boundary broadens and reduces the frequency and therefore the frequency of these waves is expected to be less than $\omega_{\rm lh}$ ultimately resulting in a broader spectrum of waves below this frequency as time evolves.

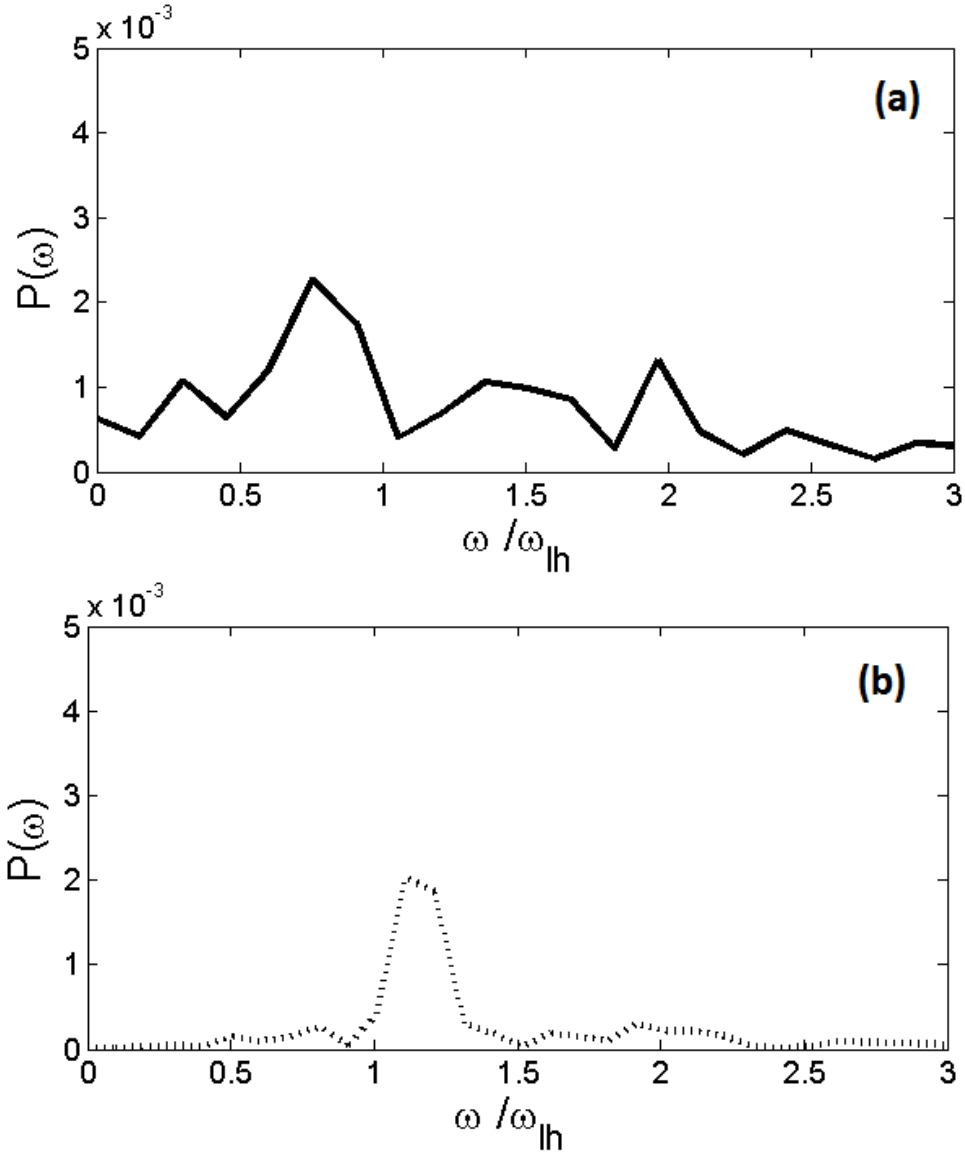

Figure 3.10: Frequency spectrum of electric field time series of (a) shear-driven instability $\theta_B = 85°$ and (b) streaming instability $\theta_B = \pi/2 - \sqrt{m_e/m_i} = 89.6°$.

It is instructive to consider the dust phase space for the streaming instability for the possibility of any particle heating during the nonlinear evolution and saturation of the instability. The velocity and position phase space plot $(v_x - x)$ in Figure 3.11 shows behavior of the injected dust beam particles at different times. The beam is taken to be cold initially with the dust drift velocity three times the ion thermal velocity as described earlier and during the linear growth period, particles oscillate with exchange of kinetic energy into field energy. During the nonlinear saturation period, particle acceleration and heating is observed. The

current model has the limitation of modeling ions as a fluid with linear Landau damping, and some ion wave-particle heating may occur as well. Ongoing work includes development of a model that includes PIC ions and this will be reported on in the near future. Preliminary comparisons indicate good qualitative agreement with the results here.

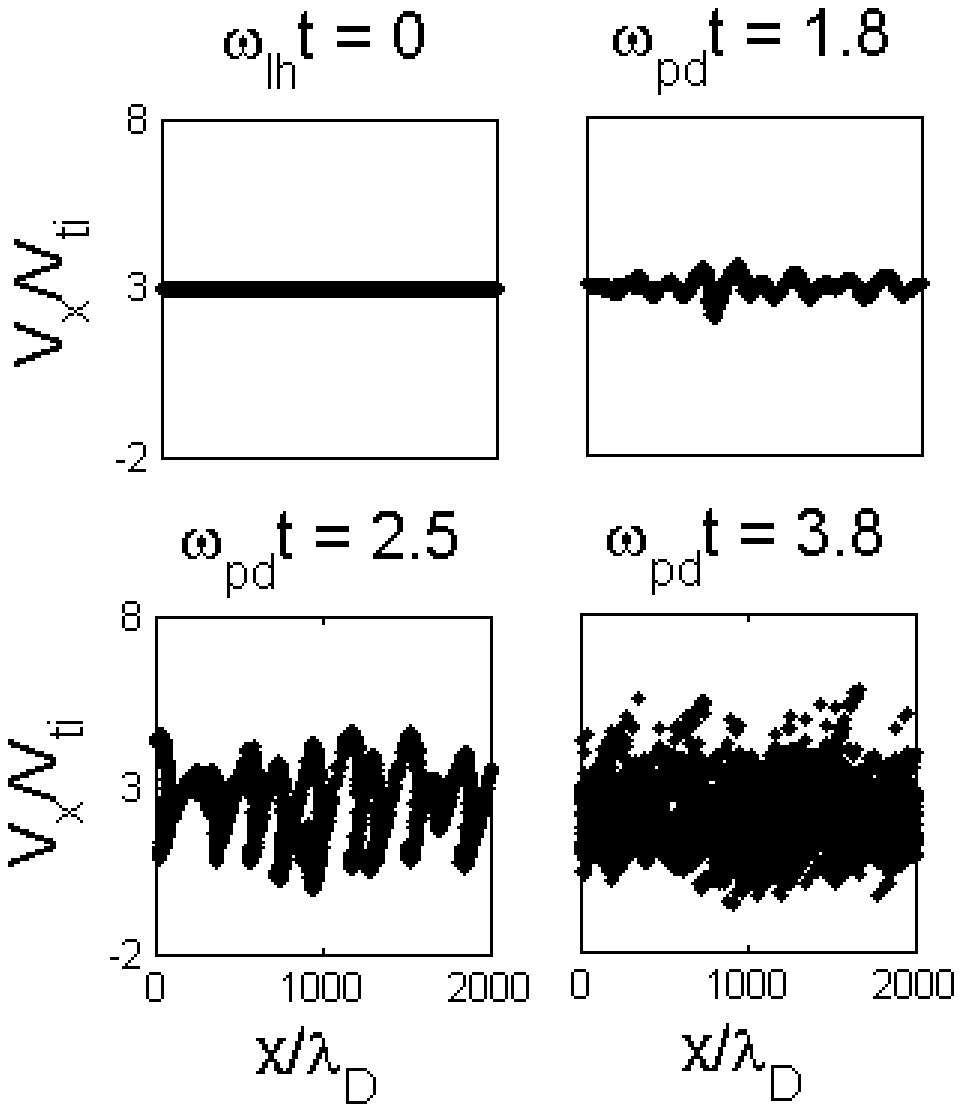

Figure 3.11: Phase space of dust particles for streaming instability. An initial cold dust beam is heated in $\hat{x}$ direction.

3.5 Summary and Conclusion

Electron irregularities generated by the creation of an artificial dusty plasma in the earth's ionosphere has been investigated. A wide range of mechanisms are expected to produce such irregularities; however, the concentration in this investigation is on irregularity production in the lower hybrid frequency range due to injection of dust at an oblique angle across the geomagnetic field. Initially, irregularities are primarily driven by inhomogeneities in the boundary layer between the expanding dust cloud and the background plasma and after several dust plasma periods, irregularities are primarily generated by dust particles streaming through the background plasma. Plasma instabilities that result from shears in the induced electron $\vec{E} \times \vec{B}$ flow in the boundary and the streaming of uniform charged dust were both investigated for parameter regimes relevant to CARE space experiments. Both instabilities were shown to be effective at generating turbulence for parameter regimes of active space experiments although they have different characteristics outside of producing turbulence in a similar frequency range. Both appear to be able to generate waves of comparable amplitudes. The shear-driven waves develop quickly after the electron reduction is created and grow on lower hybrid timescales. These waves initially propagate along the boundary of the expanding dust cloud boundary and have spatial scales of the order of the gradients in the cloud boundary. This kind of instability can exist at larger inclination angles of magnetic field as seen in Figure 7. The saturation of instability occurs primarily due to the broadening of the boundary layer between injected dust and background plasma and therefore reduction in the ambipolar electric field due to growth of the shear-driven waves. The streaming of dust produces waves that propagate, at least initially along the streaming direction and develop on timescales of the dust plasma period. Dust acceleration is observed in the saturation of this instability. Somewhat comparable electron density fluctuations are observed in both the instabilities. The irregularities were observed to be of meter scale or smaller for injection or streaming of the dust into the background plasma with velocity of order of the ion thermal speed. The processes discussed here should be observable both by ground-based and in situ space instruments. It should be emphasized that a number of other kinds of irregularities are expected to be generated during a dust cloud release in the earth's ionosphere. For instance, other possibilities include ion acoustic or dust acoustic irregularities [Fu et. al., 2011, 2012; Mahmoudian et. al., 2012]. The present investigation only considers irregularities associated with relatively high-frequency lower hybrid waves. Ongoing investigations are addressing the spectrum of possibilities.

Chapter 4

Impact of Magnetically Active Conditions on Stimulated Radiation during Ionospheric Modification Experiments

In this chapter, we examine the stimulated radiation of ion waves with HF radio wave with frequency near f_{ce}. The interaction altitude in the ionosphere for generation of these emissions was 160 km, which has 3 dominating ion (NO^+,O_2^+, O^+) species. This experiment was conducted during my participation in the SSRC 2011 campaign at HAARP. To explain the generation of the newly observed emission lines, I further developed PDI theory for multi-ion component plasma based on proton precipitation related to active conditions during the experiment. The next section provides the introduction with motivation and also the organization of the rest of the chapter.

4.1 Introduction

As mentioned in Chapter 2, Section 2.3.2, we have seen that for the past three decades since the discovery of stimulated electromagnetic emissions (SEE)[Thide et al., 1982], there has been an increasing interest in ionospheric high-frequency (HF) high power radio wave heating experiments. This is due to the wide range of ionospheric diagnostic information that has become available from the SEE spectrum, which can be used to determine the local magnetic field magnitude [Leyser et al., 1992], to determine the conditions for acceleration of electrons [Leyser et al., 2001], to measure electron temperatures [Bernhardt et al., 2009] and ion composition [Bernhardt et al., 2010]. Parametric decay of the high-frequency pump wave, transmitted from the ground, into other plasma wave modes is considered to be the

underlying theory for the generation of the features in an SEE spectrum [Leyser et al., 1991].

Recently there has been considerable interest in SEE with structures associated with ion-gyro frequency observed in the spectrum. [Bernhardt et al., 2010] reported on Magnetized Stimulated Brillouin Scatter (MSBS) of pump field decaying into high-frequency electromagnetic waves and low-frequency electrostatic ion cyclotron waves. This process has been of great interest due to the important diagnostic possibilities involving the ability to determine the mass of constitutive ions, and hence the ion composition of the ionosphere by measuring gyro-frequency at interaction altitude. Currently there are also observations of other distinctively different spectral features ordered by harmonics of the ion gyro-frequency. First observations of such structures were made in 2008 at HAARP and ordered by an O^+ gyro-harmonic frequency for second electron gyro-harmonic heating experiment [Bernhardt et al., 2011]. The heater was tuned at second electron gyro-harmonic $f_0 = 2.8MHz \approx 2f_{ce}$. The emission lines existed within 1 kHz of the pump and were ordered by ion gyro-frequency, which is typically 50 Hz for O^+. Figure 4.1 shows the O^+ gyro-harmonic structures: (a) shows the first observations, (b) and (c) shows the subsequent observations with heating at second and third gyro-harmonic heating respectively. The ion gryo-frequency structure produced by the MSBS process has typically been shown to produce no more than one harmonic. These new processes have been observed to produce many harmonics which may exist in a kHz band downshifted from the pump frequency. These structures appear most strongly when the pump frequency is near an electron gyro-harmonic (predicted by theory to be within 10 kHz). They have now been observed at both $2f_{ce}$ and $3f_{ce}$. The spectral lines typically exist at $(n+1/2)f_{ci}$. The gyro-harmonic structures are associated with airglow and upper hybrid waves. These structures are described in terms of parametric decay of upper hybrid/electron Bernstein waves into neutralized ion Bernstein waves and various aspects have been explained in terms of parametric instabilities in a single component plasma [Scales et al., 2011; Samimi et al., 2012, 2013].

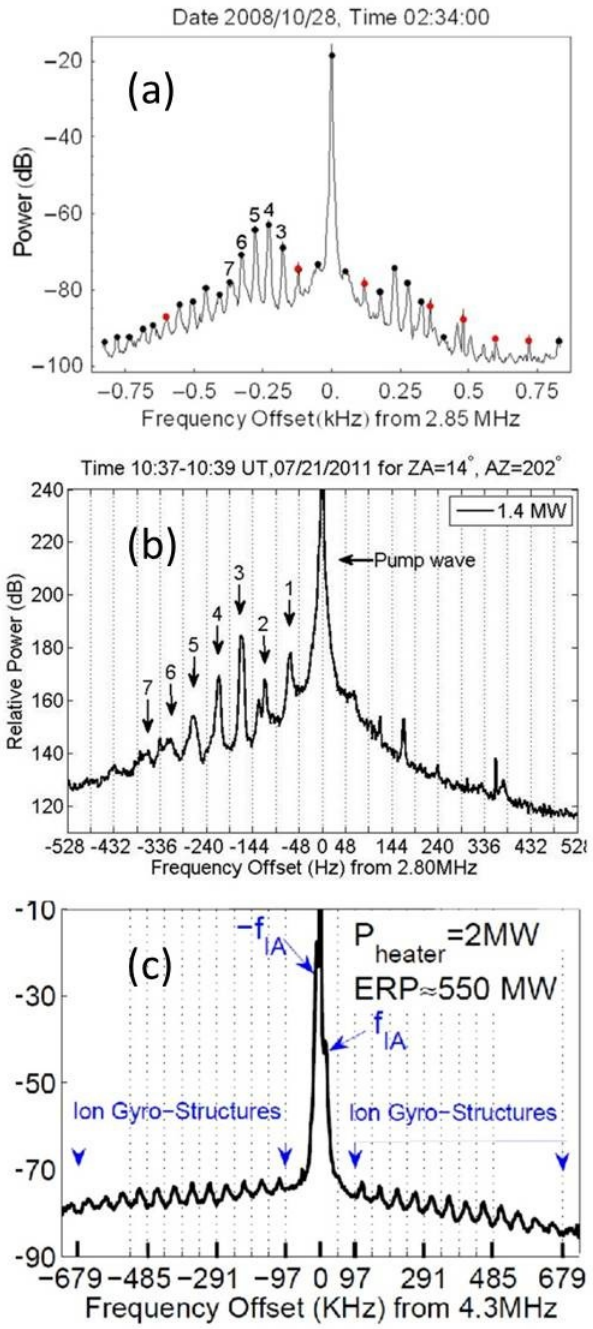

Figure 4.1: (a)First observations of O^+ gyro-harmonic structures near 2^{nd} electron gyro-harmonic. Figure reproduced from Bernhardt et al., 2011. (b)Further observations of 2^{nd} gyro-harmonic heating. Figure reproduced from Samimi et al., 2012, 2013. (c)Observations of 3^{rd} gyro-harmonic heating. Figure reproduced from Mahmoudian et al., 2013. Used under fair use, 2013.

The first observations of structuring near the H^+ (proton) gyro-frequency in the SEE spectrum during second electron gyro-harmonic heating experiments conducted during the SSRC campaign in July 2011, are described here. This is quite unusual since H^+ is a minority species and is much less than a percent of the plasma ion density under quiet conditions at altitudes of 160 km. However, the observations were made during a period of a relatively disturbed ionosphere as indicated by disturbed magnetogram and elevated absorption thought to be associated with proton precipitation [Galand and Chakrabarti, 2006; Ebihara et al., 2010]. Transportation of high energy protons is a more complicated process than that of electrons, since it involves charge exchange and ionization processes. These processes are described with coupled transport equations of the ions and the neutrals. Also ions travel in a helical path along magnetic field lines, while neutrals travel in the direction of velocity acquired at its creation. Figure 4.2 shows a sketch of this phenomenon. Because of the two different motions of ions and neutrals and its coupling, an initially narrow precipitating proton beam can spread out significantly as it penetrates the atmosphere.

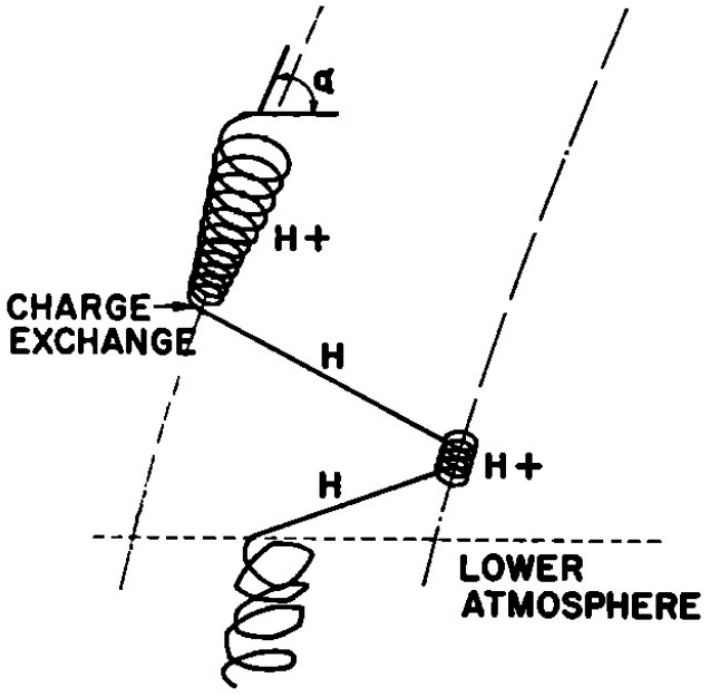

Figure 4.2: Sketch of proton and neutral path during precipitation into atmosphere. Figure reproduced from Davidson, 1965. Used under fair use, 2013.

This observation of H^+ structuring implies a multi-ion component plasma with a more complex wave mode behavior that must be considered. However, it provides possibilities for further diagnostics for determining the density of minority plasma species in ionospheric plasma that have not been considered before with such SEE measurements.

This work describes the first observations, proposes a possible theory and compares it to the observations. The next section provides the experimental setup and describes the observations made. Wave modes in a multi-component plasma of minority H^+ and majority NO^+, O^+, and O_2^+ ions are considered as possibilities for parametric decay of the pump field into high-frequency upper hybrid/electron Bernstein UH/EB waves and the appropriate low-frequency multi-ion species plasma modes. A comparison is made between the observations and the theory results, while a possible direction for future work is provided.

4.2 SEE Experiment

The current research's experiment was conducted between July 22, 2011 and July 25, 2011 at the High Frequency Active Auroral Research Program (HAARP) site at Gakona, AK. The SEEs were recorded using a HF receiver setup approximately 12 km from HAARP. The receiver system consisted of a 30 m folded dipole antenna and a receiver with estimated dynamic range of 90 dB. The receiver shifted the frequency of the acquired signal by the heater frequency by mixing and sampling it at 250 KHz. The received data was windowed (Blackman) and Fourier transformed to obtain the spectrograms of the obtained signal. The frequency resolution of the spectrogram is 5 Hz. The 30 minute experiment was organized into two 15 minute cycles of frequency stepping from 2.9 MHz to 3.0 MHz with 0.02 MHz step size. In the first cycle, the O-Mode beam was pointed vertically while in the second cycle it was pointed at magnetic zenith. The experiment was repeated with the same frequency and beam orientation settings to make it one hour long. For the whole experiment the transmitter was operated with 1 min ON and 1.5 min OFF duty cycle at full power of 3.6 MW in magnetic zenith (ERP=300 MW) and vertical (ERP=443 MW) directions.

4.3 Observations

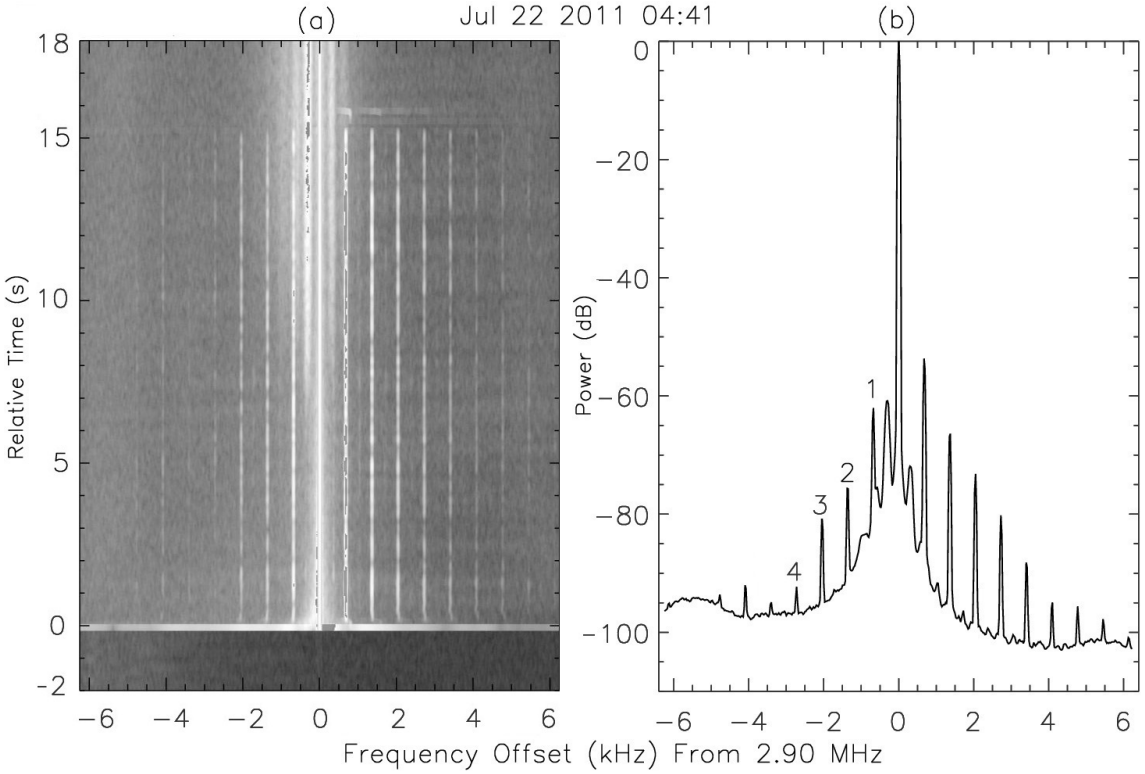

Figure 4.3: (a)SEE spectrogram showing emissions lines at harmonics of a frequency slightly less than the H^+ gyro-frequency that disappear after 15 seconds. (b) SEE spectrogram averaged over 20 seconds from the heater turn-on time.

During the hour (3:56 - 4:56UT)-long experiment on July 22, 2011 the ionosphere was relatively disturbed, with enhanced absorption recorded by digisonde and riometer from 04:36-04:42 UT. When the transmitter was turned on at 4:41 UT, both downshifted and upshifted emission lines appeared at harmonics of frequency less than the Hydrogen gyro-frequency ($f_{cH} \approx 789.76$ Hz) by about twice the Oxygen gyro-frequency ($f_{cO} \approx 49.36$ Hz) on the spectrogram as shown in Figure 4.3(a). HAARP was tuned at 2.9 MHz (near the second electron gyro-frequency f_{ce}) with the beam pointed at magnetic zenith (azimuth 202° and zenith angle 14°). The SEE spectra shows the pump at 2.9 MHz with the emission lines offset from the pump. The narrow lines shifted at harmonics of 689 Hz from the pump frequency appeared within a second after the pump was turned on and their intensity lasted for approximately 15 seconds. These lines only exist during periods when the pump is turned on, and are not related to spurious harmonics of the transmitter line frequency of 60 Hz. Therefore, they are taken to be of geophysical origin. The fundamental downshifted (Stokes) emission line first appeared within a few tenths of a second (0.1s). The other lines devel-

oped in the following few tenth of seconds with decreasing rate with increasing harmonic number. The downshifted (Stokes) emission lines were accompanied by strong upshifted (anti-Stokes) counterparts. Although the anti-Stokes lines had higher saturation amplitude, they developed at a slower rate compared to the Stokes lines. The narrow SEE harmonic lines disappeared abruptly within 0.1 seconds, except the fundamental, at 689 Hz, which decayed more slowly within 2 seconds. A broader line closer to the pump (centered near 296.16 Hz) appeared above the noise level after the pump was turned on for about 5 seconds and was present throughout the heating cycle. It was accompanied by a weaker upshifted anti-Stokes line. All these emission lines are seen clearly in the cross-section of the spectrogram in Figure 4.3(b). The cross-section of the spectrogram was computed by averaging over a period of 20 seconds from the time the heater was turned ON. The processed SEE shows the narrow lines are at harmonics of the n=1 line. This emission line is of maximum intensity and its harmonics (n=2, 3, 4) have monotonically decreasing intensity.

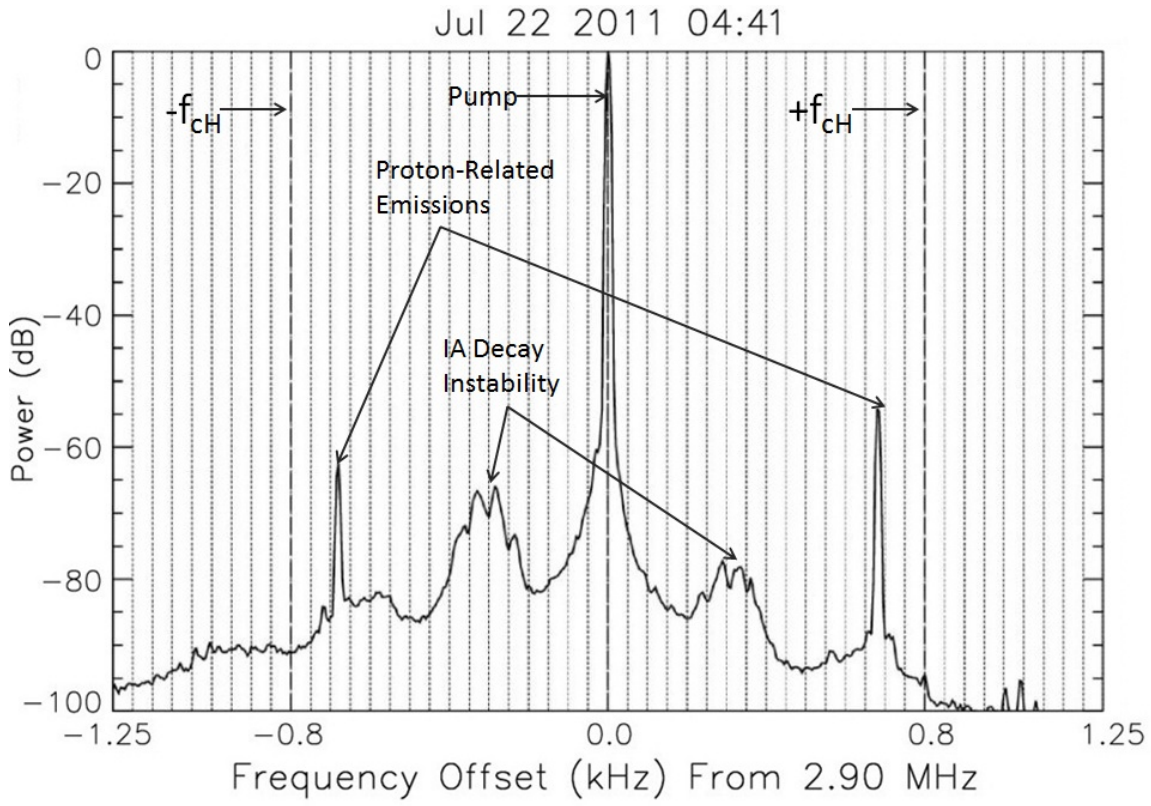

Figure 4.4: Narrowband version of Figure 4.3(b)with dotted and dashed grid lines at harmonics of f_{cO} and f_{cH} respectively, offset from the pump frequency. Note narrowband emissions near f_{cH}.

A narrowband cross-section of the spectrogram from Figure 4.3(a) is shown in Figure 4.4. Similar to Figure 4.3(b) it is averaged over a period of 20 seconds from the time the

heater was turned ON. The dotted grid lines are at f_{cO} harmonics and the dashed grid lines are at f_{cH}. The broader oblique ion acoustic (IA) instability with embedded oxygen gyro-harmonic structures [Samimi et al., 2012, 2013; Mahmoudian et al., 2013] is seen more clearly in this narrowband SEE spectrogram cross-section. It has a weaker upshifted anti-Stokes counterpart. The emission line at n=1 is about $2f_{cO}$ below f_{cH} and has bandwidth less than f_{cO}.

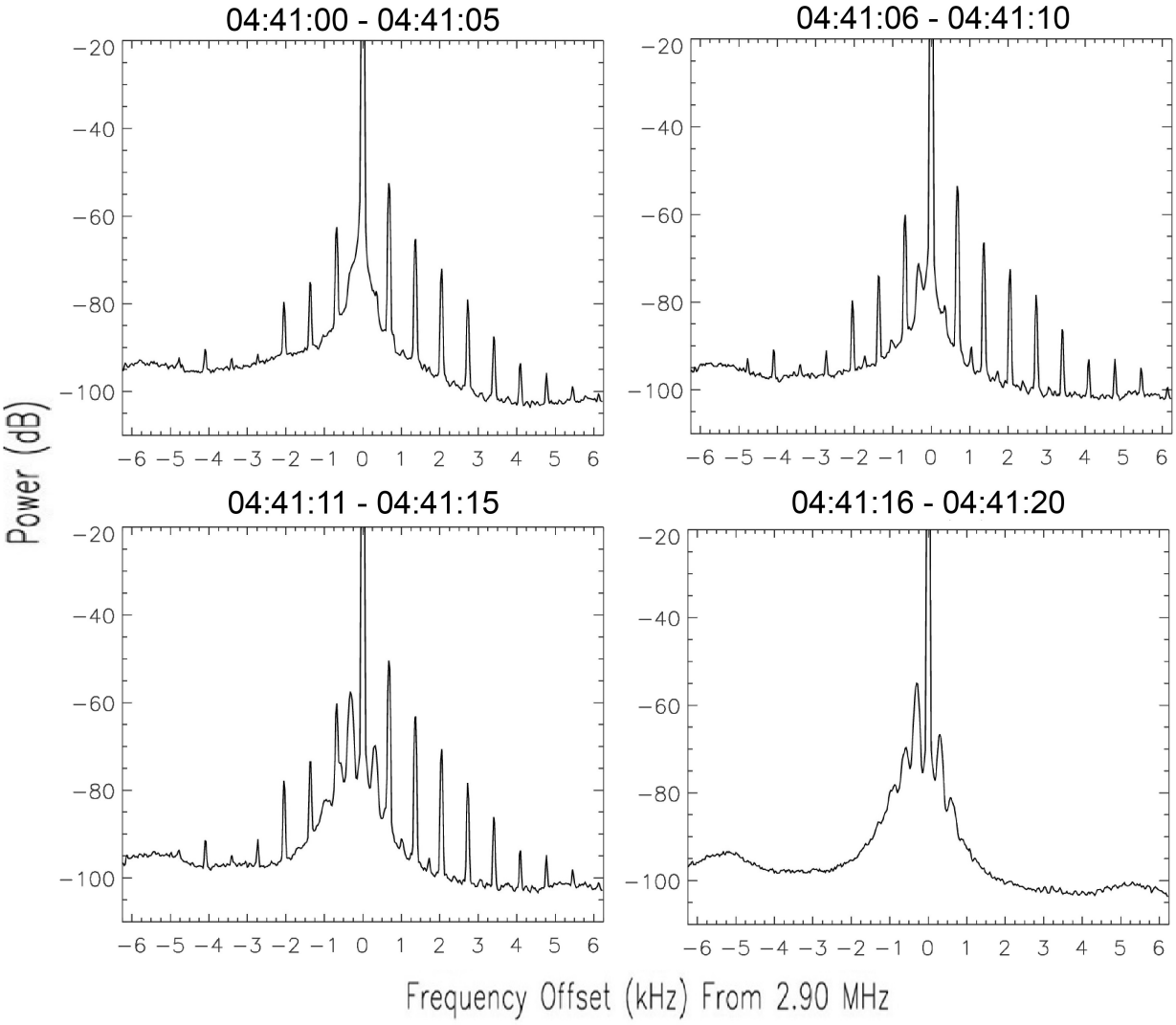

Figure 4.5: Time series of growth of emission lines for July 22, 2011 04:41 UT starting from heater turn-on time

Figure 4.5 shows the time series evolution of SEE spectrum starting from heater turn-on time. Each spectrum plot is averaged over different time periods as indicated in the figure. It is observed that the narrow narrow H^+ gyro-structures persisted for only 15 seconds while

O^+ gyro-related structures (i.e., IA decay instability) started growing about 10 seconds after heater turn-on and persisted throughout the entire heating cycle.

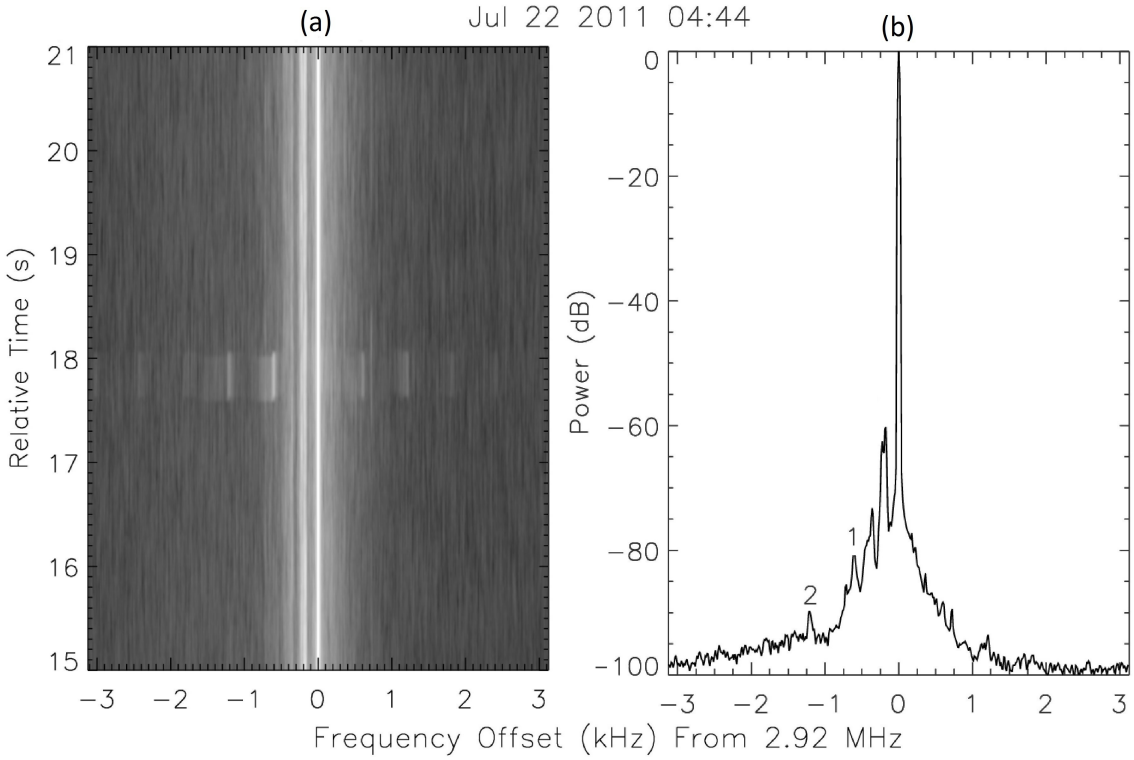

Figure 4.6: (a)SEE spectrogram showing short bursts at harmonics of a frequency slightly less than the H^+ gyro-frequency that lasted for 0.5 second on July 22, 2011 04:44 UT. (b) SEE spectrogram averaged over 2 seconds from 04:44:17 UT.

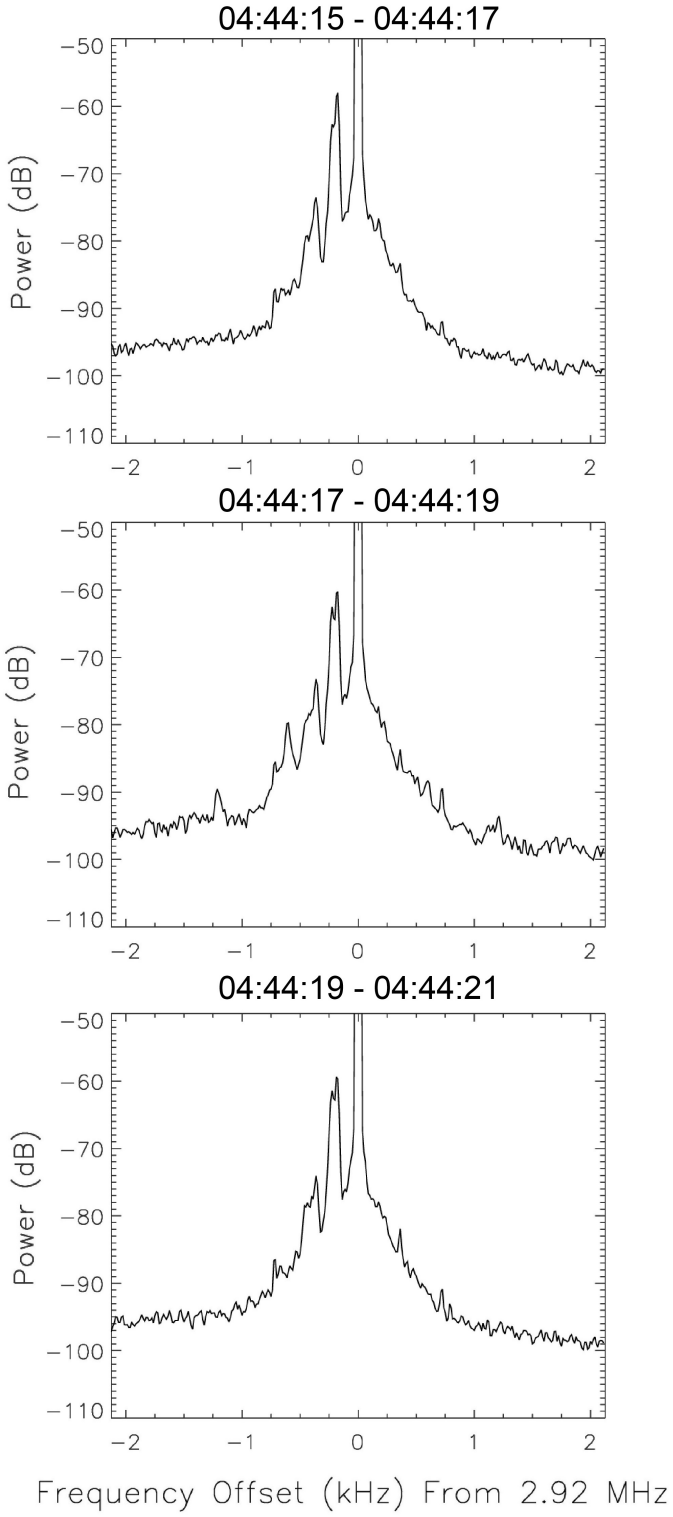

Figure 4.7: Time evolution of bursts seen on July 22, 2011 04:44 UT heating cycle

In the same hour-long experiment, when heater was turned on at 4:44 UT, short bursts of emission lines appeared at harmonics of 610 Hz below the pump and lasted for about 0.5 seconds. These bursts were accompanied by weaker anti-Stokes lines. The fundamental line was about $4\Omega_O$ below Ω_H. Figure 4.6 shows the spectrogram taken over the period of 6 seconds, 15 seconds after the heater turn-on. The cross-section shown is averaged over a 2-second period (04:44:17 - 04:44:19 UT). The oblique ion acoustic decay lines are the two lines closest to the pump at 225 Hz and 450 Hz respectively, and last for the entire heating cycle. Line $n = 1$ is the short burst at 610 Hz; the second harmonic is line $n = 2$. Other harmonics anti-Stokes lines are difficult to see above the noise level when averaged over a 2-second time period. Figure 4.7 shows the cross-section of the spectrogram with the closer view of the bursts and its harmonics. Each panel is averaged over 2 seconds; the top panel shows the cross-section before the burst appear, while the middle panel shows when the bursts appear, and bottom panel shows after the bursts. These are weaker emissions compared to the lines in Figure 4.3 and last for a substantially shorter amount of time.

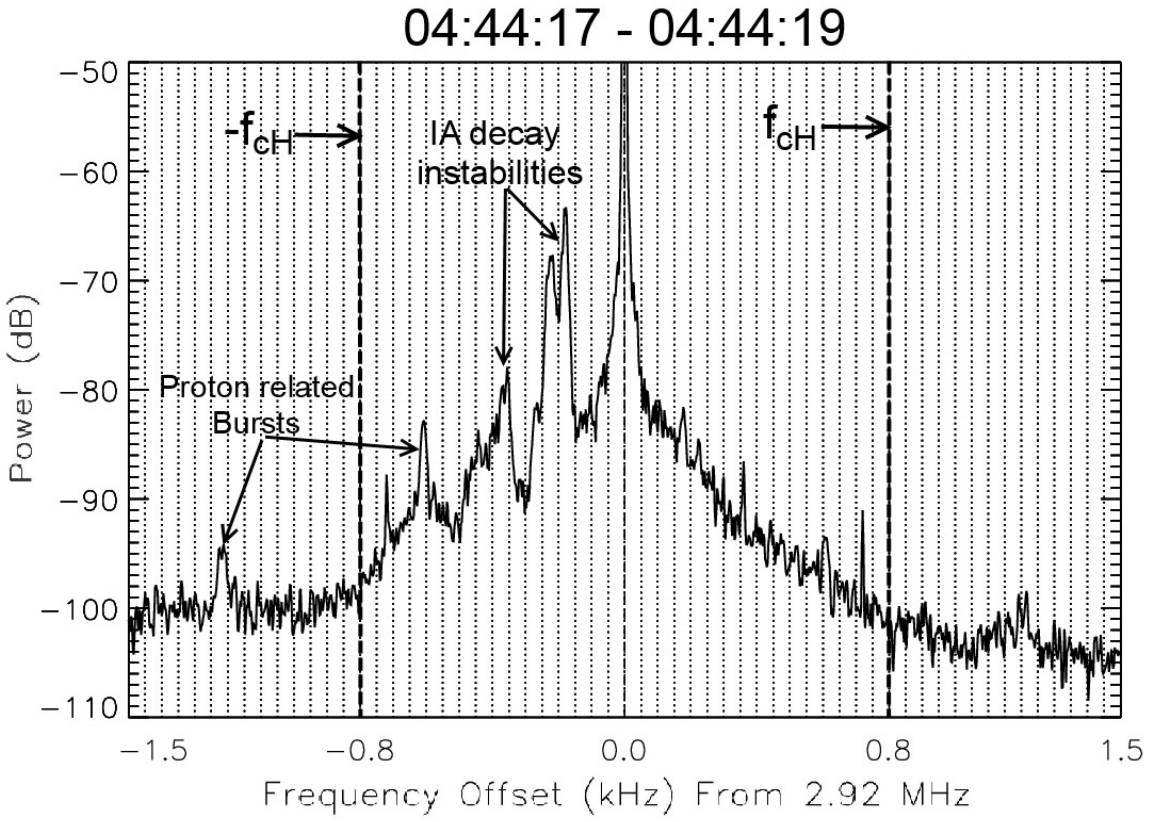

Figure 4.8: Narrowband version of Figure 4.6(b)with dotted and dashed grid lines at harmonics of f_{cO} and f_{cH} respectively, offset from the pump frequency. Note narrowband emissions near f_{cH}.

Figure 4.8 shows a narrow band cross-section of the spectrogram with dotted grid lines at harmonics of Ω_O and dashed grid lines at harmonics of Ω_H. The two broader lines below the pump closest to it are the ion acoustic decay lines with oxygen Bernstein structures embedded in it. The narrow weak peak at 610 hz below the pump is the short burst near Ω_H. The fundamental line and second harmonic are indicated in the figure. These structures are weaker than the ion acoustic decay lines and also exist for a very short time.

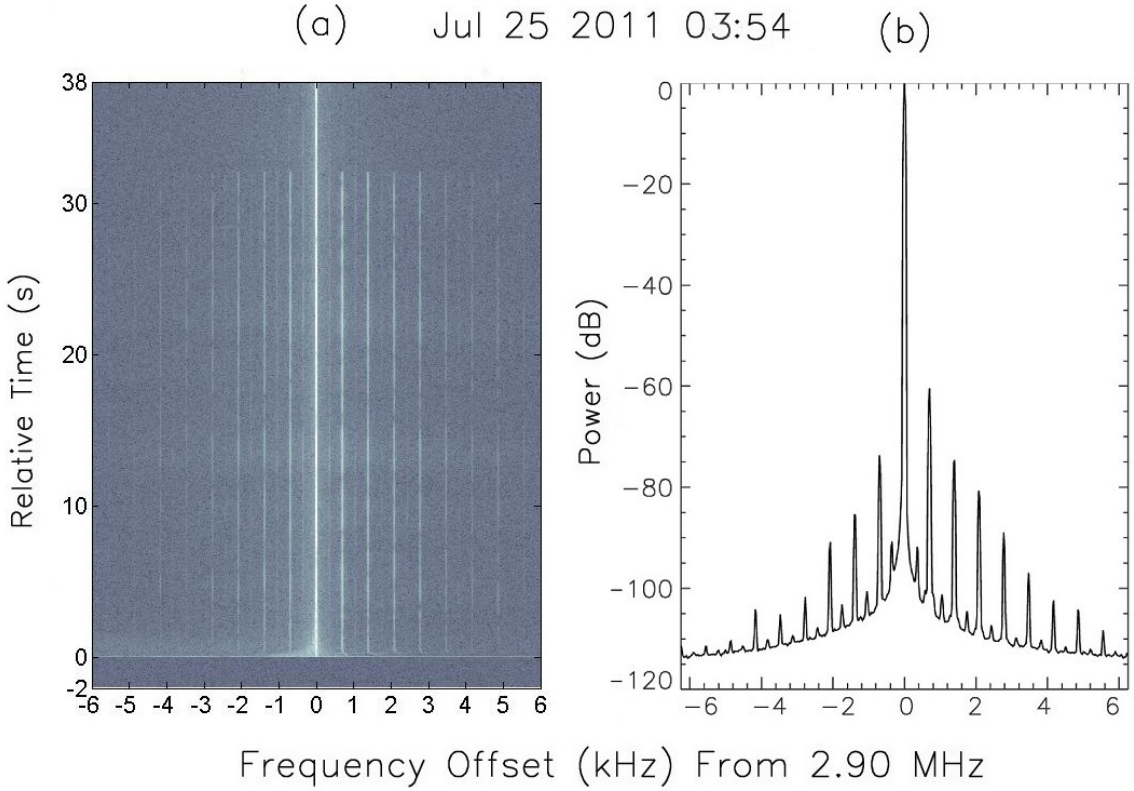

Figure 4.9: (a)SEE spectrogram showing emissions lines at harmonics of a frequency slightly less than the H^+ gyro-frequency that disappear after 30 seconds on July 25, 2011 03:54 UT. (b) SEE spectrogram averaged over 40 seconds from the heater turn-on time.

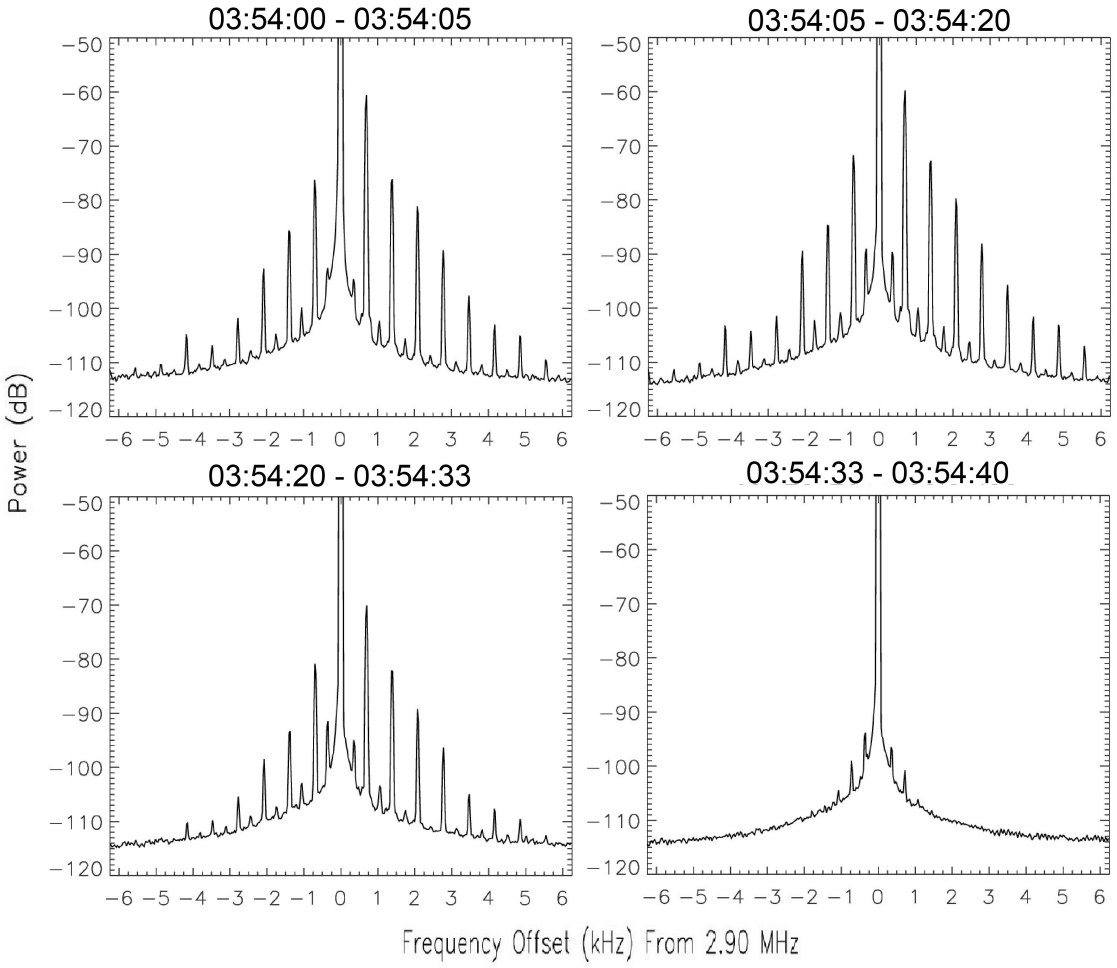

Figure 4.10: Time series of growth of emission lines for July 25, 2011 03:55 UT starting from heater turn-on time.

Another instance when similar observations were made during the campaign showed H^+ gyro-structures existed for 10's of seconds during the heating cycle. Figure 4.9 shows the spectrogram in the left- 4.9(a) panel, and cross-section of the spectrogram in the right panel. The plots show a relative time period of 40 seconds from heater turn-on period. Each of the cross-sections is averaged over 20 seconds. These observations were made on July 25, 2011 at 3:54 UT [Samimi et. al., 2012, 2013]. Similar to the previous case, when the transmitter was turned on at 3:54 UT, both downshifted and upshifted emission lines appeared on the spectrogram at harmonics of frequency less than the Hydrogen gyro-frequency by about twice the Oxygen gyro-frequency, as shown in Figure 4.9(a). HAARP was tuned at 2.9 MHz (near the second electron gyro-frequency f_{ce}) with beam pointing magnetic zenith (azimuth 202° and zenith angle 14°). The SEE spectra shows the pump at 2.9 MHz with the emission lines offset from the pump. The narrow lines appeared within a second the pump was turned on and their intensity lasted for 30 seconds. The downshifted (Stokes) emission lines were

accompanied by strong upshifted (anti-Stokes) counterparts. Relatively weaker emission lines were seen in between these H^+ gyro structures. These emission lines can be seen in the cross-section of the spectrogram in Figure 4.9(b). The cross-section of the spectrogram was computed by averaging over a period of 40 seconds. The processed SEE shows the narrow lines are at harmonics of the n=1 line ($\approx$ 700 Hz). This emission line is of maximum intensity and its harmonics (n=$2, 3, 4, 5, 6$) have monotonically decreasing intensity. The anti-Stokes lines are stronger than the Stokes lines. Emission lines also appear in between lines 1, 2, 3, 4, 5, 6 at harmonics of the n=a line. Figure 4.10 shows the evolution of the emission lines for 40 seconds from the heater turn-on time. Each cross-section of the spectrum has a closer view of the emission line. Each spectrum is averaged over different time periods as indicated in the figure. It can be seen that the emission lines persisted for about 32 seconds from the heater turn-on time.

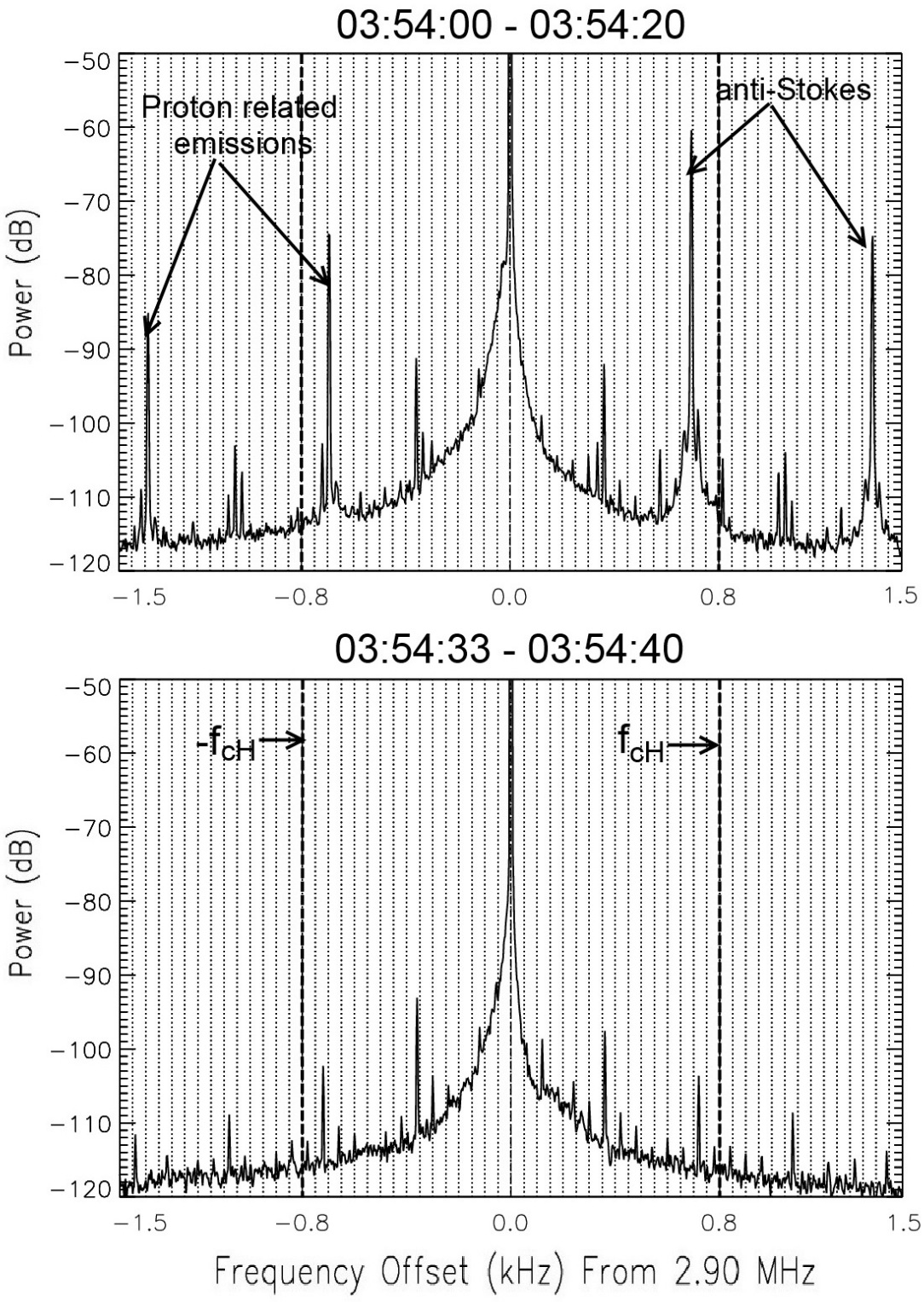

Figure 4.11: Narrowband cross-section of the spectrogram showing SEE obtained on July 25, 2011 averaged at different time periods as indicated.

Figure 4.11 shows a narrowband cross-section of the spectrogram. Each of the panels is averaged over different time periods. The top panel is averaged when the emission lines appeared and the bottom panel is averaged after the emission lines disappeared.

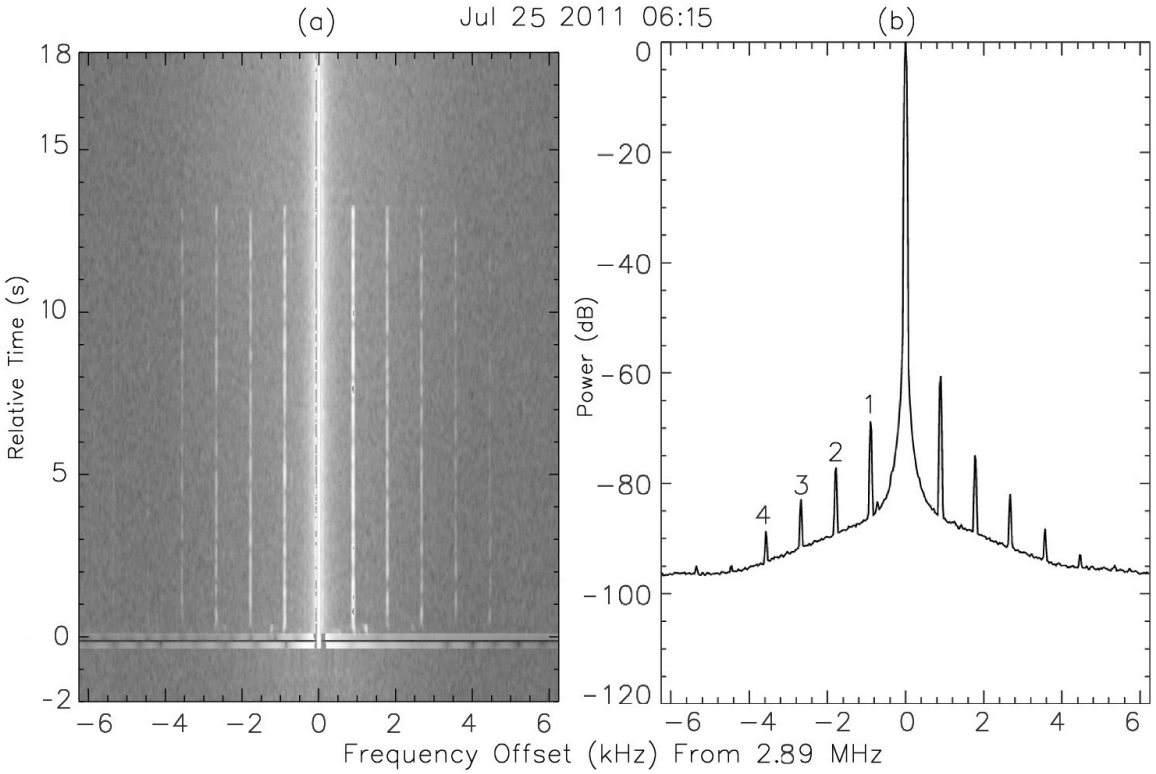

Figure 4.12: (a)SEE spectrogram showing emissions lines at harmonics of a frequency slightly higher than the H^+ gyro-frequency that disappear after 15 seconds on July 25, 2011 06:15 UT. (b) SEE spectrogram averaged over 20 seconds from the heater turn-on time.

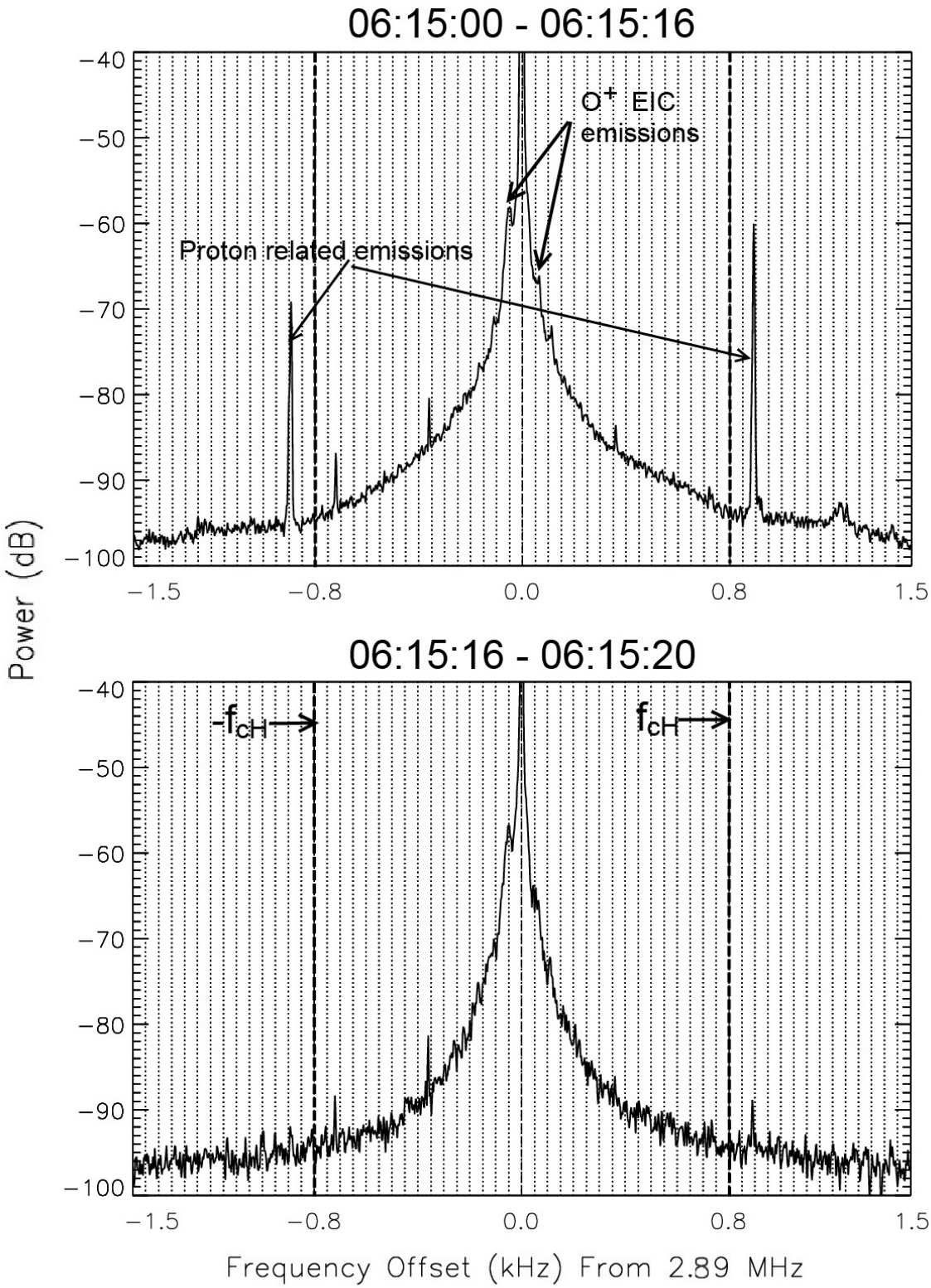

Figure 4.13: Time series of growth of emission lines for July 25, 2011 06:15 UT starting from heater turn-on time

A similar hour-long experiment performed on July 25, 2011 between 05:55-06:55 UT produced emission lines at harmonics of frequency greater than Hydrogen gyro-frequency by about twice the Oxygen gyro-frequency. Figure 4.12 shows the spectrogram in the left panel Figure 4.12(a) and the cross-section averaged over 20 seconds from heater turn-on time on the right panel Figure 4.12(b). The heater was turned-on at 06:15 UT and tuned at 2.89 MHZ. The emission lines were at harmonics of n= 1 line (≈900 Hz) which is above the Hydrogen gyro-frequency. These emission lines also lasted for about 15 seconds from the heater turn-on time. The cross-section of the SEE spectrum shows the harmonics of the emission lines-both Stokes and stronger anti-Stokes lines. Figure 4.13 shows the emission lines in a closer view with a narrowband cross-section. Here, again, the dashed grid lines are at $|omega_H$ and the dotted grid lines are at Ω_O. Each panel is averaged over different times with the top panel showing the emission lines above the Ω_H frequency by about $2\Omega_O$ and bottom panel showing SEE when the emission lines disappear. Again it is observed that these emission lines persist for a few seconds, or about 15. These narrowband cross-sections show emission line Ω_O below the pump. Note its second harmonic below the pump and the weaker anti-Stokes lines above it.

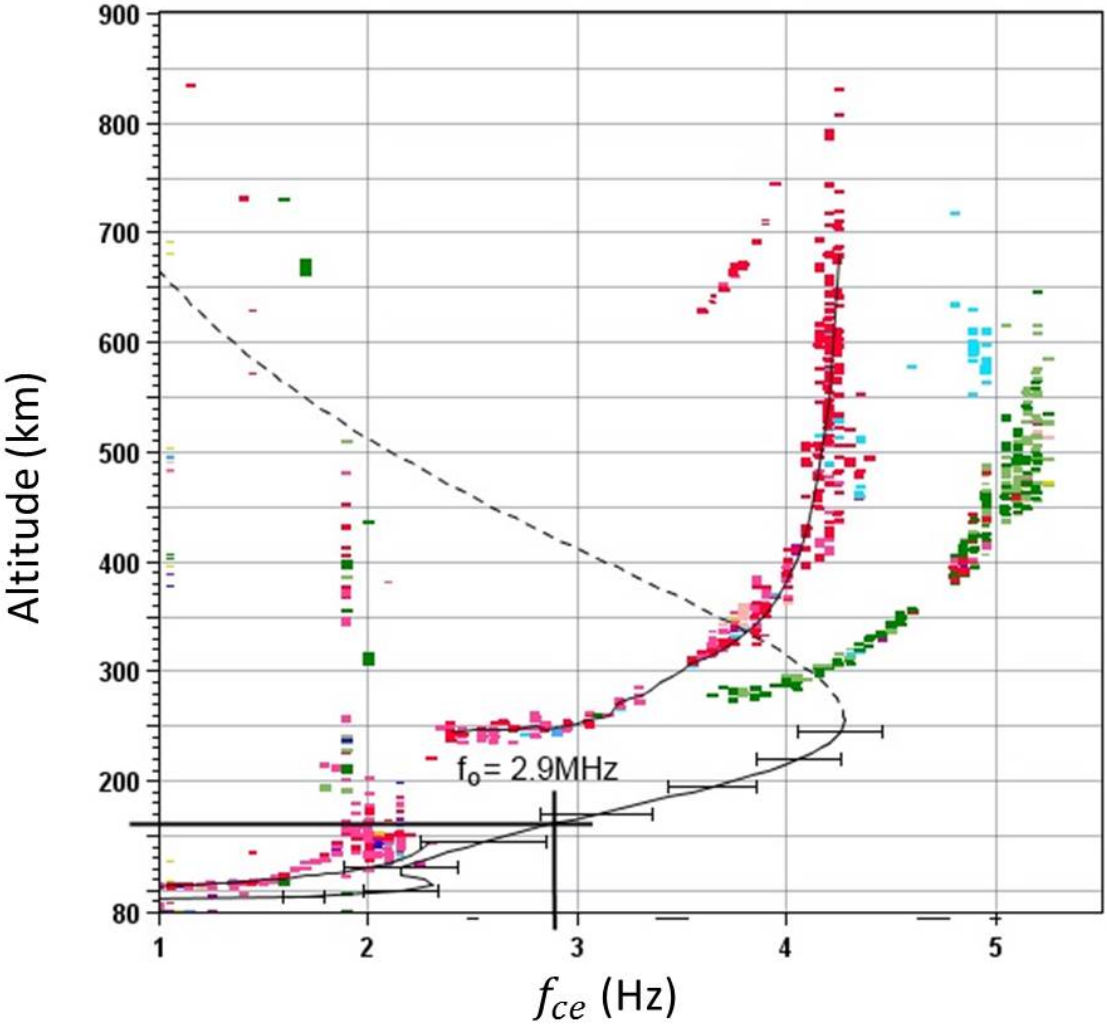

Figure 4.14: Ionogram taken on July 22nd, 2011 at a time near the heating cycle

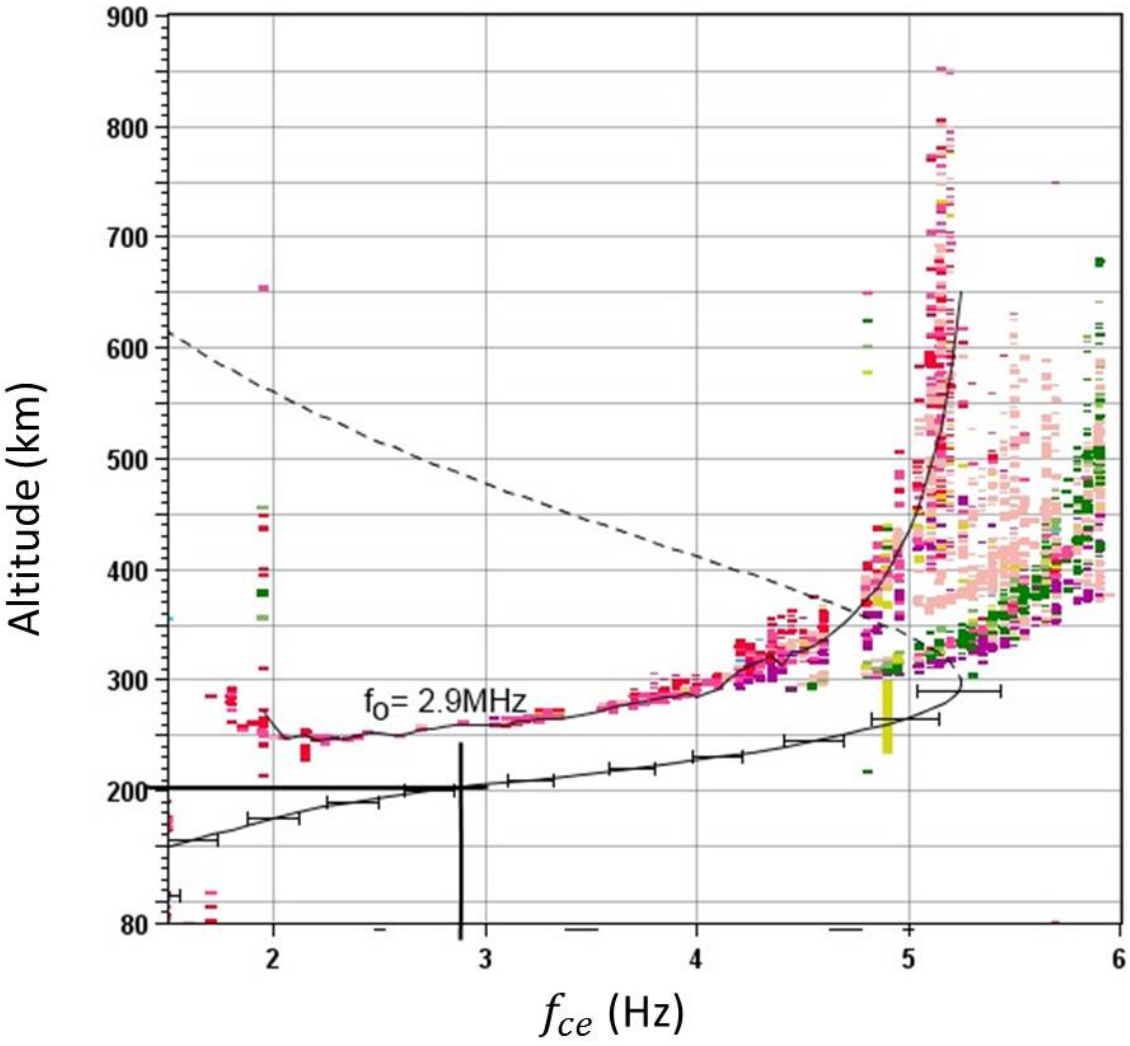

Figure 4.15: Ionogram taken on July 25th, 2011 at a time near the heating cycle

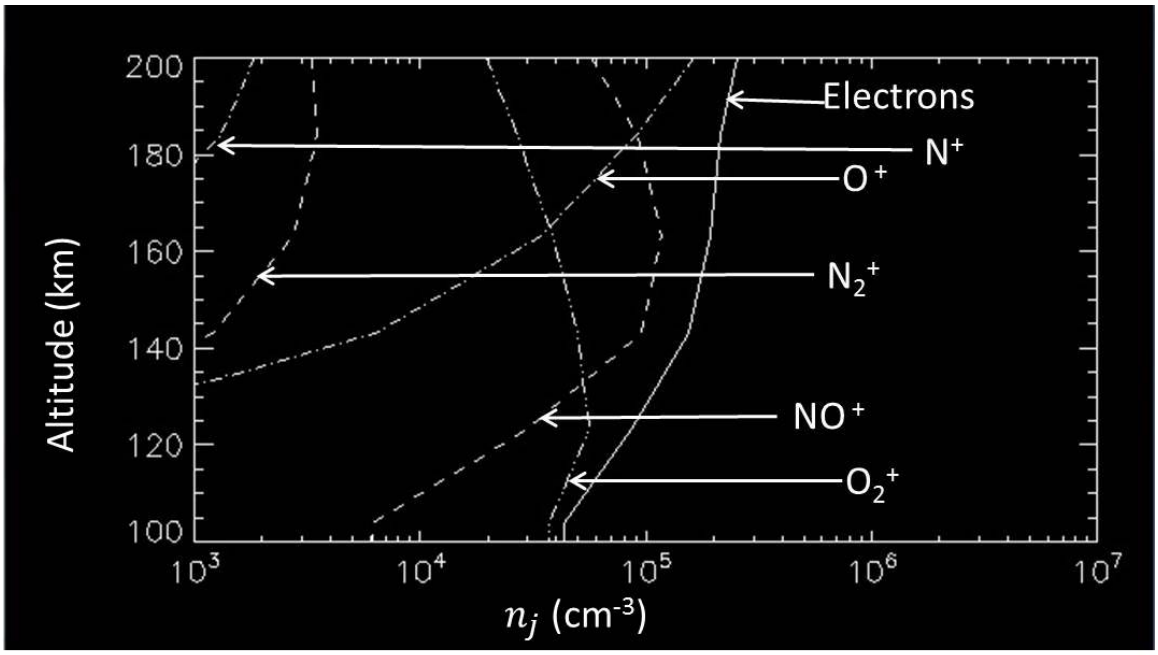

Figure 4.16: SAMI 2 simulation results for July 22nd 2011 above HAARP at 160 km

All the observations during the campaign show these H^+ gyro-structures exist for 10's of seconds during the heating cycle. The heating interaction altitude of approximately 160 km was determined from the ionograms obtained during the same time period. One such ionogram for July 22nd and July 25th is shown in Figure 4.14 and Figure 4.15 respectively. Figure 4.16 shows the results of SAMI2 code simulation at 160 km. Nitric oxide NO^+ is dominant with significant atomic O^+, and diatomic O_2^+ Oxygen ions. This indicates a multi-ion plasma; however, H+ density is negligible so the existence of these spectral lines is initially puzzling. It should be noted that the conditions were disturbed. Digisonde and riometer recorded relatively high absorption. These observations were obtained under disturbed ionospheric conditions. Figure 4.17 shows the fluxgate magnetometer (a) and riometer (b) readings around the heating period with the dashed line indicating heater turn-on time. The magnetometer showed increased magnetic field fluctuations after 03:00 UT. The peak to peak amplitude is $\approx 150nT$ in the H component. Absorption peaked at 0.25dB at 04:05UT and fell below 0.125dB during the heating cycle as seen in the riometer readings. The temporal behavior of the ion acoustic IA line is most likely due to the variation in absorption during the heating cycle as can be seen in Figure 4.17, which shows the beginning of relatively rapid reduction in absorption during the heating experiment which would allow development of the IA line. The IA lines are only observed during periods of negligible absorption [Samimi et al., 2012, 2013; Mahmoudian et al., 2013]. It is postulated that this event is associated with proton precipitation that produced significant quantities of H^+ for short periods [Ebihara et al., 2010]. It is known that precipitating KeV protons deposit much of their energy in the altitude range of 130- 200 km [Basu et al., 1987, Galand and Chakrabarti, 2006] which

brackets the heating interaction altitude. Protons with higher energy and smaller pitch angle can penetrate deeper into the atmosphere with less energy degradation, while protons with lower energy are deposited into higher altitude approximately-150 km and higher [Basu et al., 1987]. The SEE emission lines described here appeared near the end of the magnetic disturbance and lasted for the order of 10 seconds before disappearing.

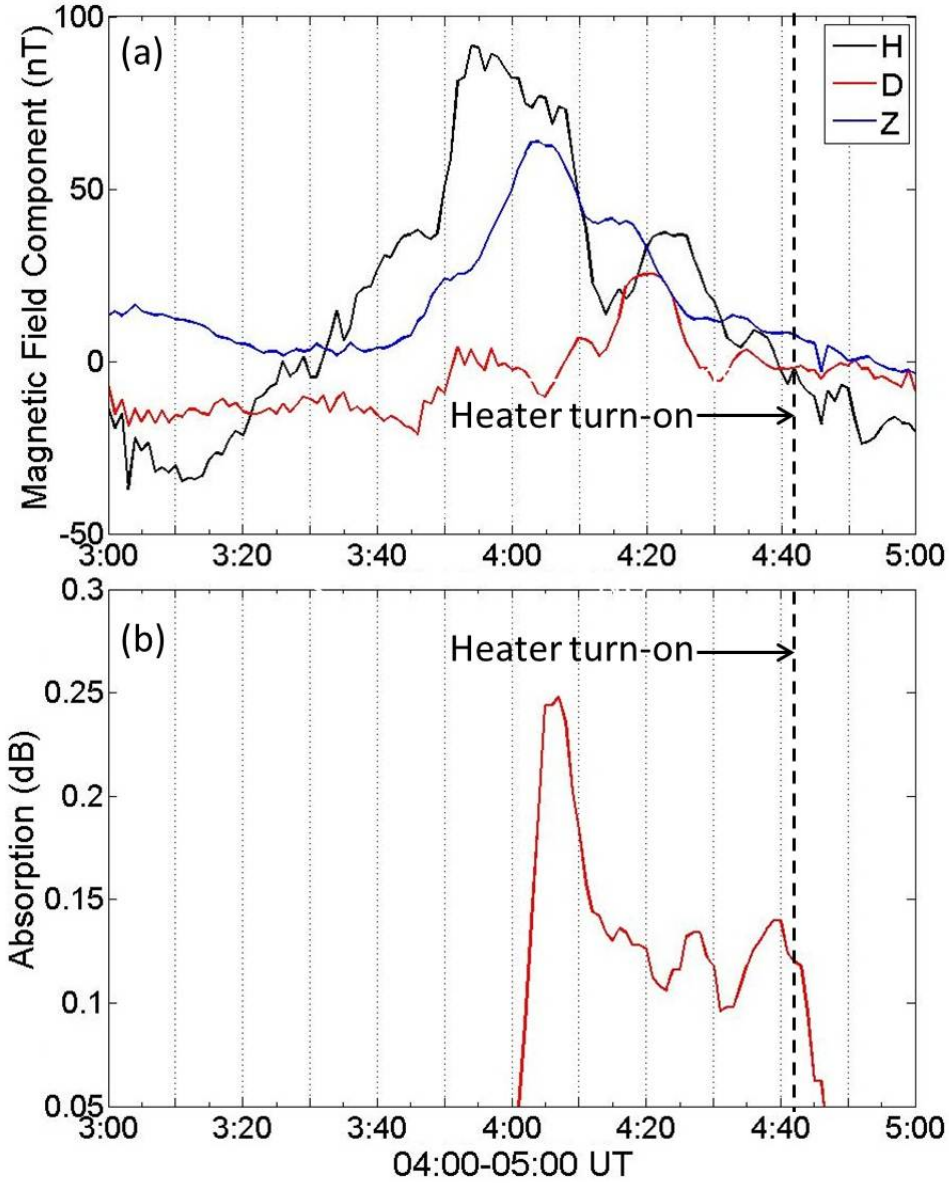

Figure 4.17: Two-hour plot of the readings of the (a) fluxgate magnetometer and (b) riometer located at Gakona, AK, on July 22, 2011. The dashed line indicates heater turn-on time in Figure 4.3 and 4.4.

Similar SEE emission lines observed on July 25, 2011 during the same campaign were seen during similar disturbed conditions. Figure 4.18 and 4.19 show a two-hour plot of the magnetometer and riometer readings for July 25, 2011 around the heating cycle corresponding to Figure 4.9 and 4.12 respectively. The dashed line in the figures indicates heater turn-on at 3:55 UT and at 06:15 UT. The SEE observations made at these times were correlated with 50-100 nT enhancements in magnetic activity. Riometer also showed a high absorption of 0.3 dB and 0.35 dB for 3:55 and 6:15 UT heating cycles respectively. These readings also indicate that these emissions are associated with disturbed conditions due to proton precipitation.

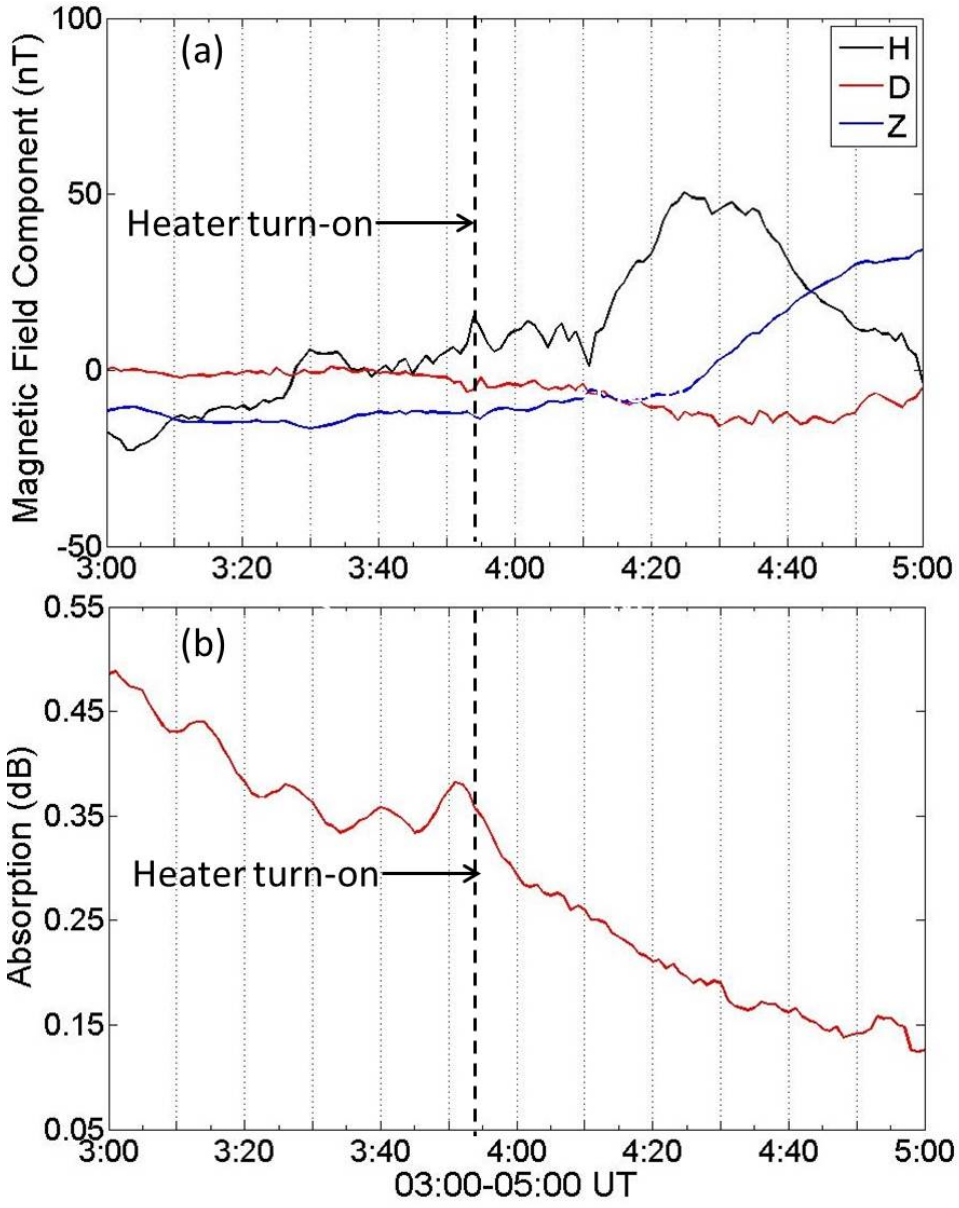

Figure 4.18: Two-hour plot of the readings of the fluxgate magnetometer located at Gakona, AK, on July 25, 2011, 03:00-05:00 UT. The dashed line indicates heater turn-on time in Figure 4.9.

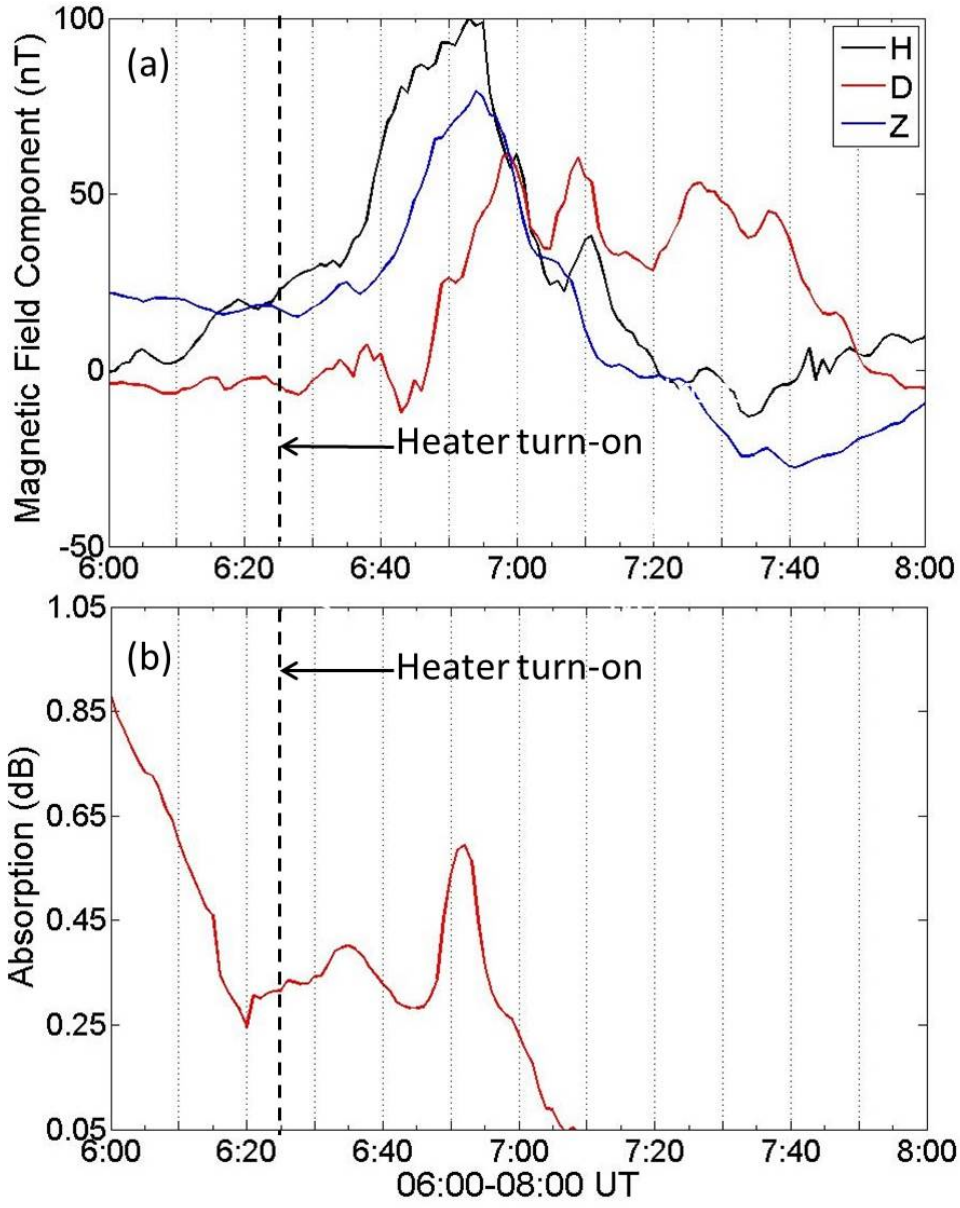

Figure 4.19: Two-hour plot of the readings of the fluxgate magnetometer located at Gakona, AK, on July 25, 2011, 06:00-08:00 UT. The dashed line indicates heater turn-on time in Figure 4.12.

Due to the proximity of these SEE emissions to f_{cH} (a minority species) and the narrow bandwidth, it is postulated that they involve parametric decay into low-frequency wave modes in a multi-ion component plasma. Figure 4.20 shows parametric decay mechanism near second gyro-harmonic heating. The pump wave goes through field aligned irregularities in the plasma and converts to a high-frequency upper hybrid UH/electron Bernstein EB mode,

which then parametric decays into a high-frequency upper hybrid UH/electron Bernstein and low-frequency ion waves, such as IB Ion Bernstein, IA Ion Acoustic, or a suitable ion wave. A three-wave parametric decay of pump in a multi-ion plasma with minority H^+ ions is proposed as a possible process for the generation of the narrowband emission lines in the SEE at the upper hybrid interaction altitude. This will be described below.

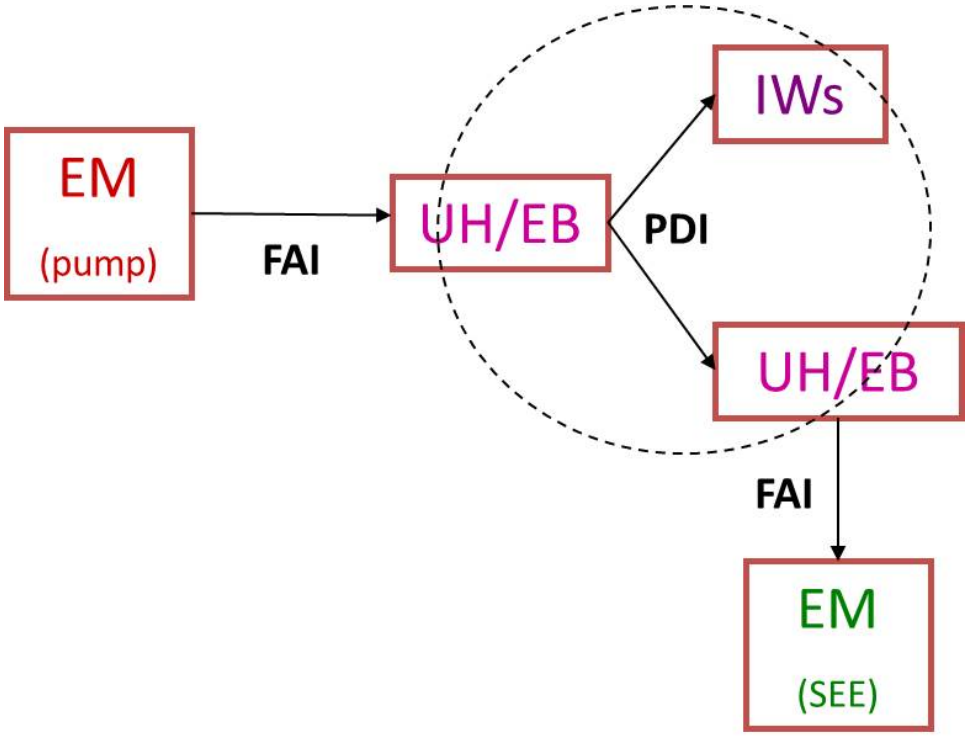

Figure 4.20: Parametric decay mechanism

4.4 Theory

At 160 km altitude, the ionospheric plasma consists primarily of nitric oxide NO^+, atomic O^+, and diatomic O_2^+ oxygen ions. The wave mode of interest for $f_{cO} << f < f_{cH}$ consistent with observations in Figures 4.3, 4.6 and 4.9, and propagation near perpendicular to the magnetic field $\vec{B}$, is the H^+-O^+ hybrid (or Buchsbaum) mode [Buchsbaum, 1960] which has physical analogies to the lower hybrid mode in a single ion plasma. The approximate plasma susceptibilities ($k_{||}/k < \sqrt{m_e/m_H}$) are given as $\chi_e \approx \omega_e^2/\Omega_e^2$, $\chi_i \approx \omega_i^2/(\Omega_i^2 - \omega^2)$ and $\chi_H \approx -(\omega_H^2/v_{th}^2 k^2) 2\Omega_H^2 \Gamma_1(b_H)/(\omega^2 - \Omega_H^2)$ respectively, where subscript e, i, and H denote electrons, (NO^+, O^+, O_2^+) ions, and H^+ ions, respectively; k is wavenumber, $k_{\perp(||)}$ is the perpendicular (parallel) component to $\vec{B}$, v_{tH} is H^+ thermal velocity ω_j and Ω_j are the species(j) (radian) plasma and gyro-frequency and $b_H = k_\perp^2 v_{tH}^2/\Omega_H^2 = k_\perp^2 \rho_H^2$ with ρ_H the H^+

gyro-radius. $\Gamma_1(b) = I_1(b)e^{-b}$ and I_1 is the modified Bessel function of 1^{st} order. The linear dispersion relation is given by $1+\chi_e+\sum_i \chi_i+\chi_H = 0$. The (radian) frequency ω is obtained by assuming $\omega \approx \Omega_H(1+\Delta)$ for low H^+ density where the frequency shift $\Delta << 1$. The solution is

$$\Delta \approx -\left(\omega_H^2/\sum_i \omega_i^2\right)\Gamma_1(b_H)/b_H \tag{4.1}$$

For long wavelengths $k_\perp \rho_H << 1$, $\Delta \approx -0.5\omega_H^2/\sum_i \omega_i^2$ and the H^+-O^+ hybrid (Buchsbaum) resonance frequency ω_{H-O} is attained. The simplified expression for Δ can be used with the shift of the SEE line below the f_{cH} in Figure 4.4 to provide a rough estimate of the hydrogen density ratio. Several percent of Hydrogen density is consistent with the observation assuming the SEE line is roughly at ω_{H-O} estimating the Hydrogen gyro-frequency to be 789.76 Hz, and the NO^+, O_2^+, O^+ densities to be 10^5, 4×10^4, and $2\times10^4 cm^{-3}$ as obtained from the SAMI II model (Huba et al., 2000).

From Figure 4.15 it can be seen that the interaction altitude for that heating cycle was near 210 km. At this altitude the dominating ion in the plasma was O^+. The wave mode with frequency slightly above the f_{cH} consistent with observations in Figure 4.12, is the electrostatic H^+ cyclotron wave, otherwise known as the neutralized H^+ Bernstein wave. The susceptibilities for electrons, oxygen and hydrogen for neutralized H^+ Bernstein mode ($k_{||}/k > \sqrt{m_e/m_H}$) are $\chi_e \approx k_e^2/k^2$, $\chi_O = k_e^2/k^2$ and $\chi_H \approx -(k_H^2/k^2)[2\Omega_H^2/(\Omega_H^2-\omega_H^2)]I_1(b_H)$ respectively. Assuming again the solution of the form $\omega = \Omega_H(1+\Delta)$ in the linear dispersion relation yields

$$\Delta \approx \frac{\Gamma_1(b_H)}{\frac{k^2}{k_H^2}+\frac{T_H n_e}{T_e n_H}\frac{T_H n_O}{T_O n_H}} \tag{4.2}$$

A three-wave parametric decay instability (PDI) of the pump wave into high-frequency upper hybrid UH/electron Bernstein and low-frequency H^+-O^+ hybrid waves in a multi-ion plasma with minority H^+ ions is proposed as a possible process for the generation of the narrowband emission lines in the SEE in Figures 4.3, 4.6 and 4.9 at the upper hybrid interaction altitude. The wavenumber and frequency matching conditions of $\vec{k_0} = \vec{k_1}+\vec{k_s}$ and $\omega_0 = \omega_1+\omega_s$, where subscripts $0, 1$ and s describe the pump field, high-frequency decay mode and low-frequency decay mode respectively, are used to describe the general dispersion relation of weak coupling [Porkolab, 1974; Ono et al., 1980]

$$\epsilon(\omega_s) + \frac{\beta_e^2}{4}\chi_\sigma(\omega_s)\left\{\frac{\epsilon_e(\omega_s)}{\epsilon_e(-\omega_1^*)} - 2\right\} = 0 \tag{4.3}$$

where $\epsilon(\omega) = 1+\chi_e(\omega)+\sum_i \chi_i(\omega)+\chi_H(\omega) = 1+\chi_e(\omega)+\chi_\sigma(\omega)$, and $\epsilon_e(\omega) = 1+\chi_e(\omega)$. The j^{th} plasma general susceptibility is,

$$\chi_j(\omega) = \frac{1}{k^2\lambda_{Dj}^2}\left\{1+\zeta_{j0}\sum_{n=-\infty}^{n=\infty}\Gamma_n(b_j)Z(\zeta_{jn})\right\} \tag{4.4}$$

where, $\Gamma_n(b_j) = I_n(b_j)\exp(-b_j)$ and $\zeta_{jn} = (\omega - n\Omega_j)/k_{||}v_{tj}$. λ_{Dj} is the Debye length of the j^{th} species. Z is the Fried Conte function. β_e is the coupling coefficient proportional to the pump field E_0 and is expressed as

$$\beta_e = \frac{e}{m_e} \quad \left\{ \left(\frac{E_{0||}k_{||}}{\omega_0^2} + \frac{E_{0\perp}\cdot k_\perp}{\omega_0^2 - \Omega_e^2} \right)^2 + \frac{(E_{0x}k_y - E_{0y}k_x)^2\Omega_e^2}{\omega_0^2(\omega_0^2 - \Omega_e^2)^2} \right\}^{1/2} \tag{4.5}$$

and $k_x^2 + k_y^2 = k_\perp^2$. The parametric decay process is assumed to occur near the upper hybrid altitude with a double resonance condition: i.e., $\omega_{uh} = 2\Omega_e$ where ω_{uh} is the upper hybrid frequency and $\omega_{uh}^2 = \omega_{pe}^2 + \Omega_e^2$ [Samimi et al., 2012, 2013; Mahmoudian et al., 2013]. Eq. (4.4) has been solved numerically with different input parameters of electron and ion temperature ratio, strength of the pump field calibrated with electron oscillating velocity $v_{osc} = eE_0/m_e\omega_0$ and pump electric field angle (θ_E) with respect to $\vec{B}$. Simplifications of a dipole pump field ($\vec{k}_0 = 0$) and neglect of collisional effects due to assumption of the pump field exceeding the PDI threshold are used.

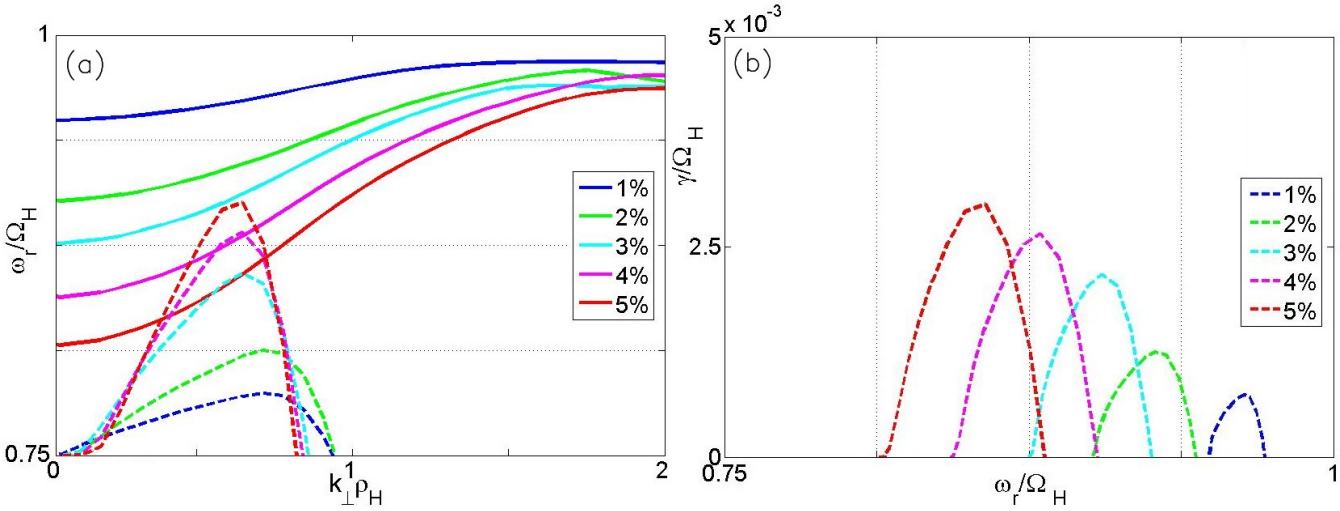

Figure 4.21: (a)PDI growth rate and dispersion relation of H^+-O^+ hybrid mode for different percentage of H^+ ions against the wavenumber with grid lines at harmonics of Ω_O. (b)PDI growth rate of H^+-O^+ hybrid mode for different percentage of H^+ ions against the real frequency normalized to Ω_H with grid lines at harmonics of Ω_O.

Figure 4.21 shows the numerical solution of the dispersion relation and growth rate of H^+-O^+ hybrid mode parametric decay instability (PDI) for different percentages for H^+ ions (colored lines). The bold lines are the solutions of the dispersion relation and the dashed lines are of the growth rate. Figure 4.21(a) shows dispersion relation and growth

rate against the wavenumber and Figure 4.21(b) shows the growth rate against the real frequency. The dotted grid lines are at harmonics of Ω_O. Note from frequency matching the low-frequency mode behavior describes the shift of the SEE line from the pump. The H^+-O^+ hybrid mode merges into various Bernstein modes in the multi-ion plasma for small wavelengths $k_\perp \rho_H >> 1$. θ_E which is the electric field angle with respect to $\vec{B}$ is taken to be $\theta_E = \pi/2 - 0.25\sqrt{(m_e/m_H)} = 89.66°$, and oscillating velocity $v_{osc} = eE_0/m_e\omega_0 = 0.95v_{te}(|E_0| \sim 10\text{V/m})$. It is assumed $T_e/T_i = 3$ [e.g., Samimi et al. 2012, 2013] and due to energy degradation $T_H/T_i = 1$; however, the importance of variation of this parameter will be discussed shortly. The electron density is $n_e = 3 \times 10^5 \text{cm}^{-3}$ and the temperature $T_e = 2500K$. The pump frequency is taken to be $\omega_0 = 2\Omega_e + 1\Omega_H$, and n_H/n_i which is the percentage of H^+ relative to the total ion density is varied from 1% to 5%. The variation in the solution of the hybrid mode with respect to the percentage of H^+ ions in the plasma is also observed in Figure 4.21. As the percentage of H^+ in the multi-ion plasma increases, the ω_{H-O} shifts further below Ω_H at long wavelengths ($k_\perp \rho_H << 1$). The value of maximum growth rate and its shift below Ω_H increases with an increase in the percentage of H^+. The growth rate increases roughly linearly with an increasing ratio of H^+ density n_H/n_i. Percentages of H^+ near 4-5% appear reasonably consistent with the frequency shift in the experimental observations. It is noted the growth time is approximately 0.5 seconds in this case. The bandwidth is typically of the order of Ω_O which has reasonable consistencies with the observations as well. It is noted that increasing T_H/T_i may significantly increase the emission bandwidth and reduce the growth rate. T_H should be no more than several times T_i for bandwidths of order Ω_O or less.

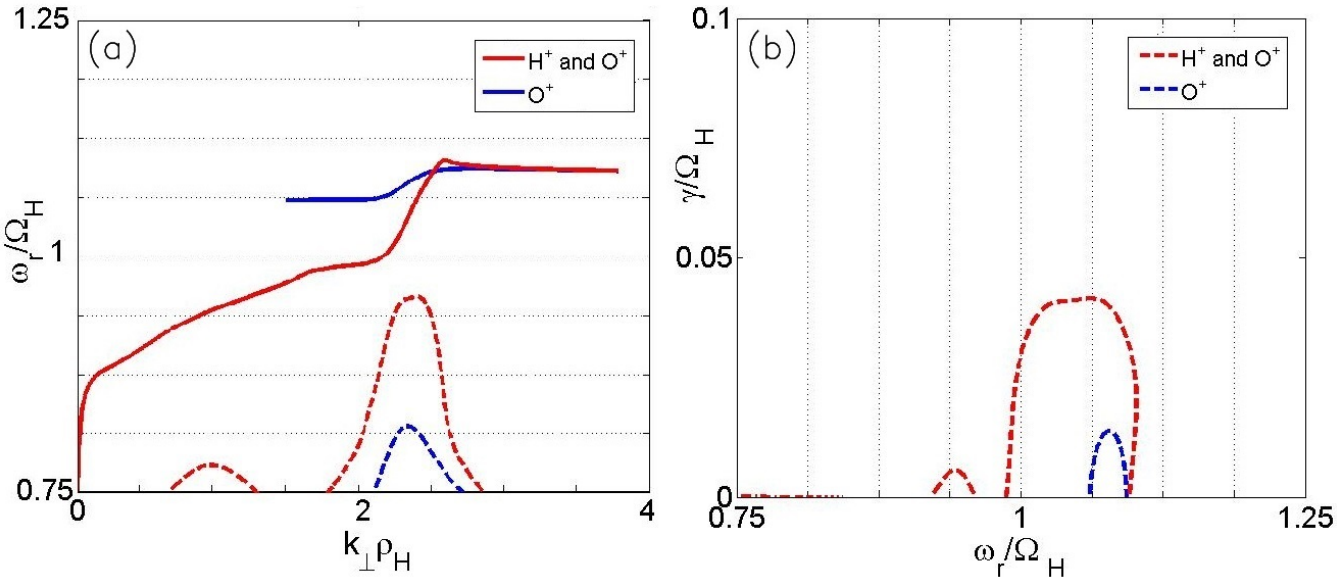

Figure 4.22: (a)PDI growth rate and dispersion relation of H^+ (red) related modes and neutralized O^+ Bernstein (blue) mode against the wavenumber with grid lines at harmonics of Ω_O. (b)PDI growth rate of H^+ (red) related modes and neutralized O^+ Bernstein mode (blue) against the real frequency normalized to Ω_H with grid lines at harmonics of Ω_O.

Figure 4.22 shows the numerical solution of the dispersion relation and growth rate of both H^+-O^+ hybrid mode and neutralized H^+ Bernstein mode (red) and neutralized O^+ Bernstein mode (blue) parametric decay instability (PDI). SEE lines above the H+ gyro-harmonic as seen in Figure 4.12 are neutralized H^+ Bernstein mode. This mode can be considered in the multi-ion component plasma as the low-frequency decay mode. This mode exists at larger inclination angles to magnetic field $\vec{B}$ and hence, here $\theta_E = \pi/2 - 1.3\sqrt{(m_e/m_H)}$, oscillating frequency is kept the same, and it is assumed $T_e/T_i = T_e/T_H = 3$ and n_H is 4% of n_i. The pump frequency is taken to be $\omega_0 = 2\Omega_e + 4\Omega_H$. Both the hybrid mode and neutralized H^+ Bernstein modes exist in the case with the growth rate of neutralized H^+ Bernstein mode larger. The excursion of the dispersion relation curve is $2\Omega_O$ above Ω_H in the large $k_\perp \rho_H$ regime before it merges into the Oxygen neutralized Bernstein mode. The bandwidth of the growth rate is approximately Ω_O. The analytical results indicate that the neutralized mode can be driven when the pump electric field vector must be at a larger off perpendicular angle, $\theta_E > \sqrt{(m_e/m_H)}$.

4.5 Discussion

This chapter presented evidence of minority (H^+) species structuring in the SEE spectrum during second electron gyro-harmonic heating under disturbed ionospheric conditions. These

emissions are correlated with magnetogram fluctuations in the 50-150 nT range and typically associated with the leading and trailing edge of the magnetic disturbance when absorption is sufficiently low to observe SEE. They are postulated to be the ultimate result of proton precipitation effects at the heating interaction altitude near 160 km. They are relatively short-lived and are observed to last for as long as 10's of seconds during the heating cycle (although, on occasion for just a few seconds). These newly discovered spectral features have the characteristics that they are narrowband, exhibit harmonic structure and often have frequency shifts slightly less (of order of 10%) than f_{cH} from the pump wave frequency. The Stokes and anti-Stokes lines also show monotonic decrease away from the pump frequency. The theory presented to produce the said emissions involves the parametric decay instability (PDI) in a multi-ion component plasma with several percent of H^+ density. The low-frequency decay mode in this case is the H^+- O^+ hybrid (Buchsbaum) mode. The results show reasonable agreement with experimental observations of downshifted sidebands observed in experimental observations. It is interesting to note the possible role of the Buschbaum hybrid mode in producing these emissions and the physical analogies to the lower hybrid mode which has long been considered to be responsible for producing the prominent Downshifted Maximum (DM) emission in the SEE spectrum in single-ion component ionospheric plasma [Leyser, 1991]. These new observations may indicate new possibilities for investigating characteristics of protons using heating experiments during active conditions. On rare occasions, the frequency shift of the emissions has been observed to be slightly larger than f_{cH}. Equation (4.3) can be shown to also exhibit growth of electrostatic Hydrogen cyclotron waves in the multi-ion plasma that show consistencies with the data. This requires larger θ_E in which the electron behavior is Boltzmann [Samimi et al. 2012, 2013]. Ongoing work is considering the physics of these emissions and diagnostic possibilities in more detail.

It should be noted that the weak coupling theory provided here does not describe the complex harmonic structure observed, which is most likely produced by nonlinear cascading processes [e.g., Zhou et al., 1994]. Further details and more sophisticated models using plasma simulations, which are beyond the scope of the current discussion, will be considered in future work. Other important aspects to be investigated include threshold of the pump power for the PDI generation, the critical proton density for PDI generation (which would imply a minimum observable frequency shift in Eq. (4.1)) and the impact of the proximity of the pump wave frequency to the second and higher electron gyro-harmonic frequencies. This study indicates that more careful experiments are needed to further access diagnostic capabilities for the interrogation of possible proton precipitation effects using the SEE spectrum during ionospheric heating experiments.

Chapter 5

Summary, Conclusion and Future Work

5.1 Summary and Conclusion

In this work, the instability processes generated during the active experiments in the ionosphere are discussed and analyzed using theoretical, observational and advanced computational methodologies. It is a step towards the ultimate goal to study and predict conditions in near-earth space so that we may better maintain our satellite communication technologies. Two active experiments were discussed: artificial dust layer injection, and stimulated electromagnetic emissions generated during second gyro-harmonic heating. The instabilities considered are lower hybrid instabilities generated due to shear-driven boundary between expanding and charging dust layer and background plasma, and due to streaming charged dust particles drifting in background plasma in the artificial dust layer experiment. New emission lines near H^+ gyro-harmonic frequency were observed during the second electron gyro-harmonic heating experiment.

Chapter 1 provided an introduction to this research with a brief summary of related prior work. Theoretical and numerical analyses performed previously on instabilities generated during dust injection/expansion process were given. Prior work and observations made during the SEE experiment were discussed and the fact that there is currently a growing interest in this new field was observed. An introduction to both the experiments was then given separately. In Chapter 2, background material for this research work was provided. A brief explanation of the ionosphere, plasma and its fundamentals was described and the classification of all space plasma experiments into passive and active experiments was made, with a detailed explanation of what active experiments entail. Charged Aerosol Release Experiment (CARE) was introduced with a background and motivation, followed by an introduction of SEE experiments. The chapter then reviewed important SEE features observed

during previous experiments.

Chapter 3 discussed irregularities of lower hybrid frequency range that were generated when dust aerosol particles were injected into the ionosphere. The chapter continued investigation of lower hybrid irregularities generated during the CARE experiment due to two different mechanisms. Lower hybrid instabilities were generated due to 1) shear vortices at the boundary of the injected dust cloud charging in the background plasma; and 2) the drifting charged dust particles in the background plasma. The first mechanism occured during early time scales when the dust particles were charging in the background plasma and inhomogeneities were created in the boundary layer. After several dust plasma periods, irregularities were mainly created by the second mechanism of charged dust particles drifting in background plasma. Both of these cases were investigated for different parameter regimes as per the CARE project. Both the instabilities were effective at generating lower hybrid irregularities for the CARE parameters, and both had comparable amplitudes. The difference was the time at which the irregularities were generated. Shear-driven instability developed during the early times of injection of the dust particles, while the streaming waves developed several dust plasma periods later. Shear-driven waves propagated along the dust cloud boundary with spatial scales of the order of the gradients in the cloud boundary. This kind of instability existed at larger inclination angles of the magnetic field. The saturation mechanism was the broadening of the boundary later and reducing the ambipolar electric field. Streaming waves were seen to develop along the streaming direction initially and on timescales of dust plasma periods. In this case, dust acceleration was the saturation mechanism. Both the irregularities had comparable density fluctuations in electron density, had spatial scales of meter scale or smaller and had velocity of the ion thermal speed. The processes discussed here should be observable both by ground-based and in situ space instruments.

New emission lines observed in the SEE near H^+ gyro-harmonic frequency during the second electron gyro-harmonic heating experiment were investigated in chapter 4. These new observations provided evidence of existence of minority (H^+) species near the heating altitude of 160 km. It should be noted that the ionospheric conditions were disturbed during the heating period. The fluxgate magnetometer indicated magnetic fluctuation of 50-150 nT range correlated with the heating cycle and the riometer showed sufficiently low absorption to observe the SEE during the same time. These observations were postulated to ultimately result in proton precipitation of H^+ at the heating interaction altitude. The emission lines were observed at harmonics of a frequency less than f_{cH} by about twice f_{cO}. They had narrow bandwidth comparable to f_{cO} and lasted for as long as 10's of seconds during the heating cycle. On one occasion these emission lines existed above the f_{cH} by twice f_{cO}. In all instances, both Stokes and anti-Stokes lines existed with monotonically decreasing amplitudes away from the pump. Three-wave parametric decay instability in multi-ion plasma was proposed as a possible generation method for these emission lines. Multi-ion species plasma consisted of three different kinds of ions in the background comparable to the interaction altitude, as shown by the SAMI 2 code and several percentage of H^+ density. The low-frequency decay mode was the H^+-O^+ hybrid mode for emission lines below f_{cH}

and neutralized H^+ Bernstein mode for emission lines above f_{cH}. Neutralized H^+ Bernstein mode required larger θ_E in which the electron behavior was Boltzmann [Samimi et al., 2012, 2013]. The results show reasonable agreement with the experimental observations. These new observations may indicate new possibilities for investigating characteristics of protons using heating experiments during active conditions.

This research has made the following original contributions:

1. Hybrid code was developed to incorporate injection of dust cloud at oblique angles to background magnetic field. The irregularities studied existed at a larger inclination angle to the magnetic field (Chapter 3).

2. Special boundary conditions involving dust cloud injection were implemented. This new condition allowed the study of the shear-driven instability generated due to charging dust cloud injected from one boundary of the simulation box and taken out of the opposite boundary. The saturation for this instability is the broadening of this inhomogeneous boundary between the dust cloud and background plasma (Chapter 3).

3. Dust particle collisions were implemented using the Monte Carlo algorithm. Ion collisions with plume neutrals were also considered to investigate its effects on shear-driven instability, which may be important at early times. Parameters considered are in the CARE project regime, and investigation by several simulation runs showed reduction in the ambipolar electric field and hence reduced saturated wave field energy. Spatial vortex structures were less pronounced but the growth and saturation amplitude were not changed substantially (Chapter 3, results in Figure 3.7).

4. Ion wave-particle damping process was included for more accurate non-linear evolution. ν_L^* term for modeling ion Landau damping written in wavenumber space was added in the momentum equation for unmagnetized ion velocity. This was accordingly implemented in the hybrid code (Chapter 3).

5. First observations of ion (H^+) structuring in stimulated radiation during second electron gyro-harmonic heating experiments were made. This was quite unexpected; H^+ is a minority ion at the heating interaction region near 160 km. Proton precipitation was postulated as a reason for appearance of these emission lines in the SEE spectrum during active ionospheric conditions (Chapter 4, Section 4.3).

6. A three-wave parametric decay instability (PDI) of the pump wave into high-frequency upper hybrid UH/electron Bernstein and low-frequency H^+-O^+ hybrid waves and neutralized H^+ Bernstein waves in a multi-ion plasma with minority H^+ ions was proposed as a possible process for the generation of the narrowband emission lines in the SEE at the upper hybrid interaction altitude. Plasma with three major species, nitric oxide (NO^+), diatomic oxygen (O_2^+) and atomic oxygen (O^+) and minor species of hydrogen

(H^+) ions were considered. A numerical method for theoretical analysis was developed to investigate the growth rate of the two low-frequency modes in parameter regimes pertaining to the heating experiment (Chapter 4, Section 4.3).

5.2 Related Publications by the Author

Several publications related to this research have been written. These include two journal papers published as first author, one journal paper in preparation to be submitted as first author, two co-author journal papers, one co-author conference paper and five posters. The first author published journals include [Bordikar et al., 2012, 2013] published in IEEE transactions on Plasma Science and Geophysical Research Letters. The manuscript in preparation is to be submitted to the Journal of Geophysical Research. The co-author papers include [Scales et al., 2010; Scales et al., 2011; Mahmoudian et al., 2013] published in IEEE transactions on Plasma Science, General Assembly and Scientific Symposium, URI, and Journal of Geophysical Research respectively. Five poster papers were presented at the RF Ionospheric Interactions Workshop in April 2009, 2010 and 2011 and AGU Fall meeting 2009 and 2010.

5.3 Future Work

This study has presented an investigation of lower hybrid irregularities generated during dust cloud release experiments in near-earth space environment, along with new observations of H^+-O^+ hybrid mode and neutralized H^+ Bernstein mode emission lines in SEE during a heating experiment. Both of these studies were conducted on active experiments performed in the ionosphere. A hybrid (PIC and fluid) numerical code was used to study the lower hybrid irregularities generated in two different time scales by different mechanisms. There are various kinds of irregularities that could be generated during a dust cloud release in the earth's ionosphere. For instance, other possibilities include ion acoustic or dust acoustic irregularities [Fu et al., 2011; Mahmoudian et al. 2012]. The present investigation only considers irregularities associated with relatively high-frequency lower hybrid waves. The spectrum of these possibilities will be investigated as ongoing work.

Future work in stimulated radiation heating experiments should consider the physics of these emissions and diagnostic possibilities in more detail. It should be noted that the weak coupling theory provided here, does not describe the complex harmonic structure observed, which is most likely produced by nonlinear cascading processes [e.g., Zhou et al., 1994]. Further details and more sophisticated models that use plasma simulations, which are beyond the scope of the current discussion, will be considered in future work. Other important aspects to be investigated include threshold of the pump power for the PDI generation, the critical proton density for PDI generation (which would imply a minimum observable frequency shift in Eq. (4.1)), and the impact of the proximity of the pump wave frequency to

the second and higher electron gyro-harmonic frequencies. This study indicates that more careful experiments are needed to further access diagnostic capabilities for interrogation of possible proton precipitation effects using the SEE spectrum during ionospheric heating experiments.

Bibliography

[1] Basu, B., J. R. Jasperse, R. M. Robinson, R. R. Vondrak, and D. S. Evans (1987), Linear transport theory of auroral proton precipitation: A comparison with observations, J. Geophys. Res., 92(A6), 59205932, doi:10.1029/JA092iA06p05920.

[2] Bernhardt, P. A., L. S. Wagner, J. A. Goldstein, V. Y. Trakhtengerts, E. N. Ermakova, V. O. Rapoport, G. P. Komrakov, and A.M. Babichenko, Enhancement of stimulated electromagnetic emission during two frequency ionospheric heating, Phys. Rev. Lett., 72, 2879, l1994.

[3] Bernhardt, P. A., G. Ganguli, M. C. Kelley, and W. E. Swartz (1995), Enhanced radar backscatter from space shuttle exhaust in the ionosphere, J. Geophys. Res., 100 (A12), 23,811-23,8185.

[4] Bernhardt P. A. (2009), An update on charged aerosol release experiment CARE, talk AGU Fall 2009 meeting

[5] Bernhardt, P. A., C. A. Selcher, R.H. Lehmberg, J. Rodriguez, J. Thomason, M. McCarrick, and G. Frazer (2009), Determination of the electron temperature in the modified ionosphere over HAARP using the HF pumped stimulated Brillouin scatter (SBS) emmision lines , Ann. Geophys., 27, 4409-4427, doi:10.5194/angeo-27-4409-2009.

[6] Bernhardt, P. A., C. A. Selcher, R. H. Lehmberg, S. P. Rodriguez, J. F. Thomason, K. M. Groves, M. J. McCarrick, and G. J. Frazer (2010), Stimulated Brillouin Scatter in a Magnetized Ionospheric Plasma , Phys. Rev. Lett., 104, 16, 165004, doi:10.1103/PhysRevLett.104.165004.

[7] Bernhardt P. A., J.B. Baumgardner, A.N. Bhatt, P.J. Erickson, M.F. Larsen, T.R. Pedersen and C.L. Siefring (2011), Optical Emissions Observed During the Charged Aerosol Release Experiment (CARE I) in the Ionosphere, IEEE Trans. Plasma Sci., vol 39, No. 11, pp. 2774-2775

[8] Bernhardt, P. A., C. Selcher, and S. Kowtha (2011), Electron and ion Bernstein wave excited in the ionosphere by high power EM waves at the second harmonic of the electron cyclotron frequency, Geophys. Res. Lett., 38, L19107, doi:10.1029/2011GL049390.

[9] Bernhardt, P. A., J. B. Baumgardner, A. N. Bhatt, A. Coster, P. J. Erickson, C. R. Kaplan, R. A. Haaser, M. F. Larsen, F. D. Lind, T. R. Pedersen, R. F. Pfaff, P. A. Roddy, S. P. Rodriquez, P. W. Schuck, C. L. Siefring, S. M. Smith, E. R. Talaat, and J. F. Thomason (2012), Ground and space-based measurement of rocket engine burns in the ionosphere, IEEE Trans. Plasma Sci., 40, 1267-1286.

[10] Bharuthram R, M Rosenberg (1998) A note on the generation of fluctuations by Space Shuttle exhaust in the ionosphere Planet. Space Sci., 46, p. 425.

[11] Birdsall, C. K., and A. B. Langdon (1991), Plasma Physics via Computer Simulation , New York: McGraw-Hill.

[12] Bordikar, M. R., and W. A. Scales (2012), Lower hybrid turbulence associated with creation of dusty plasmas in the near-earth space environment, IEEE Trans. Plasma Sci., 40, 946-953.

[13] Bordikar, M. R., W. A. Scales, A. R. Samimi, P. A. Bernhardt, S. Brizcinski, and M. J. McCarrick (2013), First observations of minority ion (H+) structuring in stimulated radiation during second electron gyro-harmonic heating experiments, Geophys. Res. Lett., doi:10.1002/grl.50327.

[14] Buchsbaum, S. J. (1960), Resonance in a Plasma with Two Ion Species , Phys. Fluids 3, 418; doi: 10.1063/1.1706052.

[15] Chae G. S., W.A. Scales, G. Ganguli, P.A. Bernhardt, and M. Lampe (2000), Numerical model for low-frequency ion waves in magnetized dusty plasmas, IEEE Trans. Plasma Sci., vol. 28, pp. 1694-1705.

[16] Chen, Francis F., (1984), Introduction to Plasma Physics and Controlled Fusion, Volume 1, Plenum Press, New York.

[17] Cho J. Y. N. and M.C. Kelley (1993), Polar mesospheric summer radar echoes: Observations and current theories, Rev. Geophys., vol. 31, pp. 243-265.

[18] Cho J. Y. N. and J.Rottger (1997), An updated review of polar mesospheric summer echoes: observations, theory and their relationship to noctilucent clouds and subvisible aerosols, J. Geophys. Res., vol. 102, pp. 2001-2020.

[19] Cohen, M. B., M. Golkowski, and U. S. Inan (2008), Orientation of the HAARP ELF ionospheric dipole and the auroral electrojet, Geophys. Res. Lett., 35, 2806-+, doi:10.1029/2007GL032424.

[20] Cohen, M. B., U. S. Inan, M. Golkowski, and M. J. McCarrick (2010), ELF/VLF wave generation via ionospheric HF heating: Experimental comparison of amplitude modulation, beam painting, and geometric modulation, Journal of Geophysical Research (Space Physics), 115(A14), 2302-+, doi:10.1029/2009JA014410.

[21] Davidson G. T. (1965), Expected spatial distribution of low-energy protons precipitated in the auroral zones, J. Geophys. Res., vol. 70 no. 5, pp. 1061-1068.

[22] Dysthe, K. B., E. Mjlhus, H. L. Pecseli, and K. Rypdal (1983), A thermal oscillating twostream instability, Phys. Fluids, 26, 146, doi: http://dx.doi.org/10.1063/1.863993.

[23] Ebihara, Y., R. Kataoka, A. T. Weatherwax, and M. Yamauchi (2010), Dayside proton aurora associated with magnetic impulse events: South Pole observations, J. Geophys. Res. 115, A04301, doi:10.1029/2009JA014760.

[24] Eliasson, B., X. Shao, G. Milikh, E. V. Mishin, and K. Papadopoulos (2012), Numerical modeling of artificial ionospheric layers driven by high-power HF heating, J. Geophys. Res., 117, A10321, doi:10.1029/2012JA018105.

[25] Fialer, P. A. (1974), Field-aligned scattering from a heated region of the ionosphere: Observations at HF and VHF, Radio Sci., 9, 923.940.

[26] Fu H. and W.A. Scales (2011), Nonlinear evolution of the ion acoustic instability in artificially created dusty space plasmas, J. Geophys. Res., 116, A10315.

[27] Fu, H., and W. A. Scales (2012), Nonlinear evolution of the dust acoustic instability in artificially created dusty space plasmas, IEEE Trans. Plasma Sci., 40, 1223-1228, doi: 10.1109/TPS.2011.2180929.

[28] Fu H. and W. A. Scales (2011), Nonlinear evolution of the dust acoustic instability in artificially created dusty space plasmas, IEEE Trans. Plasma Sci., in press.

[29] Ganguli G., Y.C. Lee, and P. Palmadesso (1998), Electron-ion hybrid mode due to transverse velocity shear, Phys. Fluids, vol. 31, pp. 2753-2756.

[30] Galand, M., and S. Chakrabarti, (2006), Proton aurora observed from the ground, J. Atmospheric and Solar-Terrestrial Phys. 68, 13, 1488-1501, doi: 10.1016/j.jastp.2005.04.013.

[31] Goldberg R. A., DROPPS: A study of the polar summer mesosphere with rocket, radar and lidar, Geophys. Res. Lett., vol. 28, pp. 1407 - 1410, 2001.

[32] Huba, J.D., G. Joyce, and J.A. Fedder, Sami2 is Another Model of the Ionosphere (SAMI2): A new low-latitude ionosphere model, J. Geophys. Res., 105, 23,035, 2000.

[33] Huang, J. and S.P. Kuo, A theoretical model for the Broad Up-Shifted maximum in stimulated electromagnetic emission spectrum, J. Geophys. Res., 99, 19569, 1994.

[34] Huang, J. and S. P. Kuo (1995), A generation mechanism for the downshifted peak in stimulated electromagnetic emission spectrum, J. Geophys. Res., 100(A11), 21,43321,438, doi:10.1029/95JA02302.

[35] Hysell, D. L., E. Nossa, and M. McCarrick (2011), Xmode suppression of artificial E region field-aligned plasma density irregularities, Radio Sci., 46, RS2010, doi:10.1029/2010RS004551.

[36] Jackson, J. E., H. A. Whale, and S.J. Bauer (1962), Local ionospheric disturbance created by a burning rocket, J. Geophys. Res., 67, 2059-2061.

[37] Kelley, M. C., (1989), The earth's ionosphere, International Geophysics Series, Vol 43, Page 5-6.

[38] Kivelson M. G., C. T. Russell (1973), Active experiments, magnetospheric modification, and a naturally occurring analogue, Radio Sci., vol. 8, no. 11, pp-1035-1048.

[39] Lie-Svenson O., T. A. Blix, and U. P. Hoppe (2003), Modeling the plasma response to small-scale aerosol particle perturbations in the mesopause region, J. Geophys. Res., vol. 108, pp. 243-265.

[40] Leyser, T. B., B. Thide, H. Derblom, A. Hedberg, and B. Lundborg, Stimulated electromagnetic emission near electron cyclotron harmonics in the ionosphere, Phys. Rev. Lett., 63, 1145, 1989

[41] Leyser, T. B. (1991), Parametric interaction between upper hybrid and lower hybrid waves in heating experiments, Geophys. Res. Lett., 18, 3, 408-411, doi:10.1029/91GL00136.

[42] Leyser, T. B., B. Thide, S. Goodman, M. Waldenvik, E. Veszelei, S. M. Grach, A. N. Karashtin,G. P. Komrakov, and D. S. Kotik (1992), Narrow cyclotron harmonic absorption resonances of stimulated electromagnetic emission in the ionosphere, Phys. Rev. Lett., 68, 22, 3299-3302, doi:10.1103/PhysRevLett.68.3299.

[43] Leyser, T. B. (2001), Stimulated electromagnetic emission by high-frequency electromagnetic pumping of the ionospheric plasma, Space Science Reviews, 98, 223-328, doi:10.1023/A:1013875603938.

[44] Mahmoudian, A. and W. A. Scales (2012), Irregularity excitation associated with charged dust cloud boundary layers, J. Geophys. Res., 117, A02304, doi:10.1029/2011JA017204.

[45] Mahmoudian A., W. A. Scales, P.A. Bernhardt, A. Samimi, E. Kendall, J. M. Ruohoniemi, B. Isham, O. Vega, and M. Bordikar (2013), Ion gyro-harmonic structuring in the stimulated radiation spectrum and optical emissions during electron gyro-harmonic heating, J. Geophys. Res., in press.

[46] Mendillo, M., G. S. Hawkins, and J.A. Klobuchar (1975a), A Large-Scale Hole in the Ionosphere Caused by the Launch of Skylab, Science, 187, 343.

[47] Mendillo, M., G. S. Hawkins, and J. A. Klobuchar (1975b), A sudden vanishing of the ionospheric F region due to the launch of Skylab, J. Geophys. Res., 80, 2217-2228, doi:10.1029/JA080i016p02217.

[48] Mendillo, M. (1988), Ionospheric holes: A review of theory and recent experiments, Adv. Space Res., 8, 51-62.

[49] Milikh, G. M., K. Papadopoulos, M. McCarrick, and J. Preston (1999), ELF emission generated by the HAARP HF-heater using varying frequency and polarization, Radiophysics and Quantum Electronics, 42, 639-646, doi:10.1007/BF02676849.

[50] Mishin, E., and T. Pedersen (2011), Ionizing wave via highpower HF acceleration, Geophys. Res. Lett., 38, L01105, doi:10.1029/2010GL046045.

[51] Norin, L., Leyser, T. B., Nordblad, E., Thide, B., and McCarrick, M.: Unprecedentedly strong and narrow electromagnetic emissions stimulated by high-frequency radio waves in the ionosphere, Phys. Rev. Lett., 102, 065003, doi:PhysRevLett 102.065003, 2009.

[52] Nossa, E., D. L. Hysell, C. T. Fallen, and B. J. Watkins (2009), Radar observations of artificial E]region field]aligned irregularities, Ann. Geophys., 27, 2699.2719.

[53] Ono M., M. Porkolab, and R. P. H. Chang (1980), Parametric decay into ion cyclotron waves and drift waves in multiion species plasma, Phys. Fluids 23, 1656; doi: 10.1063/1.863185

[54] Oppenheim M. and N. Otani (1996), Saturation of Farley-Buneman instability via nonlinear electron ExB drifts, J. Geophys. Res., vol. 101, no.A8, pp. 17273-17286.

[55] Pedersen, T., B. Gustavsson, E. Mishin, E. Kendall, T. Mills, H. C. Carlson, and A. L. Snyder (2010), Creation of artificial ionospheric layers using high power HF waves, Geophys. Res. Lett., 37, L02106, doi:10.1029/2009GL041895, 2010

[56] Porkolab, M. (1974), Theory of parametric instability near the lower-hybrid frequency, Phys. Fluids, 17, 1432-1442, doi:10.1063/1.1694910.

[57] Rodriguez P., E . J. Kennedy, M . J. Keskinen, S a. Basu, M. McCarrick, J. Preston, H. Zwi, M. Engebretso, A . Wong, R. Wuerker, M . L. Kaisers, M.D. Deschs, K . Goetzc, J.-L. Bougeret and R . Manning (1999), A Wave Interference Experiment with HAARP, HIPAS, and WIND, Geophys. Res. Lett., vol. 26, no. 15, pp 2351-2354.

[58] Ronnmark K. (1982), Computation of dielectric tensor of a Maxwellian plasma, Plasma Phys., 25, 699.

[59] Rosenberg M. (1996), Ion-dust streaming instability in processing plasmas, J. Vac. Sci. Technol. A, 14, 631-633.

[60] Rosenberg, M., M. Salimullah, and R. Bharuthram, (1999) Lower hybrid instability driven by charged dust beam , Planet. Space Sci., 47, 1517-1519.

[61] Rosenberg M., G. Sorasio, (2006), Lower Hybrid Instability in Ionospheric GasDust Formations from Rocket Exhaust, J. Spacecraft, vol. 43, no. 1, pp. 245-247

[62] Rosenberg M., P.A. Bernhardt, S.E. Clark (2011), Excitation of ion waves by charged dust beams in ionospheric aerosol release experiments, Planetary and Space Science, vol. 59, pp.312-318.

[63] Samimi, A., W. A. Scales, P. A. Bernhardt, S. J. Briczinski, C. A. Selcher, and M. J. McCarrick (2012), On Ion Gyro-Harmonic Structuring in the Stimulated Electromagnetic Emission Spectrum During Second Electron Gyro-Harmonic Heating, Ann. Geophys.,30, 15871594, doi:10.5194/angeo-30-1587-2012

[64] Samimi, A., W. A. Scales, H. Fu, P. Bernhardt, S. Briczinski, and M. J. McCarrick (2013), Ion Gyro-Harmonic Structures in Stimulated Radiation During Second Electron Gyro-Harmonic Heating: Part I: Theory, J. Geophys. Res., doi:10.1029/2012JA018146, in press

[65] Scales W. A. and P. A. Bernhardt (1991), Simulations of high (orbital) velocity releases of electron attachment materials in the ionosphere, J. Geophys. Res., vol. 96, pp. 13815-13825.

[66] Scales W. A., P. A. Bernhardt, and G. Ganguli (1994), Early time evolution of negative ion clouds and electron density depletions produced during electron attachment chemical release experiments, J. Geophys. Res., vol. 99, pp. 373-383

[67] Scales, W. A., P. A. Bernhardt and G. Ganguli (1995), Early time evolution of a chemically produced electron depletion, J. Geophys. Res. 100, 269.

[68] Scales, W. A., G. Ganguli, P. A. Bernhrdt, M. Lampe (1998), Wave generation associated with dust cloud expansion into a plasma, Phys. Scr., T75, 238-240.

[69] Scales W. A., M. R. Bordikar, A. Mahmoudian and H. Fu (2010), Irregularities associated with creation of artificial dusty plasmas in near-earth space environment, IEEE Trans. Plasma Sci., vol. 38, pp. 880-885.

[70] Scales, W. A., M. R. Bordikar, A. Samimi, P. A. Bernhardt, S. Briczinski, C. A. Selcher, and M. McCarrick (2011), Observations and theory of ion gyro-harmonic structures in the stimulated radiation spectrum during second electron gyroharmonic heating, General Assembly and Scienti

c Symposium, URSI, doi:10.1109/URSIGASS.2011.6051126.

[71] Shukla P. K., and A. A. Mamun (2000), Introduction to Dusty Plasma Physics, Am. Inst. of Phys., Philadelphia.

[72] Stenflo, L. (1990), Stimulated scattering of large-amplitude waves in the ionosphere, Phys. Scr., T30, 166-169.

[73] Stubbe, P., H. Hopka, B. Thide, and H. Derblom, Stimulated electromagnetic emission: A new technique to study the parametric decay instability in the ionosphere, J. Geophys. Res., 89, 7523, 1984.

[74] Stubbe, P., A. Stocker, F. Honary, T.R. Robinson and T.B. Jones (1994), Stimulated electromagnetic emissions and anomalous hf wave absorption near electron gyroharmonics, J. Geophys. Res., 99, 6233.

[75] Thide, B., H. Kopka, and P. Stubbe (1982), Observation of stimulated scattering of a strong high frequency radio wave in the ionosphere, Phys. Rev. Lett., 49, 1561-1564, doi:10.1103/PhysRevLett.49.1561.

[76] Vahedi V. and M. Surendra (1995), A Monte Carlo collision model for the particle-in-cell method: applications to argon and oxygen discharges, Computer Physics Communications, vol. 87, no.1-2, pp. 179-198.

[77] Winske, D. and M. Rosenberg (1998), Nonlinear development of the dust acoustic instability in collisional dusty plasma, IEEE Trans. Plasma Sci. 26, 92-99.

[78] Zhou H. L., J. Huang, and S. P. Kuo (1994), Cascading of the upper hybrid/electron Bernstein wave in ionospheric heating experiments, Phys. Plasmas, 1, 9, 30443052, doi:http://dx.doi.org/10.1063/1.870929.

Appendices

Appendix A

Numerical Methods

In Chapter 3, the simulation model of hybrid code was introduced. The numerical techniques used for particles and fluids have been well documented. In this section the algorithm and new techniques used will be discussed. In this numerical model, electrons and ions are treated as a fluid, and dust is treated as particle. Algorithm with new methods and time advancement for both particles and fluid will be described below.

A.1 Algorithm

The Particle in Cell (PIC) method is used in this work for the calculations equations governing dust particles. The PIC technique is an efficient and conceptually simple method of solving a wide variety of complex problems involving a large number of particles moving under the action of self-generated and externally imposed forces. It has been used for over several decades in many fields and in particular in plasma physics. The defining characteristic of PIC simulations is the method of calculating the force acting on each particle. The simulation region is divided into a number of cells and the resulting grid is used in the solution of a field equation from which the force on each particle can then be determined. In this case the forces acting of the particles are electromagnetic forces. Hence the relevant field equation is then Poisson's equation or current closure equation. Background plasma is treated as fluid. The continuity and momentum equations govern the density and velocity of the fluid species. Poisson's equation to solve the potential and electric field are calculated using spectral methods.

The complete algorithm used here involves the basic steps of advancing position and velocity of species, calculating charge density, calculating potential and electric fields, interpolating fields to grid points. In this case changes are made to accommodate the fluid background plasma and dust particles. To simulate injection of artificial dust particles loading of particles changed to injection of particles. Dust particles are injected from the left boundary at every

time step with drift velocity as per specified density per cell. Similarly at each step dust particles that drift out the right boundary of the box are taken out. OML dust charging model is used to calculate the charge on the dust particles. Figure A.1 shows a generic flowchart of this simulation.

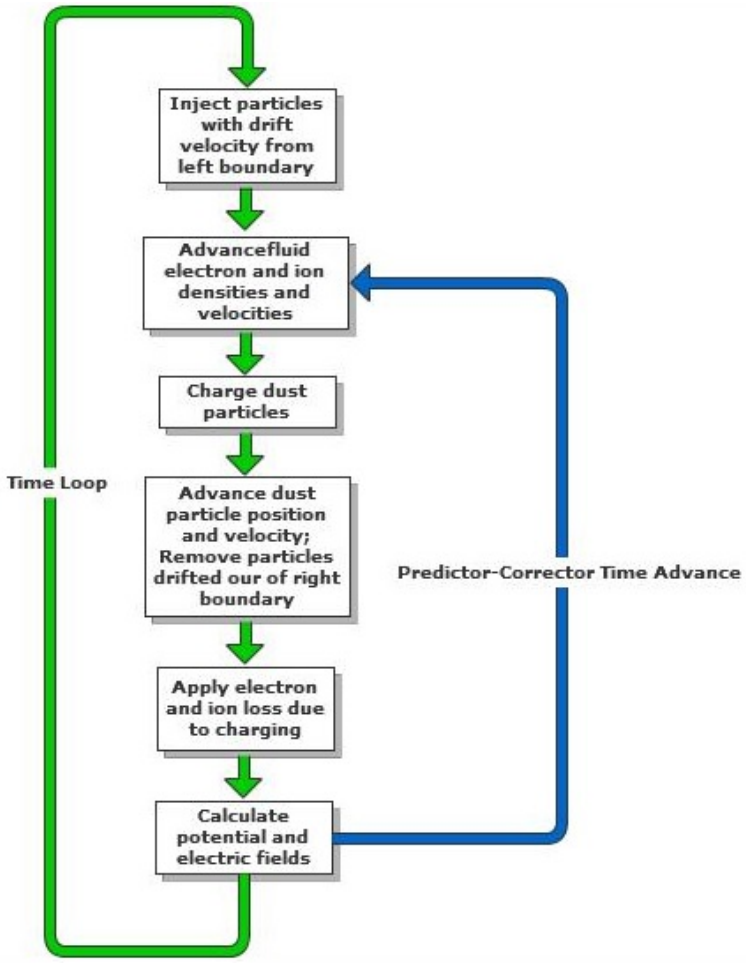

Figure A.1: Algorithm of PIC model shown in flowchart format

A.2 Time Advance with Predictor Corrector Method

In this work a predictor-corrector algorithm is used and particles and fluid are advanced twice per time step. A generic schema of time advance in this method is shown in Figure A.2. Calculations made at each time step are described in detail below.

1. Position, velocity and density are advanced first using standard leap frog

2. The magnetic field is then advanced, and then the electric field to the half step
3. The fields at the half step are used to predict fields at the full step
4. Predicted fields at the full step are used to advance plasma species quantities to the next full time step
5. Fields at the next half step are predicted
6. These fields are averaged with fields from the previous half step to get the corrected fields at the full step

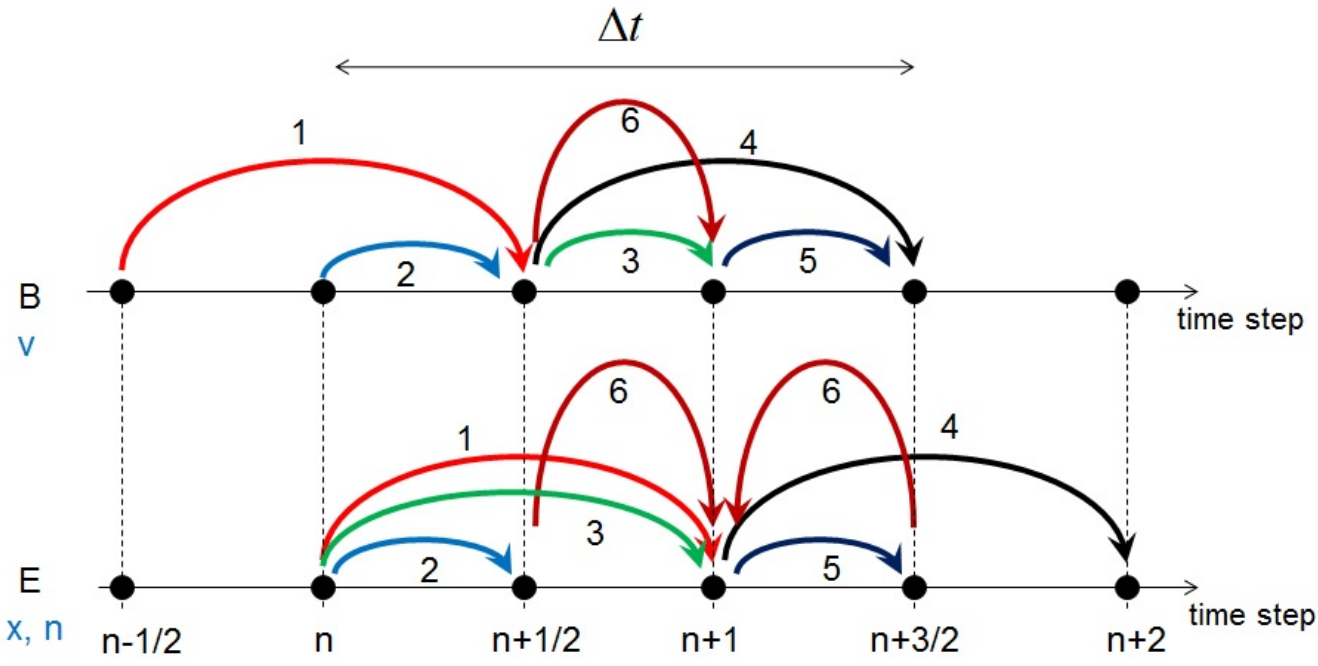

Figure A.2: Time advance of hybrid code

The fields are staggered on the spatial grid to ensure that $\bigtriangledown \times \vec{E}$ is on $\vec{B}$ and $\bigtriangledown \times \vec{B}$ is on $\vec{E}$

Appendix B

Susceptibilities in Dispersion Relation Solution of Three-wave Process

In this appendix, the susceptibilities χ_e, χ_i, χ_H are expressed as unitless variables that are used by [Ronnmark, 1982]. The susceptibilities are used to obtain expressions for the dispersion relations for the three-wave interaction process [Eq. (4.4)]. The dispersion relation is solved numerically using Newton's method to obtain the growth rate for the three-wave process. Note that the derivatives of the susceptibilities are also needed to solve the dispersion relations for both the three-wave processes since Newton's method requires the derivatives. Note that the susceptibilities for electron, ions and hydrogen are obtained considering all the species as magnetized.

Starting with the susceptibilities for the ions [Porkolab, 1974] given by

$$\chi_j(\omega) = \frac{1}{k^2\lambda_{Dj}^2}\left\{1 + \zeta_{j0}\sum_{n=-\infty}^{n=\infty}\Gamma_n(b_j)Z(\zeta_{jn})\right\} \tag{B.1}$$

where, Z is the Fried Conte function, $\Gamma_n(b_j) = I_n(b_j)\exp(-b_j)$, $b_j = k_\perp^2 v_{tj}^2/\Omega_j^2 = k_\perp^2\rho_j^2/2$ and $\zeta_{jn} = (\omega - n\Omega_j)/k_{||}v_{tj}$. $\lambda_{Dj} = (k^2 v_{tj}^2)/\Omega_j$ is the Debye length and $v_{tj} = \sqrt{2T_j/m_j}$ is the thermal velocity of the j^{th} species respectively. Substituting for ζ, v_{tj}, b_j, λ_{Dj} and $\tilde{\omega} = \omega/\Omega_e$, $\tilde{\omega_{pe}} = \omega_{pe}/\Omega_e$ and solving the above equation we get,

$$\chi_j(\omega) = 2\frac{T_e}{T_j}\left(\frac{\tilde{\omega_{pe}}}{k\rho_e}\right)^2\left(\frac{n_j}{n_e}\right)\left\{1 + \frac{\tilde{\omega}}{\rho_e k_{||}\sqrt{m_e T_j/m_j T_e}}\sum_{n=-\infty}^{n=\infty}\Gamma_n(b_j)Z(\zeta_{jn})\right\} \tag{B.2}$$

Solving $\sum_{n=-\infty}^{n=\infty}\Gamma_n(b_j)Z(\zeta_{jn})$ using pade approximation we get,

$$\sum_{n=-\infty}^{n=\infty}\Gamma_n(b_j)Z(\zeta_{jn}) = \sum_{m=1}^{8}\frac{r_m k_{||}\rho_e b_j}{Y^2}\left[R(Y,b_j) + \frac{Y}{b_j}\right] \tag{B.3}$$

where the form of function R of [Rommark, 1982] is given by,

$$R(\tilde{\omega}, \lambda) = \sum_{n=-\infty}^{n=\infty} \frac{n^2 \lambda_n(\lambda)}{\lambda\tilde{\omega} - n} \tag{B.4}$$

Here $Y = \tilde{\omega}\frac{m_j}{m_e} - C_m k_{||}\rho_e\sqrt{(m_j T_j)/(m_e T_e)}$, where r_m and C_m are the residues and poles of pade approximant. Making all the substitutions and solving the susceptibility we get,

$$\chi_j(\omega) = 2\frac{T_e}{T_j}\left(\frac{\tilde{\omega_{pe}}}{k\rho_e}\right)^2\left(\frac{n_j}{n_e}\right)\left\{1 + \frac{\tilde{\omega}}{k_{||}\rho_e}\sqrt{\frac{m_j}{m_e}}\sum_{m=1}^{8}\frac{r_m k_{||}\rho_e b_j}{Y^2}\left[R(Y, b_j) + \frac{Y}{b_j}\right]\right\} \tag{B.5}$$

This susceptibility equation is used for all species electrons, ions and hydrogen to solve the dispersion relation for three-wave process.